Van Hove Singularities and Resonant Tunneling in Carbon Nanotubes

I n a u g u r a l - D i s s e r t a t i o n

zur
Erlangung des Doktorgrades der
Mathematisch-Naturwissenschaftlichen Fakultät
der Heinrich-Heine-Universität Düsseldorf

vorgelegt von
Sascha Hügle
aus Freiburg i. Br.

April 2003

Referent: Prof. Dr. R. Egger
Koreferent: Prof. Dr. H.-K. Janssen

Tag der mündlichen Prüfung: 21.05.2003

Gedruckt mit der Genehmigung der Mathematisch-Naturwissenschaftlichen
Fakultät der Heinrich-Heine-Universität Düsseldorf

"Im Lichte bereits erlangter Erkenntnis erscheint
das glücklich Erreichte fast wie selbstverständlich, ...
Aber das ahnungsvolle, Jahre währende Suchen im Dunkeln
mit seiner Abwechslung von Zuversicht und Ermattung
und seinem endlichen Durchbrechen zur Wahrheit,
das kennt nur, wer es selber erlebt hat."

A. Einstein

Contents

Introduction

Mesoscopic physics, especially the description of nanometer-sized systems, is one of the most promising fields for the development of future technology. Besides showing new and rich physics in fundamental research, mesoscopic systems exhibit a vast potential for fascinating applications in very different domains, some of them being already available as commercial products. Typical systems under investigation are quantum wires, i.e., one-dimensional quantum systems with only very few conduction channels, and quantum dots, which are roughly speaking laterally restricted quantum wires leading effectively to zero-dimensional systems with only discrete energy states. These nanoscale devices carry a few to a few thousand electrons being confined on them and behave like artificial atoms.

One of the most challenging and in many respects prototypical systems in mesoscopic physics are carbon nanotubes which were discovered in 1991. Carbon nanotubes are tubular nanoscale objects which can be thought of as graphite sheets wrapped onto a cylinder. Due to their intriguing electronic and mechanical properties, they continue to attract an increasing amount of attention. Besides single-wall nanotubes which consist of only one graphite shell, there also exist multi-wall nanotubes consisting of a few concentrically arranged graphite shells.

Due to the one-dimensional nature of their electronic conduction bands near the Fermi energy, metallic single-wall nanotubes constitute a nearly perfect realization of 1D quantum wires. In particular, because of this reduced dimensionality, electron-electron correlations invalidate the usual Fermi liquid picture leading to a Luttinger liquid phase. This is the generic phase for 1D metals and has been observed experimentally in the suppression of the tunneling density of states, or in interaction-dependent power-law behavior of transport properties. While single-wall nanotubes are ballistic with elastic mean free paths up to several microns, the detailed behavior of multi-wall nanotubes is not yet completely understood. Thus, lately much effort, including this work, has been devoted to studying the electronic properties of multi-wall nanotubes, especially with focus on disorder induced effects.

Since real materials always enclose impurities, dislocations, or more general forms of disorder, this generally implies to go beyond usual paradigms that have been used successfully for pure systems. To strengthen the usefulness of carbon nanotubes, the understanding of the influence of defects in nanostructures deserves particular attention since at such very small scale, any disruptions of local order may affect

dramatically the physical response of the nanodevice. For the implementation to efficient technological devices, one needs to seriously understand, control, and possibly confine the magnitude of these inherent quantum fluctuations, induced by disorder or magnetic field.

Therefore, we present a theory for the van Hove singularity in the tunneling density of states of disordered multi-wall nanotubes. However, this problem is also of great importance for other multi-channel quantum wires. We answer the question: How is the van Hove singularity modified by the presence of disorder? This question is crucial for the interpretation of several key experiments on multi-wall nanotubes. A typical experimental setup to check our predictions would be, e.g., a scanning tunneling spectroscopy measurement, which can directly probe the tunneling density of states. By using diagrammatic perturbation theory within a non-crossing approximation which is valid over a wide parameter region, we obtain closed analytical expressions governing the disorder-induced broadening and shift of van Hove singularities as new subbands are opened. This problem is highly non-trivial because the (lowest-order) Born approximation breaks down close to the van Hove singularity. Interestingly, the boundary tunneling density of states shows drastically altered behavior compared to the bulk case, even in the clean limit. The typical $1/\sqrt{E-E_n}$ dependence of the van Hove singularity turns into a non-analyticity with $\sqrt{E-E_n}$ behavior close to the boundary, where E_n is the threshold energy.

Quantum dots have been successfully realized, e.g., in semiconductor heterostructures or by using carbon nanotubes. One great advantage compared to real atoms is that their properties can be tuned and controlled in experiments making it possible to study, e.g., transport through a quantum dot via attached leads. Within Coulomb blockade theory, transport only occurs for selected values of the gate voltage capacitively coupled to the dot, resulting in a sequence of equidistant conductance peaks (Coulomb peaks) corresponding to the addition of single electrons. This opens the possibility of building a transistor operating at the level of single electrons and being on that score the ultimate limit of a transistor at all.

Quantum dots also provide a fascinating device to study another interesting and important effect, appearing when the topmost level of the dot is occupied by a single electron only. The resulting situation corresponds to a magnetic impurity in a sea of conduction electrons giving rise to the Kondo effect, which has received an enormous amount of attention over the years. Kondo's original work over thirty-five years ago was intended to explain the anomalous resistivity observed in magnetic alloys. However, in quantum dots the Kondo effect allows for resonant transmission through the island, as observed in recent experiments.

In most treatments of the Kondo effect (and resonant tunneling) in quantum dots, the leads are taken to be Fermi liquids and interactions in the leads are ignored. This is sufficient if the leads are 2D or 3D electron gases, where interactions affect the low-energy properties only perturbatively. In contrast, in 1D arbitrarily weak interactions completely modify the ground state and the low-energy excita-

tions are described by a Luttinger liquid rather than a Fermi liquid. The drastic consequence is that, e.g., in a repulsively interacting Luttinger liquid with a single impurity, transport is completely blocked at very low temperatures. However, adding a second impurity profoundly changes the whole situation since then, even perfect transmissions can be achieved (resonant tunneling).

The problem of resonant tunneling in a Luttinger liquid was first studied a decade ago, but has recently attracted renewed and widespread attention by theorists. This is primarily caused by novel exciting experimental realizations of double-barrier structures in interacting 1D quantum wires as, e.g., single-wall nanotubes with two intramolecular buckles induced by an atomic force microscope. The buckles act as tunneling barriers and thereby create a well-defined island (quantum dot) with a length of a few tens of nanometers. Transport measurements revealed oscillations in the conductance through the island as a function of the gate voltage which are believed to correspond to the addition of single electrons to the dot, and to be a result of the Coulomb blockade. The whole device has been reported to behave as single electron transistor, up to room temperature.

However, the reported unconventional behavior of the conductance measured in this experiment could not be understood within existing theories. As a result, many new and also contradictory results appeared in the literature leading to a recent controversy. Therefore, we try to clarify this situation by carefully reconsidering the problem of transport through a Luttinger liquid with two impurities of arbitrary strength. As this problem is not integrable, exact solutions covering a wide parameter range of interest are out of reach, in marked contrast to the situation of only a single impurity. We present analytical results for the resonance condition as well as a detailed quantum Monte Carlo study of the conductance in such a system. These numerically exact results allow to investigate the line shape of the resonance as well as the behavior of the peak height and width. We will pay particular attention to how the barrier strength influences the physical mechanisms of transport through the double-barrier. This question is related to the breakdown of Coulomb blockade at strong transmission. The validity of our Monte Carlo approach is demonstrated for the non-interacting case by comparing numerical results to the exact solution for arbitrary barrier height. We identify the regime of coherent resonant tunneling where the line shape shows universal scaling behavior, i.e., rescaled resonance curves for different temperature collapse onto a single master curve. In this regime, the line width shows power-law behavior on temperature with the exponent depending on the interaction strength in the system. We could also identify the regime of correlated sequential tunneling thereby resolving the recent controversy mentioned above. With spin, we identify resonant tunneling peaks, but no Kondo effect can be found in this setup.

The entire work is organized as follows. The first chapter gives a brief introduction to carbon nanotubes including some remarks on relevant experimental techniques like scanning tunneling microscopy. Chapter 2 provides the theoretical frame-

work for describing disordered multi-wall nanotubes as needed for studying van Hove singularities in the tunneling density of states of such systems which is done in detail in the third chapter. Then, after introducing the Luttinger liquid description for single-wall nanotubes in Chapter 4, we give a summary of earlier results on resonant tunneling and Kondo effect in quantum dots in Chapter 5. There, we also review recent experimental results that are in close context to our theory for transport through a nanotube quantum dot presented in Chapter 6. Finally, we conclude in the summary. Some calculations which would be too tedious for the main text are provided in several appendices for the interested reader.

Chapter 1

Carbon nanotubes

In this chapter we will review the physical properties of carbon nanotubes. We start by describing growth processes, the crystallographic structure, and the electronic properties. Subsequent, we discuss differences between the two existing classes of nanotubes (single- and multi-wall). Because of its importance as an experimental tool for visualizing as well as manipulating and spectroscopically probing atomic structures, we also briefly describe the scanning tunneling microscopy technique. We close the chapter by giving an outlook on some challenging applications.

1.1 Growth and purification

Carbon nanotubes (NTs) were discovered in 1991 by Iijima [1] (for a recent review, e.g., see [2]). He observed tubular features in electron microscopy images of fullerene soot produced in an arc discharge which were identified as fullerene tubes consisting of multiple shells, in which many tubes were arranged in a coaxial fashion. Such tubes were called multi-wall nanotubes (MWNTs). In 1993, Iijima's group, as well as others, found that the use of transition-metal catalysts leads to NTs with only a single shell [3]. Accordingly, they were called single-wall nanotubes (SWNTs). Because of their simple and well-defined structure, SWNTs serve as model systems both for theoretical calculations as well as for key experiments. As an example, in Fig. 1.1 we show an atomic force microscopy image of a SWNT.

In 1995, Smalley and co-workers found a laser ablation technique that could produce SWNTs at yields of up to 80% instead of the few percent yields of earlier experiments [5]. Later, it has been shown that high yields of NTs can also be obtained with the arc discharge method [6]. A recent development is the use of chemical vapor deposition, in which NTs are grown by decomposing an organic gas over a substrate covered with metal catalyst particles. Either MWNTs or SWNTs can be grown with this technique (see especially [7] and references therein).

The first step in the study of NTs is technological, their purification. Purification steps may consist of controlled oxidation, chemical treatment, filtration and other

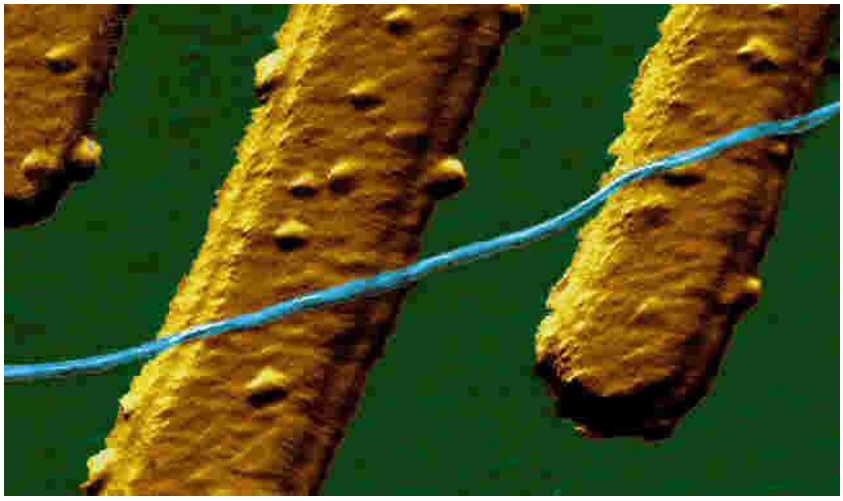

Figure 1.1: *Atomic force microscopy image of a carbon nanotube on top of a Si/SiO_2 substrate with two 15 nm thick Pt electrodes. The tube has a diameter of $\sim$ 1 nm, and is identified as an individual SWNT. (Taken from [4].)*

procedures. The first purification method consisted of burning the raw soot in air which resulted in a relatively pure NT soot, but with damaged tube walls and tips, and with a loss of about 99 weight percent of the material. More advanced methods build on a special filtration technique using a water/surfactant solution to extract the tubes from the suspension. Further purification can be accomplished by size-selection through controlled flocculation and after a final separation, yields as high as 90% in weight are obtained without any damage to the tubes [7].

High resolution transmission electron microscopy provides valuable information about the NT quality prepared by different synthesis methods. In the arc discharge and related methods, NTs are produced in an inert gas atmosphere from graphite at such high local temperature that the carbon evaporates and subsequently forms the NT. The resulting tubes are mainly straight and exhibit a rather flawless structure in transmission electron microscopy images. The NTs grown by the arc discharge method have generally the best structures, presumably due to the high temperature of the synthesis process [7].

As already mentioned, a MWNT is composed of a set of coaxially arranged SWNTs of different radii. The distance between nearest-neighbor shells corresponds, within good approximation, to the van der Waals distance between adjacent carbon sheets in graphite which is $\approx$ 3.4 Å. The outer diameter of NTs depends on the growth process. For SWNTs, one has typically a radius of $R \approx 0.5$ to 1 nm while for MWNTs, the outermost shell radius is $R \approx 5$ to 20 nm. For arc discharge grown MWNTs, R is typically of order 10 nm, but can attain values exceeding 100 nm for some chemical vapor deposition grown MWNTs. Transmission electron microscopy has shown that these large diameter tubes contain a considerable amount of defects.

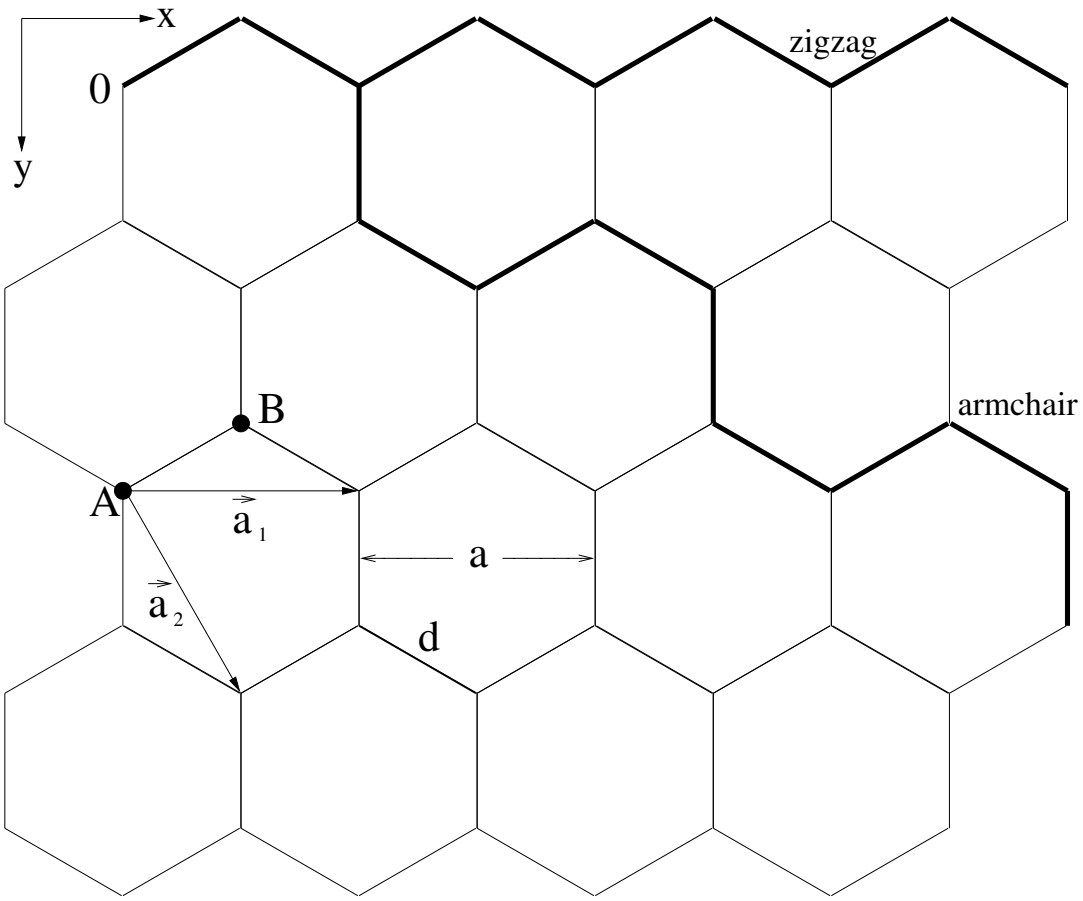

Figure 1.2: *Honeycomb lattice of graphene with the basis consisting of two atoms (A,B) and with the primitive Bravais translation vectors* $\vec{a}_1$ *and* $\vec{a}_2$*. The C-C nearest-neighbor distance* $d \approx 1.42$ *Å determines the lattice constant* $a = \sqrt{3}d \approx 2.46$ *Å. Indicated are also the wrapping directions for zigzag and armchair NTs.*

Typical lengths of NTs are up to 1 mm. Because of their small radius and the large aspect ratio $> 10^4$ (length-to-diameter ratio), they provide an important system for studying one-dimensional (1D) physics, both theoretically and experimentally. Thereby, main advantages are their high chemical stability as well as their extraordinary mechanical properties. Most important for our study are, however, the remarkable electronic properties of carbon NTs on which we will mainly focus in the remainder.

1.2 Crystallographic structure

A SWNT can be constructed from a slice of graphene (that is a single planar layer of the honeycomb lattice of graphite, see Fig. 1.2) rolled into a seamless cylinder, i.e., with all carbon atoms covalently bound to three neighbor carbons by sp^2 molecular

orbitals. The mapping of the graphene sheet onto the cylindrical surface can be specified by a single superlattice translation vector $\vec{T}$ which defines an elementary orbit around the waist of the cylinder, therefore connecting two crystallographically equivalent sites on the two-dimensional (2D) graphene sheet. In the absence of disclinations, the superlattice vector $\vec{T}$ is an element of the original graphene lattice. The wrapping is conventionally indexed by two integers $0 \leq s \leq r$ such that $\vec{T} = r\vec{a}_1 + s\vec{a}_2$, where $\vec{a}_1 = a(1,0)$ and $\vec{a}_2 = a(1/2, \sqrt{3}/2)$ are the primitive Bravais translation vectors of the honeycomb lattice of length $a = \sqrt{3}d \approx 2.46$ Å (a is called lattice constant), with the C-C nearest-neighbor distance d (see Fig. 1.2). Together with the basis of the honeycomb lattice that consists of two atoms, the vectors $\vec{a}_1$ and $\vec{a}_2$ span the complete lattice.

According to the construction, the arrangement of carbon atoms on the tube surface is determined by the integer indices r and s resulting in a so-called (r, s) NT. Vectors $(r, 0)$ denote *zigzag* tubes while vectors (r, r) denote *armchair* tubes (see Figures 1.2 and 1.3). These two cases with especially high symmetry correspond to the limiting cases of a general chiral tube specified by all other vectors (r, s) with $s \neq 0, r$.

Equivalently to the two integers r and s, one can specify the NT in terms of the tube radius $R = |\vec{T}|/2\pi = a\sqrt{r^2 + s^2 + rs}/2\pi$ and the chiral angle $\theta = \tan^{-1}[\sqrt{3}s/(s + 2r)]$, which is the angle between $\vec{a}_1$ and $\vec{T}$ and therefore measures the torsion of the lattice with respect to $(r, 0)$. Because of the sixfold symmetry of the honeycomb lattice, several different integers (r, s) will give rise to equivalent NTs. To define each tube once and once only, we have to restrict the chiral angle to $0° \leq \theta \leq 30°$ which is equivalent to the restriction $0 \leq s \leq r$ made before.

1.3 Electronic properties

An interesting point is that MWNTs allow us to study the transition from the single molecule (SWNT) to the macroscopic crystal (graphite). Accordingly, they are in-between the 1D (SWNT) and 2D (planar graphene) limit. The question that arises is whether their electronic properties are closer to that of graphite or do MWNTs rather behave as a set of independent SWNTs? It is thus useful to briefly highlight the electronic properties of the two reference systems, graphite and ideal SWNTs.

Starting with graphite, we will first review the band structure of a graphene sheet. It is convenient to transform to the reciprocal lattice[1] which, for a periodic lattice, corresponds to the "momentum space". The Wigner-Seitz unit cell[2] for the

[1] Remember that the product of a lattice vector $\vec{r}$ and a vector $\vec{G}$ of the reciprocal lattice is just $\vec{r} \cdot \vec{G} = 2\pi n$, with integer n.

[2] For a certain lattice structure there exist several possible unit cells, all having of course the same (minimal) volume. The Wigner-Seitz unit cell now is constructed by connecting a lattice point with straight lines to all possible neighbor points. The smallest volume generated by the perpendicular bisectors of the bonding lines is then called Wigner-Seitz unit cell.

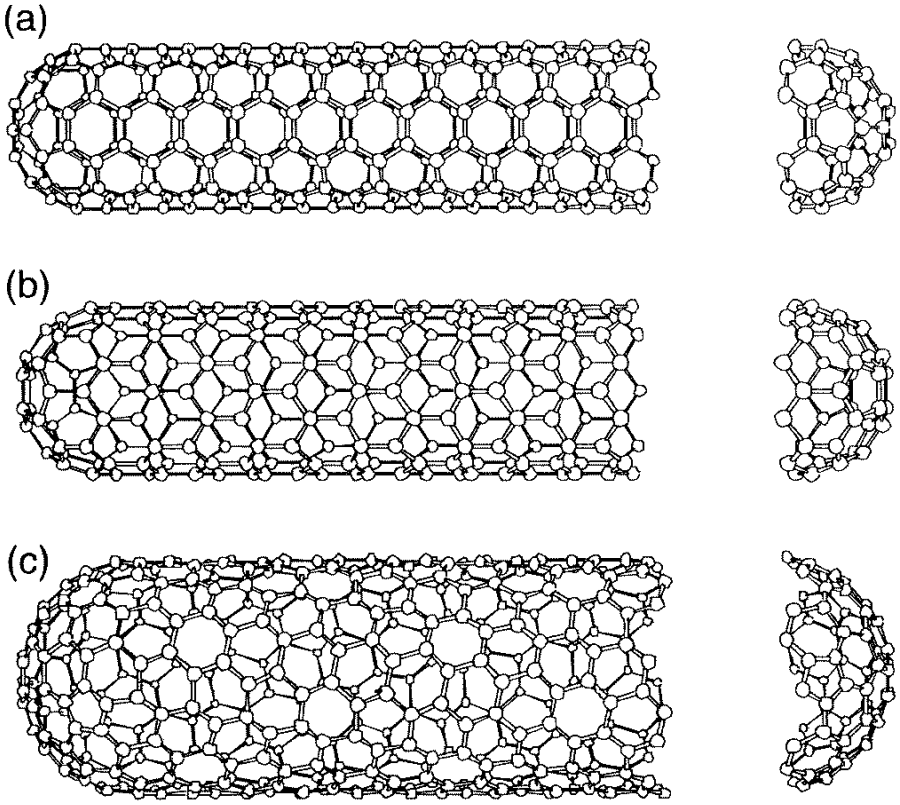

Figure 1.3: *SWNTs with different chiralities and possible caps at each end: (a) shows a (r, r) armchair NT which corresponds to a chiral angle $\theta = 30°$, (b) shows a $(r, 0)$ zigzag NT with $\theta = 0°$, and (c) shows the general case of a chiral tube with $0° < \theta < 30°$. The tubes shown in the figure correspond to (r, s) values of (a) (5,5), (b) (9,0), and (c) (10,5). (From [8].)*

reciprocal lattice is called the first Brillouin zone and has, for the honeycomb lattice, the form of a hexagon (see Fig. 1.4). As already mentioned, the carbon atoms in a graphene sheet are covalently bound by sp^2 molecular orbitals and the fourth valence electron, an atomic p_z-state, hybridizes with all other p_z-orbitals to form a delocalized π-band. The band structure of a graphene sheet was calculated already in 1947 by Wallace using the nearest-neighbor tight binding approximation on a honeycomb lattice [9]. The corresponding Hamiltonian can easily be diagonalized,

$$H = t \sum_{<i,j>} c_i^\dagger c_j + \text{h.c.} \,,$$

with the creation operator $c_i^\dagger$ for a π-electron on lattice site i and the hopping matrix element $t \approx 2.5$ eV (given by the nearest-neighbor C-C overlap integral). The resulting dispersion relation is straightforward to derive (see also [10]),

$$E(\vec{k}) = \pm t \left\{ 1 + 4\cos^2\left(\frac{k_x a}{2}\right) + 4\cos\left(\frac{k_x a}{2}\right)\cos\left(\frac{\sqrt{3}k_y a}{2}\right) \right\}^{1/2} .$$

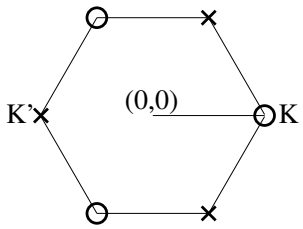

Figure 1.4: *Wigner-Seitz unit cell for the reciprocal lattice (first Brillouin zone) of the honeycomb lattice. Only the corner points exhibit a gapless band structure, i.e., the Fermi surface is collapsed to isolated points, with only two of them being independent (K, K'). Each set of points $\circ$ and $\times$ represents equivalent points since they differ only by reciprocal lattice vectors.*

From such a calculation it is now seen that the bonding π-band (valence band, "$-$") is always energetically below the antibonding π^*-band (conduction band, "+") for all wavevectors, except at the corner points of the first Brillouin zone, where the band splitting is zero by symmetry of the honeycomb lattice. Accordingly, an isolated graphene sheet is a semimetal, whose 2D band structure near the Fermi surface consists of six conical energy surfaces in the first Brillouin zone, with the Fermi energy E_F residing at a critical point in the 2D π-electron spectrum (see Fig. 1.5). Theoretically, all bonding states will be filled up to the corner points, which coincide with E_F. Hence, the Fermi surface of undoped graphene consists only of six isolated points, the vertices of the six cones. But there exist only two distinct Fermi points, namely the K and K' points of the first Brillouin zone at $\vec{K} = (\pm 4\pi/3a, 0)$,[3] the remaining points can be mapped onto these two via a reciprocal lattice vector. Up to high energies $E \approx 1$ eV one can linearize the dispersion relation around the Fermi points, $E(\vec{q}) = \pm\hbar v_F|\vec{q}|$ with $\vec{q} = \vec{k} - \vec{K}$ and the Fermi velocity $v_F = \sqrt{3}at/2\hbar \approx 8 \times 10^5$ m/s.

Next, we will turn to the other reference compound, that is a perfect SWNT. When the graphene sheet is wrapped into cylindrical form, the periodic boundary condition around the NT circumference causes quantization of the transverse wavevector component. Along the tube, the electrons are not confined. More precisely, the π-electron eigenstates $\psi(\vec{r})$ have to satisfy the condition $\psi(\vec{r}+\vec{T}) = \psi(\vec{r})$ leading to the requirement that all allowed wavevectors $\vec{k}$ have to fulfill $\vec{T}\cdot\vec{k} = 2\pi n$, with integer n. From this requirement we can also find a condition for the NT to be metallic, namely we have to require that the Fermi vector $\vec{K}$ itself is an allowed wavevector (otherwise there would be a gap in the spectrum), leading to $2r+s = 3n$, which is a necessary condition for a (r, s) tube to be metallic. As we see, armchair NTs should always be metallic while most other tubes are semiconducting. Thus, the conductive properties of NTs depend drastically on the chirality of the hexago-

[3]Obviously, $\cos(2\pi/3) = -0.5$ and hence, the K points are gapless, $E(\vec{K}) = 0$.

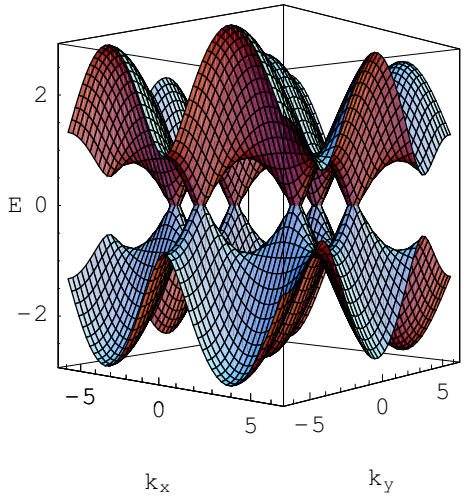

Figure 1.5: *Dispersion relation of the π- (lower half) and π^*-band (upper half) of a 2D planar graphene sheet. The energy is measured relative to the Fermi energy of undoped graphene. As one can clearly see, the upper and lower band touch at the six corner points of the first Brillouin zone which has a hexagonal structure.*

nal carbon lattice along the tube. A slight change in the winding of the hexagons along the tube can transform the NT from a metal into a large-gap semiconductor where the gap is of the order of 1 eV and scales inversely with the tube radius, $E_{\mathrm{gap}} = 2\hbar v_F/3R$. Since r and s should be statistically independent, one assumes that approximately two-thirds of the tubes are semiconducting and one-third are metallic, which is also supported by the experimental findings.

One should mention that also in many nominally metallic tubes like, e.g., the $(6, 0)$ zigzag NT, a minigap appears at the band center. This is due to the intrinsic tube curvature which reduces the overlap of nearest-neighbor π-orbitals resulting in a shift of $\vec{K}$ such that the allowed 1D subband no longer passes through it, and hence, a small gap opens. Such gaps have been observed experimentally, have a size of a few tens of meV, and scale as $1/R^2$ [11]. However, in armchair NTs such secondary gaps cannot appear due to the high symmetry of the tube lattice and therefore, armchair NTs are indeed always metallic.

The 1D band structure can easily be constructed using the 2D band structure of graphene. Let us denote the wavevector along the tube direction by k and the transverse component by $k_\perp$, where the allowed $k_\perp$ are spaced by $1/R$. Because of this quantization of circumferential modes, the tube's electronic states do not form one wide electronic energy band but instead split into 1D subbands with band onsets at different energies (see Fig. 1.6). Each $k_\perp$ within the first Brillouin zone gives rise to a 1D subband and hence, a set of subbands $E_{k_\perp}(k)$ is obtained which are often referred to as *transverse modes* in analogy with the modes of an electromagnetic waveguide. A large-diameter tube will have many (occupied) subbands, while a

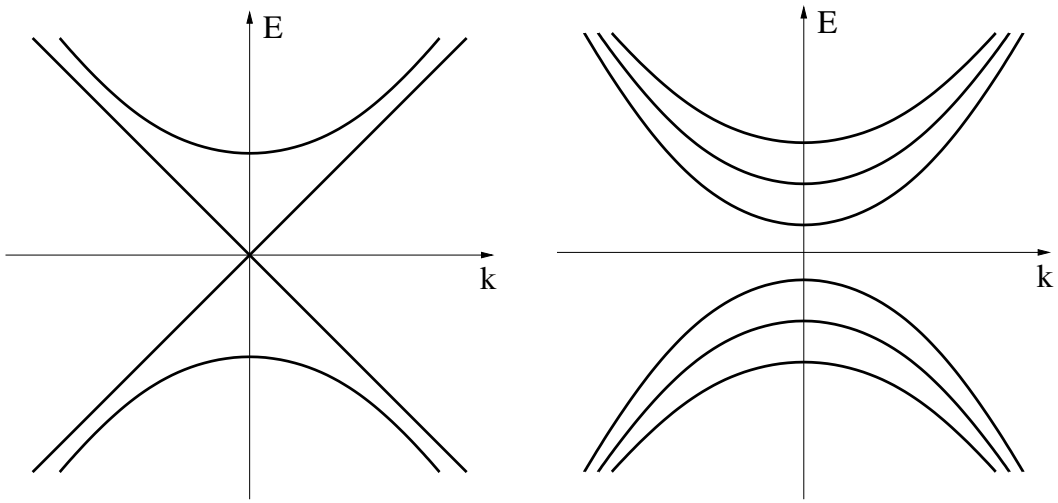

Figure 1.6: *Dispersion relation for the 1D electronic energy bands of a metallic (left) and a semiconducting (right) NT. While in the metallic case there is a non-zero density of states (DOS) at the Fermi level, in the semiconducting case there is a band gap leading to a vanishing DOS in the vicinity of E_F (undoped case).*

small-diameter tube has only a few of them. For SWNTs, subbands are widely separated in energy on the scale of 1 eV, much larger than the room temperature thermal energy of about 1/40 eV.

In semiconducting NTs, there are no electron states at the Fermi level while in metallic NTs, two of the 1D subbands cross the Fermi energy. They are constructed out of the six energy cones of graphene which collapse into two independent 1D conduction channels since at each case three of the cones are equivalent. The current through metallic SWNTs is therefore predicted to be carried by only this pair of subbands. Taking into account the spin degeneracy of the electrons, metallic SWNTs have altogether four independent conduction channels. The number N of independent conduction channels determines the conductance G of a ballistic (i.e., without backscattering) 1D system adiabatically connected to external leads according to the Landauer conductance formula, $G = NG_0$, where $G_0 = e^2/h \approx [25.8\ \mathrm{k\Omega}]^{-1}$ is the conductance quantum. SWNTs are thus predicted to be prototype 1D quantum wires.

To summarize, depending on the specific realization (i.e., the chiral angle), a NT may be a true 1D metal with a non-vanishing density of states (DOS) at the Fermi energy or a semiconductor with a gap (see Fig. 1.6) [12, 13]. This is in marked contrast to the 2D graphene sheet which is a zero-gap semiconductor (semimetal).

We want to close this section by commenting on a subtle fact concerning 1D metallic wires. In 1930, Peierls showed that 1D metallic wires are essentially unstable and will turn semiconducting [14]. That is what happens, for example, to polyacetylene and other so-called conducting polymers, which have gaps of a few

eV. NTs are an exception to this general rule. Because of their tubular structure, the energy change of setting up a Peierls distortion is very unfavorable. The fact that NTs can be metallic at the level of a single molecule is therefore unique.

1.4 Differences between single- and multi-wall nanotubes

Radius and energy scale

Neglecting the inner shells of a MWNT for the moment (inter-shell tunneling is largely suppressed for a number of reasons [15]), the main difference between a SWNT and a MWNT is the outer diameter of the graphene cylinder. SWNTs have typical diameters of $\approx$ 1 to 2 nm while MWNTs normally have diameters in the range of 10 to 40 nm. This one order of magnitude difference in diameter relates into an order of magnitude difference in energy scale. For a semiconducting MWNT, tight binding calculations predicted a gap of order 0.1 eV for a 10 nm diameter tube, whereas for a SWNT the gap is of order 1 eV. This scale is also roughly valid for the energy separation between the first conduction and valence subbands above and below the Fermi level for metallic tubes.

Magnetotransport

With regard to electrical measurements in magnetic fields, orbital effects cannot be studied in SWNTs because extremely high magnetic fields would be required. In contrast, a magnetic field of 12 T is enough to induce a magnetic flux of $\phi_0/2$ in a MWNT with an outer diameter of 15 nm ($\phi_0 = h/e$ is the flux quantum). Therefore, valuable information can be obtained from magnetotransport experiments on MWNTs.

Recently, Bachtold *et al.* [16] reported magnetoresistance measurements on individual MWNTs showing the typical fingerprints of diffusive behavior. On applying a magnetic field parallel to the tube axis the resistance decreases as a consequence of weak localization (see Sec. 2.1). For the specific geometry of a cylinder, the weak localization contribution is periodic because of the interference of closed electron trajectories that encircle the cylinder once. Due to the Aharonov-Bohm effect [17], the phase difference $\Delta\varphi$ between each such trajectory and the time-reversed counter-propagating trajectory is solely determined by the magnetic flux ϕ enclosed, $\Delta\varphi = 4\pi\phi/\phi_0$. Consequently, the electrical resistance has an oscillating contribution with period $\phi_0/2$ (Al'tshuler-Aronov-Spivak effect [18]). Similar oscillations were also observed for thin hollow cylinders [19].

The measured resistance oscillations were found to be in good agreement with Al'tshuler-Aronov-Spivak theory if the current is assumed to flow only through the outermost cylinder of the MWNT. Therefore, this experiment leads to the conclusion

that the inner shells of a MWNT do not contribute to transport and that the electric current can be assumed to flow in the outermost (metallic) graphene tube only,[4] at least at low temperatures, and hence, experiments on MWNTs also address a single shell.

Inner shell effects

For MWNTs, one may have to take a weak hybridization of electron states from neighboring tubes into account. Since MWNTs are composed of coaxial cylindrical layers, each with different radii and also different helicities, the adjacent layers are generally non-commensurate, and, as a consequence, the electronic coupling between the layers is decreased relative to graphite and hybridization is therefore expected to be small [20]. Notice however, that the presence of inner shells is one of the main differences between MWNTs and SWNTs since they cause a screening of the electron-electron interaction [21]. In addition, the energy landscape of the incommensurate inner shells acts as a *quasiperiodic* ionic potential on outermost-shell electrons. The effect of such a potential is known to be very similar to a (Gaussian white noise) random potential (see also Sec. 2.3). As a consequence, disorder-dominated behavior can be important even in impurity-free MWNTs.

Intrinsic resistance

By scanning the tip of an atomic force microscope above a NT device using it as a local voltmeter, Bachtold *et al.* separately measured the intrinsic resistance and contact resistances of SWNTs and MWNTs [22]. They showed for the first time that in metallic SWNTs the measured resistance is exclusively due to the contact resistance (there is no measurable intrinsic resistance) thereby demonstrating unambiguously that transport in metallic SWNTs is ballistic over a length of $> 1\mu$m, even at room temperature. In contrast, in MWNTs the voltage drops uniformly (linear) along the tube length with no significant drop at the contacts which indicates that MWNTs behave as diffusive conductors with a well-defined resistance per unit length, $R/L \sim 10$ kΩ/μm. Hence, the important observation is that SWNTs are ballistic while MWNTs are rather diffusive than ballistic (as already expected from the magnetotransport experiment). What remains to be determined is the source of backscattering in MWNTs which at present is not (definitely) known.

Doping

Since diffusive transport requires that the number of subbands $N \gg 1$, one can ask the question why MWNTs are doped to such a degree that $N \gg 1$? By using a new gating technique (electro-chemical gating), Krüger *et al.* have recently shown that

[4] Presumably, this is a consequence of the way in which the NTs are contacted. Since the electrodes are evaporated over the MWNT, they contact the outermost tube preferentially.

MWNTs are indeed hole doped, most likely induced by the adsorption of water [23]. The number of 1D modes is $\neq 2$, but rather 10 to 20. Therefore, MWNTs are not single mode, but rather few mode quasi-1D quantum wires. Whether they are 1D or 2D diffusive is another question.

Mean free path

Therefore, the estimation of the electron mean free path l in NTs is relevant for determining which is the most likely transport regime (ballistic versus diffusive), and further tells us whether or not the conductance should be quantized. While some experiments have observed conductance quantization [24], others suggest, in contrast, rather short mean free paths [16]. Reported elastic mean free paths for MWNTs are in the range $l \approx 5$ to 100 nm (whereas metallic SWNTs can have l of the order of microns), but by intentionally damaging the tubes, e.g., by fast ion bombarding, any level of disorder may be realized experimentally.

For $l \gg 2\pi R$, we have the situation of 1D ballistic transport (as observed in SWNTs) as long as $l > L$, where L is the tube length, and 1D diffusive transport for $l < L$, whereas 2D diffusive behavior is obtained for $l \ll 2\pi R$. The regime of 1D diffusive transport is characterized by a diffusive motion of the electrons along the tube whereas the motion around the circumference is ballistic. Therefore, this regime is also called *quasi-ballistic*.

1.5 Scanning tunneling microscopy/spectroscopy

The rapid advances in nanoscale science were only made possible by new materials (e.g., carbon NTs) and the development of a special microscope which enabled the individual atom of a surface to be visualized for the first time.

Invented by Binnig and Rohrer in 1981, the scanning tunneling microscope (STM) is based on electron tunneling [25]. Using piezodrivers, one can position the STM's conducting tip to within a few angstroms of the surface of a conducting (metal, semiconductor or superconductor) substrate. At such close distances, the wavefunctions of both will overlap. Consequently, if a bias voltage is applied between the tip and the substrate, electrons from the tip have a finite probability of tunneling across the vacuum space to the sample, resulting in a measurable current. This tunneling current can be calculated using perturbation theory (Fermi's golden rule) and is found to be proportional to the local DOS of the surface at the Fermi level, taken at the position of the tip [26]. An example of an STM image of a SWNT is shown in Fig. 1.7. Besides providing extremely high resolution images of the substrate surface, the STM can also be used to fabricate and spectroscopically probe atomic-scale structures.

The most promising present technique for carrying out sensitive measurements of the electronic properties of individual NTs is scanning tunneling spectroscopy

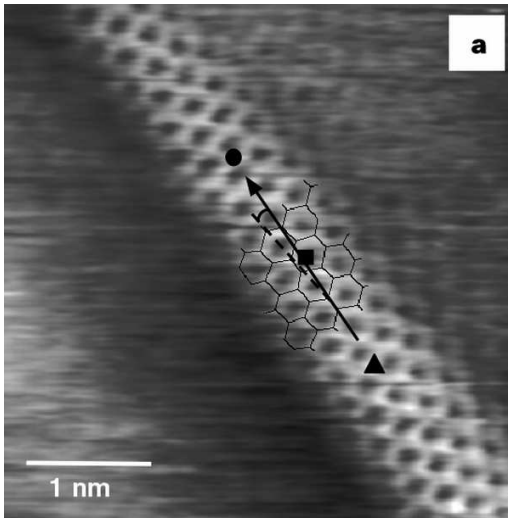

Figure 1.7: *This STM image was recorded in the constant-current mode and it resolves the atomic structure of a SWNT. The tube axis is indicated with a solid black arrow. A portion of a 2D graphene layer is overlaid to highlight the atomic structure. (This image is taken from [12].)*

(STS). With this technique, it is further possible to carry out both STS and STM measurements at the same location on the same tube. Since the STM has the power to obtain atomically resolved images of the tube's hexagon lattice, it is possible to measure the tube diameter as well as the chiral angle concurrently with the STS spectrum and thus, to correlate the electronic structure with the chiral structure of the tube. In this way the theoretical predictions have been experimentally confirmed [12, 13, 27, 28]. Further, STS at low temperatures ($T < 10$ K) allows for an energy resolution in the range of meV and therefore, the combination of STM and STS makes it also possible to directly image the lateral distribution of energy-selected electronic states [29].

The vacuum barrier between the STM tip and the sample forms a convenient junction for STS as it allows tunnel currents at large bias voltages. In STS, scanning and feedback are switched off (i.e., the position of the STM tip is fixed above a single NT), and the tunneling current I between tip and NT is recorded as a function of the bias voltage V applied to the sample. The differential conductance dI/dV can then be considered to be proportional to the tunneling density of states[5] of the tube examined. On semiconductors, the normalized differential conductance $(dI/dV)/(I/V)$ has been argued to give a better representation of the tunneling density of states than the direct derivative dI/dV, partly because the normalization accounts for the voltage dependence of the tunnel barrier at high bias (for details see [30]).

[5]This is the DOS at a certain position x and hence, in general, a function of energy and space coordinates (see Chapter 3).

The great possibilities of STM in the fabrication and manipulation of nano- and even atomic-scale structures have been impressively demonstrated by the creation of so-called quantum corrals [30]. There, single atoms are arranged on a substrate in order to form, e.g., a circle or ellipse which can be used to directly demonstrate the wave character of particles. Concerning NTs, one can use the STM to induce, e.g., a buckle (that would effectively act as an impurity for electron transport) in a single tube or to arrange several tubes on a substrate in order to form a certain electronic circuit.

Besides the STM there exists another important scanning probe microscope, namely the atomic force microscope. There, the probing tip is attached to a fine cantilever and as the sample is scanned, the deflection of the cantilever is measured. From these data the surface of the sample can be reconstructed. The great advantage of the atomic force microscope is that also non-conductive materials can be studied. Clearly, one can also use an atomic force microscope to manipulate and arrange NTs on a substrate.

1.6 Applications

There exist many challenging applications of carbon NTs in very different fields (for a general survey see [7]), some of them being already available as commercial products. What is so special about carbon NTs? The answer lies in their unique physical properties, structural and electronic. For example, NTs have a small specific weight and a record-high elastic modulus (NTs can, e.g., be used to design new composite materials being much more stable than steel and having at the same time a smaller specific weight). They are predicted to be by far the strongest fibers that can be made. Additionally, when a tube is bent, it does not directly fracture like most materials but buckles like a drinking straw. When the bending strain is released, the tube straightens out again. Such remarkable mechanical properties are relevant to a broad range of potential applications. Proposals span a wide spectrum, from molecular electronics to hydrogen storage, bulletproof vests and even artificial muscles.

NTs have been successfully used as field emission devices [31] for flat panel displays [32]. Due to the small radius of the tube, high local fields can be produced when applying a potential between a NT-coated surface and an anode, which causes electrons to tunnel from the tube tip into the vacuum. The use of NTs further removes the need for ultrahigh vacuum in these devices and saves energy because NTs field emit at room temperature, no heating is required. Even x-ray and microwave generators are possible [33]. The compact geometry of NT-based x-ray sources suggests their possible use for medical imaging, possibly even for x-ray endoscopes.

Due to their capillary properties, NTs are (controversially) discussed for hydrogen storage, e.g., for fuel cells that power electric vehicles or laptop computers (see [34] and references therein).

Further, NTs are discussed as future components for building up molecular electronic devices. Dramatic recent advances have fueled speculation that NTs will be useful for down-sizing electronic circuit dimensions. One can imagine to construct complete electronic circuits from interconnected NTs. Because the electronic properties depend on helicity, it should be possible to produce a diode, e.g., by grafting a metallic NT to a semiconducting one. Such a device has already been demonstrated. Also a field effect transistor with only one SWNT as active element [35] and even a single electron transistor have been demonstrated to work, importantly at room temperature. IBM expects that NT electronics will be realized in about a decade.[6]

Another interesting application is the use of NTs as tips for STMs (or atomic force microscopes). Ever since the discovery of STM, the tip has been a black box. NT tips offer a number of advantages. NTs are chemically inert and mechanically robust, they have a large aspect ratio, and the tip end is, in principle, well defined. Furthermore, they are crash-proof: pressing the NT tip onto a surface will buckle the tube rather than induce tip damage. Subsequent withdrawal will relieve the buckle and recover the original tip.

We want to close this introductory chapter by quoting Richard Smalley: "These nanotubes are *so* beautiful that they *must* be useful for something."

[6] New York Times, 20 May 2002

Chapter 2

Disordered multi-wall nanotubes

We begin this chapter by pointing out the influence of the spatial dimension on the behavior of disordered systems. Then, after deriving the low-energy theory for the electronic states in MWNTs, we discuss the various disorder mechanisms that are possible in such systems. Finally, we briefly summarize some concepts of diagrammatic perturbation theory which will be the basic tool used in Chapter 3.

2.1 Disorder and dimensionality

Since MWNTs are somewhere in-between 1D and 2D systems, we briefly want to comment on the different influence of disorder in systems with different spatial dimension. Consider a model of non-interacting electrons scattered by a random potential due to disorder (Anderson localization problem). If the disorder is weak, then on a short length scale the wavefunction will look like a plane wave, but on a long length scale it will be scattered by the random potential. The multiply scattered wave is expected to have an amplitude everywhere in the sample, just as a plane wave does, and is referred to as an extended state. Anderson pointed out [36] that if the disorder is made progressively stronger, one should expect a qualitative change in the nature of the wavefunction, namely that in the limit of very strong disorder the wavefunction decays exponentially from some point in space on the scale of the localization length (localized state). Physically, this is expected to happen when the mean free path becomes comparable to the wavelength. The interesting question is, what happens for intermediate disorder and does this general picture hold in all dimensions?

Actually, it is easier to establish the existence of localized states than that of extended ones. For example, in 1D it can be shown rigorously that all states are localized, no matter how weak the disorder [37]. On the other hand, the existence or non-existence of an extended state in 2D has been a point of contention for many years (see, e.g., [38]). The scaling theory of localization tries to solve the problem by considering the behavior of the dimensionless conductance g as a function of the

system size L. The scaling function $\beta(g) = d(\ln g)/d(\ln L)$ then allows one to discuss and understand the different influence of the spatial dimension. In 3D, the system can scale to an Ohm's-law conductor ($\beta(g) = 1$) as well as to an insulator with localized states ($\beta(g) < 0$). The critical point $\beta(g) = 0$ is an unstable fixed point. However, the same analysis carried out for 2D and 1D systems suggests that there is no such critical point. Instead, $\beta(g) < 0$ (2D) and < -1 (1D) always. Therefore, at large enough length scales, only localized behavior is possible and hence, there are no truly extended states. In 1D, one crosses over into the localized regime more rapidly than in 2D.

Additionally, in diffusive 2D (and 3D) systems there exists the phenomenon of weak localization [39] if the length of a phase-coherent conductor is much less than the localization length. If we consider (quantum-mechanically) the probability for an electron to return to its starting point, then we have to take into account the interference between closed Feynman paths and their time-reversed paths. Due to the prerequisite of phase-coherence this interference is constructive (in zero magnetic field) leading to a doubling of the return probability compared to the classical diffusion. This so-called enhanced backscattering increases the resistivity and therefore reduces the conductance. This effect, that the average quantum-mechanical conductance is smaller than the classical Drude result, is known as *weak localization effect*. A unique signature of weak localization is that it can be destroyed by a magnetic field because of the broken time reversal symmetry. The interference terms then cancel out due to the accumulation of a Peierls phase in the wavefunction resulting in an anomalous magnetoconductance, i.e., a negative magnetoresistance. The Peierls phase is given by

$$\varphi_P = \frac{e}{\hbar} \oint \vec{A} \cdot d\vec{r} = 2\pi \frac{\phi}{\phi_0} \ ,$$

where the integral is over a closed loop leading to the phase difference $\Delta\varphi = 2\varphi_P$.

2.2 Low-energy theory for multi-wall nanotubes

In order to derive the low-energy theory for MWNTs we start from the dispersion relation of graphene. In the vicinity of the K points, the energy bands in graphene are highly linear and, to a very good approximation, given by

$$E(\vec{k}) = \pm\hbar v_F |\vec{k} - \vec{K}| \ ,$$

with the Fermi velocity $v_F = 8 \times 10^5$ m/s. This linear dispersion relation holds for energies $E < D \approx 1$ eV and is fully equivalent to the light cone in a relativistic theory.

Since the basis of the honeycomb lattice contains two atoms, there are two sublattices $p = \pm$. As a consequence, there are two degenerate Bloch states,

$$\varphi_{p\alpha}(\vec{r}) = \frac{1}{\sqrt{2\pi R}} \exp[-i\alpha \vec{K} \cdot \vec{r}] \ ,$$

at each Fermi point $\alpha = \pm$ corresponding to the two K points. Here, $\vec{r} = (x, y)$ lives on the sublattice p under consideration, and we have already anticipated the correct normalization for NTs. The Bloch functions are defined separately on each sublattice such that they vanish on the other. One can then expand the electron operator for spin $\sigma = \pm$ in terms of these Bloch functions,

$$\Psi_\sigma(\vec{r}) = \sum_{p\alpha} \varphi_{p\alpha}(\vec{r}) \psi_{p\alpha\sigma}(\vec{r}) \ , \tag{2.1}$$

thereby introducing the two-component spinor ψ, where the two components reflect the sublattice degree of freedom. In addition to its physical spin and momentum, the π-electron carries an internal pseudo-spin index p, labeling the sublattice state, and an iso-spin index α, labeling the two independent Dirac spectra derived from the K and K' points of the first Brillouin zone.

Expanding the π-electron Hamiltonian around either of the two Fermi points, and linearizing in spatial derivatives, one finds that the low-energy electronic states of a *clean* graphene sheet are described by a massless 2D Dirac Hamiltonian [40],

$$H = -i\hbar v_F \sum_{pp'\alpha\sigma} \int d\vec{r}\, \psi^\dagger_{p\alpha\sigma}(\vec{r}) (\vec{\sigma} \cdot \vec{\nabla})_{pp'} \psi_{p'\alpha\sigma}(\vec{r}) \ , \tag{2.2}$$

where the 2×2 Pauli matrices $\vec{\sigma} = (\sigma_x, \sigma_y)$ act in the sublattice space.

In order to describe propagating π-electrons on the tube, one has to map (2.2) onto a curved surface which is done by enforcing periodic boundary conditions around, say, the y-direction, the tube pointing along the x-direction. The action of the resulting system can then be interpreted as the action of an equivalent quantum problem in $(1 + 1)$ dimensions, $(x, y) \to (x, \tau)$, with y playing the role of imaginary time τ. Under this correspondence, the circumference of the outermost shell maps to the "temperature" of the quantum system,

$$\beta^{-1} = k_B T_{\text{eff}} = \frac{\hbar v_F}{2\pi R} \ , \tag{2.3}$$

while, however, the physical temperature of the system is still zero. In order to simplify notation, we set $\hbar = v_F = 1$ from now on except for final results.

In the absence of disorder, the electrons on the outermost shell of a MWNT are then described by the Dirac Hamiltonian

$$H_0 = \frac{1}{\beta} \sum_n \int \frac{dk}{2\pi}\, \psi^\dagger(\vec{k}) (\vec{\sigma} \cdot \vec{k} + M\sigma_y) \psi(\vec{k}) \ , \tag{2.4}$$

with $\vec{k} = (k, \omega_n)$. The "Matsubara frequencies" $\omega_n = k_\perp = 2\pi n/\beta$, with integer n, arise due to the finite radius, see Eq. (2.3), and reflect quantized transverse momentum. The effects of the tubule size, shape and symmetry can be included through an effective vector potential [15].

Albeit the mass M is zero for a 2D graphene sheet, it can be non-zero for NTs due to chirality effects or an applied magnetic field. In general, a flux Φ (in units

of the flux quantum $\phi_0 = h/e$) gives rise to a mass $M = 2\pi\Phi/\beta$. Chirality effects in a (r, s) tube cause a flux $\Phi_1 = -(2r + s)/3$ [15] while a magnetic field B applied parallel to the tube axis causes an additional flux $\Phi_2 = B/B_0$, with $B_0 = h/\pi R^2 e$. For a tube with $R = 10$ nm we have $B_0 = 13.2$ T. Since the total flux is given by the sum of the two contributions, it is clear that chirality effects can always be absorbed by the appropriate adjustment of B, and therefore we consider only Φ_2. Since the mass term in Eq. (2.4) couples in the same way as $k_\perp$, we can replace

$$\omega_n \to \omega_n + 2\pi\Phi_2/\beta = (n + B/B_0)/R \tag{2.5}$$

in Eq. (2.4) in order to include the mass term. The magnetic flux Φ_2 through the NT therefore gives rise to an Aharonov-Bohm phase modifying the boundary condition of the transverse wavevector. Since n is integer, it is clear that for integer Φ_2, the accumulated phase due to the magnetic field can be absorbed into the definition of the azimuthal quantum number n and the system remains unaffected. In particular, there exists an azimuthal state $n = -\Phi_2$ for which the mass term vanishes, and the electronic spectrum is gapless.

2.3 Disorder mechanisms

Real materials always enclose impurities, dislocations, or more general forms of disorder which generally imply to go beyond usual paradigms that have been used successfully for clean systems. To strengthen the usefulness of carbon NTs, the understanding of the influence of defects in nanostructures deserves particular attention since at such small scales, any disruptions of local order may dramatically affect the physical response of the nanodevice. For the implementation of efficient technological devices, one needs to understand, control, and possibly confine the magnitude of these inherent quantum fluctuations, induced by disorder or magnetic field.

2.3.1 General remarks

There are various sources for impurities possible in NTs: structural imperfections like substitutional atoms, charge defects in the substrate, twists, or topological defects. To cover all these effects in a microscopic model, for an effective low-energy theory, three types of randomness should be considered: a random vector potential (or gauge field) $\vec{A}$ as well as two different types of random scalar potentials $\tilde{V}$ and V. The corresponding Hamiltonians are given by

$$H_A = \int d\vec{r}\,\psi^\dagger(\vec{r})\vec{\sigma}\cdot\vec{A}(\vec{r})\psi(\vec{r})\;, \tag{2.6}$$

$$H_{\tilde{V}} = \int d\vec{r}\,\tilde{V}(\vec{r})\psi^\dagger(\vec{r})\sigma_z\psi(\vec{r})\;, \tag{2.7}$$

$$H_V = \int d\vec{r}\,V(\vec{r})\psi^\dagger(\vec{r})\psi(\vec{r})\;, \tag{2.8}$$

where the fields $\vec{A}, \tilde{V}$, and V are random in space but constant in time ("quenched disorder"). Thus, they mix up the momenta but not the frequencies. Further, the three random fields are assumed to have zero mean, $\langle O(\vec{r})\rangle = 0$, and a Gaussian white noise distribution for the fluctuations, $\langle O(\vec{r})O(\vec{r}\,')\rangle = \Delta_O \delta(\vec{r}-\vec{r}\,')$, where Δ_O is the disorder strength[1] for the field O corresponding to $\vec{A}, \tilde{V}$, and V, respectively. The assumption of delta-correlation is equivalent to assuming that the individual scatterers are point-like and hence isotropic.

Focusing on disorder contributions of the inner-shell potentials, we can expand these fields in terms of reciprocal lattice vectors $\vec{G}$ of the inner shells. Note that these are different from the ones of the outermost shell, since inner shells have different radii and chiralities. In particular, to obtain sizeable scattering between the two K points, the Fourier component of these random fields at $\vec{G} = 2\vec{K}$ should be finite. As $2\vec{K}$ is normally not an allowed reciprocal lattice vector on inner shells, scattering between the two distinct K points is expected to be drastically suppressed. From this observation, we then restrict ourselves to the single-K-point problem. Let us now comment on the physical significance of the three disorder terms.

2.3.2 Topological disorder and random vector potential

Topological defects are dislocations (kinks) that locally change the superlattice vector $\vec{T}$ by replacing one of the hexagons in the graphene network by a pentagon or heptagon. Pentagons, e.g., can be viewed as disclinations in the lattice, and, when circling one such defect, the two sublattices in the honeycomb structure are exchanged (see Fig. 2.1), as well as the fermion flavors. The scheme to incorporate this change in a continuum description was discussed in [41] and shown to be described by means of a non-Abelian gauge field, which rotates the spinors describing the electrons in flavor space. The vector potential is that of a vortex at the position of the defect, and the flux is $\pm\pi/2$. Thus, a random distribution of topological defects can be described by a (non-Abelian) random gauge field.

A random vector potential can also be caused by indirect hopping between nearest-neighbor sites on the honeycomb lattice via real or virtual states provided by the inner-shell ionic potential. Since hopping connects different sublattices, the resulting modulation of the hopping matrix element leads to the random gauge field.

The nature of the electronic states derived from the 2D Dirac equation in the presence of a gauge field with Gaussian randomness has received a great deal of attention, as it also describes the effects of disorder in integer quantum Hall transitions or d-wave superconductors [42, 43]. Concerning the NTs, we have to investigate the influence of a random vector potential on a system controlled by the Dirac Hamiltonian (2.4).

[1] For not too high energies, the disorder strength can be considered to be constant.

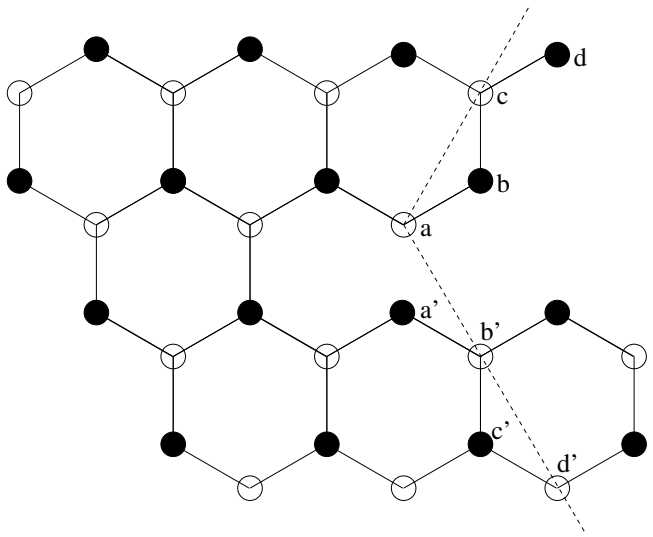

Figure 2.1: *Formation of a pentagonal ring in the honeycomb lattice where the two sublattices are represented by the filled and unfilled circles. The points* $a, b, c, \ldots$ *have to be identified with the points* $a', b', c' \ldots$. *The defect can be seen as a disclination, defined by the dashed lines.*

2.3.3 Random chemical potential

Both $H_{\tilde{V}}$ and H_V correspond to a random chemical potential. They arise from direct impurity potential scattering processes that are diagonal in sublattice space. The potential $\tilde{V}$ is short-ranged and resolves the sublattice structure while V is long-ranged and therefore does not distinguish between different sublattices. Using the standard replica trick to average over disorder, the two kinds of potential scattering can be mapped onto each other with the correspondence $\Delta_{\tilde{V}} \leftrightarrow -\Delta_V$ [42]. Here, we focus only on H_V since the $\tilde{V}$ term is, technically speaking, irrelevant under a renormalization group procedure. In particular, when the MWNT is intrinsically damaged by fast ion bombarding, the dominant disorder mechanism is expected to be due to standard potential scattering H_V [7, 10].

2.4 Diagrammatic perturbation theory

In this section we will briefly discuss the basics of diagrammatic perturbation theory as far as it is necessary to understand the computations in Chapter 3. For further details, the reader is referred to the literature, see for example [44]. We will consider only a non-interacting system.

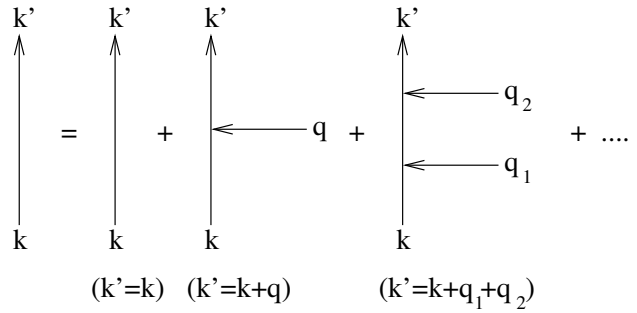

Figure 2.2: *Diagrammatic representation of the perturbation series for the Greens function in Eq. (2.9).*

2.4.1 Perturbation expansion for the Greens function

The diagrammatic perturbation theory provides an elegant analytical method for computing ensemble averages. In the presence of a scattering potential U we can expand the Greens function in a perturbation series,

$$\begin{aligned} G(\vec{k}',\vec{k}) &= \delta_{\vec{k}'\vec{k}} G_0(\vec{k}) + G_0(\vec{k}') U(\vec{q}) G_0(\vec{k}) \\ &\quad + G_0(\vec{k}') U(\vec{q}_1) G_0(\vec{k}+\vec{q}_2) U(\vec{q}_2) G_0(\vec{k}) + \dots \ , \end{aligned} \tag{2.9}$$

where G_0 is the Greens function of the clean system and the matrix elements of the scattering potential depend only on the difference between the wavevectors, $U(\vec{q}) \equiv U(\vec{k}'-\vec{k}) = U(\vec{k}',\vec{k})$. This perturbation series can be depicted as shown in Fig. 2.2, noting that the wavevectors must add up to satisfy the relations

$$\vec{k}\,' = \vec{k} \quad \text{or} \quad \vec{k}\,' = \vec{k}+\vec{q} \quad \text{or} \quad \vec{k}\,' = \vec{k}+\vec{q}_1+\vec{q}_2 \ ,$$

which is nothing else but momentum conservation.

What is special about this perturbation series is that only momentum is transferred but there is no transfer of energy and hence, no need to consider time. The energy is just a parameter. A crucial point is that in contrast to interacting systems, in non-interacting disordered systems there appear no loops in the Greens function.

2.4.2 Ensemble-averaging

The Greens function is different for each individual phase-coherent unit of the whole system since the scattering potential is different. The ensemble-average is calculated by averaging over all the phase-coherent units assuming appropriate statistical properties for the random scattering potential. In particular we will assume that the scattering potential has zero mean and is delta-correlated (Gaussian white noise),

$$\langle U(\vec{r})\rangle = 0 \quad \text{and} \quad \langle U(\vec{r})U(\vec{r}\,')\rangle = \Delta\delta(\vec{r}-\vec{r}\,') \ ,$$

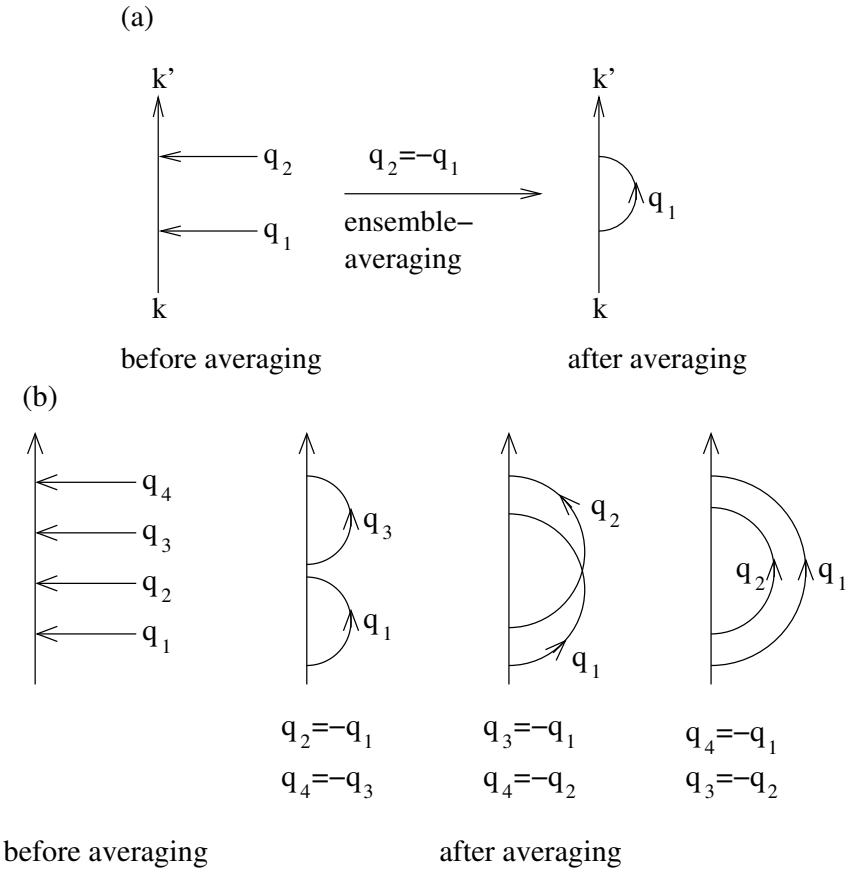

Figure 2.3: *Ensemble-averaging results in tying together the scattering lines in pairs. For diagrams with two scattering lines there is only one possibility as depicted in (a). For diagrams with four scattering lines the resulting three possibilities are shown in (b). The first diagram is reducible and separates into two first order diagrams while the second (crossed) and third (rainbow) diagram are irreducible.*

i.e., the individual scatterers are point-like and hence isotropic. In momentum representation this corresponds to

$$\langle U(\vec{q})\rangle = 0 \quad \text{and} \quad \langle U(\vec{q})U(\vec{q}\,')\rangle = \Delta\delta_{\vec{q},-\vec{q}'} \; . \tag{2.10}$$

We can then calculate the ensemble-averaged Greens function simply by ensemble-averaging the perturbation series term by term. Using the statistical property (2.10), the second term of Eq. (2.9) averages to zero, $\langle G_0(\vec{k}\,')U(\vec{q})G_0(\vec{k})\rangle = 0$, while the third term averages to a non-zero value only if $\vec{q}_2 = -\vec{q}_1$,

$$\langle G_0(\vec{k}\,')U(\vec{q}_1)G_0(\vec{k}+\vec{q}_2)U(\vec{q}_2)G_0(\vec{k})\rangle = \Delta G_0(\vec{k})G_0(\vec{k}-\vec{q}_1)G_0(\vec{k}) \; .$$

Diagrammatically, we can represent the effect of averaging by connecting together the scattering lines in pairs as shown in Fig. 2.3. Each such closed scattering line

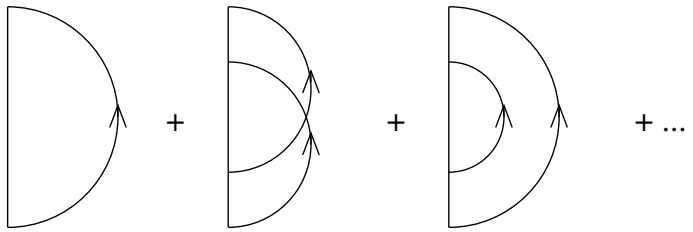

Figure 2.4: *Examples of diagrams included in the self energy. Shown are the first (Born approximation) and second order diagrams.*

contributes a factor of Δ to the diagram. Any diagram with one or more free scattering lines that is not connected to another diagram vanishes on ensemble-averaging.

2.4.3 Self energy

It is useful to define a self energy function Σ as the sum of all diagrams of the type shown in Fig. 2.4. Then, any diagram contributing to the ensemble-averaged Greens function can be represented by sandwiching self energy diagrams between free propagators G_0. This allows us to express the Greens function in the form

$$\langle G \rangle = G_0 + G_0 \Sigma G_0 + G_0 \Sigma G_0 \Sigma G_0 + \dots \ ,$$

which is a geometric series and can be summed leading to $\langle G \rangle = G_0(1 - \Sigma G_0)^{-1}$ which is equivalent to $\langle G \rangle^{-1} = G_0^{-1} - \Sigma$, known as the Dyson equation. In order to avoid double counting, one has to sum only over irreducible diagrams, i.e., diagrams which cannot be divided into two sub-diagrams joined only by a single G_0 line (see Fig. 2.3).

It is easy to see that as a result of ensemble-averaging all the off-diagonal elements of the Greens function vanish, so that we have

$$\langle G(\vec{k}, \vec{k}') \rangle = \delta_{\vec{k},\vec{k}'} G(\vec{k}) \ .$$

In general, the self energy function has both real and imaginary parts. The physical meaning of the self energy is that the scattering shifts the energy eigenvalues via the real part of Σ, while the imaginary part of Σ causes the Greens function to decay with time. So, in general, the poles of the Greens function in the complex plane determine the excitation energy as well as the lifetime of the quasi-particle excitations.

Chapter 3

Van Hove singularities in disordered multi-wall nanotubes

We now present a theory for the van Hove singularities in the tunneling density of states of disordered multi-channel quantum wires, with particular focus on MWNTs. We answer the question: How is the van Hove singularity modified by the presence of disorder? This question is of importance for the interpretation of many experiments on MWNTs.

We start by pointing out the general relevance of van Hove singularities and also comment on experimental results that are in close context to our studies. After these introductory remarks we discuss the relevant assumptions we made in our model. Then, after discussing the case of a clean tube, we analyze the disordered case in detail. Finally, we close by giving some conclusions. Some of the results presented in this chapter have been published in [45].

3.1 Introduction

3.1.1 Van Hove singularities

Because of its relevance for the understanding and interpretation of spectroscopy data of NTs, we now discuss van Hove singularities (VHS's). VHS's in the thermodynamic density of states (DOS) have been predicted in 1953 [46] and were observed in many experiments since then. The DOS for a d-dimensional system with dispersion relation $E(\vec{k})$ is by definition

$$\nu(E) = \int \frac{d\vec{k}}{(2\pi)^d} \delta(E - E(\vec{k})) \ ,$$

and can be rewritten as a surface integral over $E(\vec{k}) = E = const$,

$$\nu(E) = \int \frac{dS}{(2\pi)^d} \frac{1}{|\nabla_{\vec{k}} E(\vec{k})|} \ .$$

The quantity in the denominator is basically the group velocity. Due to symmetries in a crystal, the group velocity may vanish at certain momenta which, of course, can happen in all dimensions. In 1D or 2D systems, however, this results in a divergent integrand (as a manifestation of confined states).

Van Hove pointed out that the existence of such saddle-points in the dispersion relation $E(\vec{k})$, far from being accidental, are necessarily implied by the periodic structure of the lattice. According to a general theorem of M. Morse [47], any function of more than one independent variable which, as $E(\vec{k})$, is periodic in all its variables has at least a certain number of saddle points. This number is determined by topological considerations and depends only on the number of independent variables. It is this mathematical fact which accounts for the occurance of singularities in the DOS of 1D and 2D systems. In three dimensions, the corresponding divergencies are integrable, typically leading to a finite DOS. Since we are primarily interested in NTs, we will, in the subsequent sections, focus only on the 1D limit, where the VHS in a clean system diverges like $1/\sqrt{E-E_n}$ when approaching the threshold E_n from above. Therefore, VHS's appear as sharp features in the DOS, at energies where the bottom or top of 1D subbands are located, reflecting the onset of new active subbands (Fig. 3.1).

Similar VHS's exist for the tunneling density of states (TDOS) measured at some location x along the system,

$$\nu(E,x) = \frac{\mathrm{Re}}{\pi\hbar} \int_0^\infty dt\, e^{iEt/\hbar} \langle \psi(x,t)\psi^\dagger(x,0)\rangle \;, \tag{3.1}$$

where $\psi(x,t)$ is the electron field operator and the brackets denote a quantum expectation value. The TDOS is easily accessible experimentally via the conductance through a weak link or a tunnel junction. More typically, it is measured by means of STS on which we already commented in Sec. 1.5. Corresponding experimental results on NTs will be discussed in the next section.

In general, one has to carefully distinguish between the DOS and the TDOS. While the DOS is a thermodynamic property of the system, the TDOS is a local property and therefore depends on the position. In the "bulk" limit, the DOS and the (possibly coarse-grained) TDOS are expected to lead to identical results, but near a boundary they can strongly differ.

3.1.2 Experimental results

One-dimensional VHS's are important for determining many solid state properties of NTs, such as optical absorption, resonant Raman spectroscopy, and the spectra observed by tunneling measurements on which we will focus exclusively in our discussion below.

The observation of VHS's in recent STS experiments on SWNTs on a metallic substrate represents a direct proof for the 1D band structure [12, 13, 27, 28].

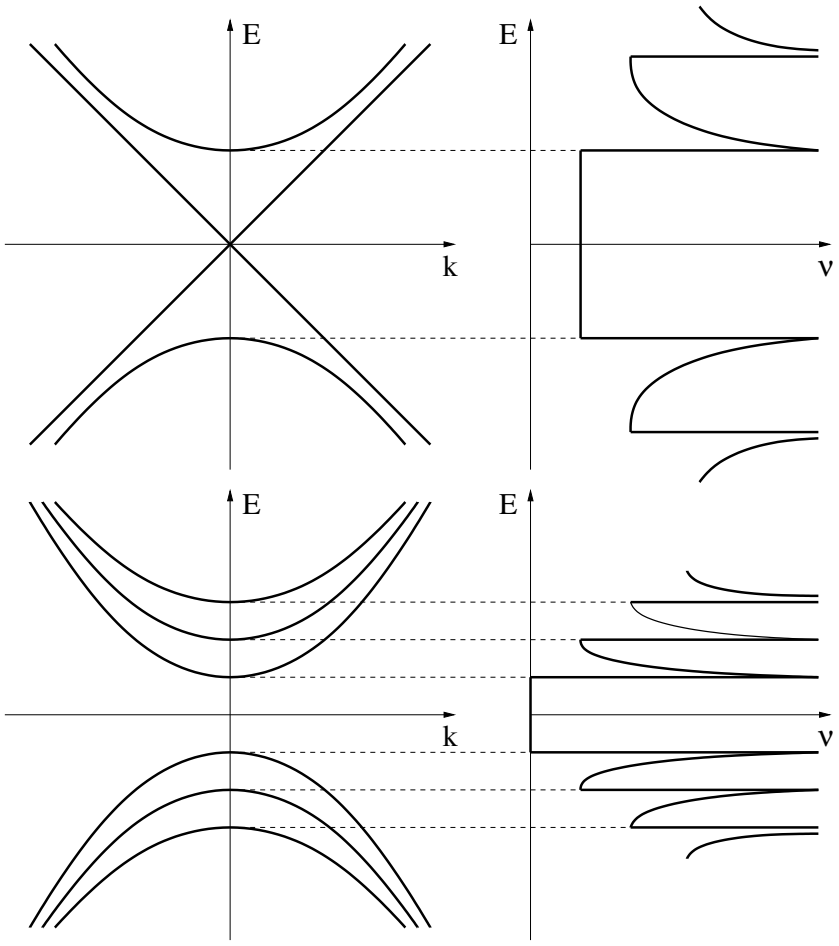

Figure 3.1: *Dispersion relation $E(\vec{k})$ (left) and DOS $\nu(E)$ (right) for a metallic (top) and a semiconducting (bottom) NT. The sharp peaks in the DOS correspond to VHS's at the onset of new subbands as is indicated by the dashed line.*

By moving the STM tip along the length of a NT, sharp deviations in the $I-V$ characteristics could be observed and related to theoretically predicted electronic properties, in particular the $1/\sqrt{E-E_n}$ behavior of VHS's in ballistic 1D wires, see Fig. 3.2. With regard to MWNTs, we then need to understand how VHS's develop in the presence of and with increasing amounts of disorder.

In other tunneling spectroscopy experiments the differential conductance was measured also on a single MWNT [48], see Fig. 3.3. There is a substantial DOS at the Fermi energy ($V=0$) indicating that the NT is metallic. The almost symmetric peak structure (corresponding to VHS's) is caused by the additional 1D subbands in the valence ($V<0$) and conduction ($V>0$) band with threshold energies of order ≈ 50 meV. The distance between the two first-order subbands is found to be $\Delta E \approx 0.12$ eV which predicts a diameter of 19 nm in good agreement with the measured diameter of 17 nm.

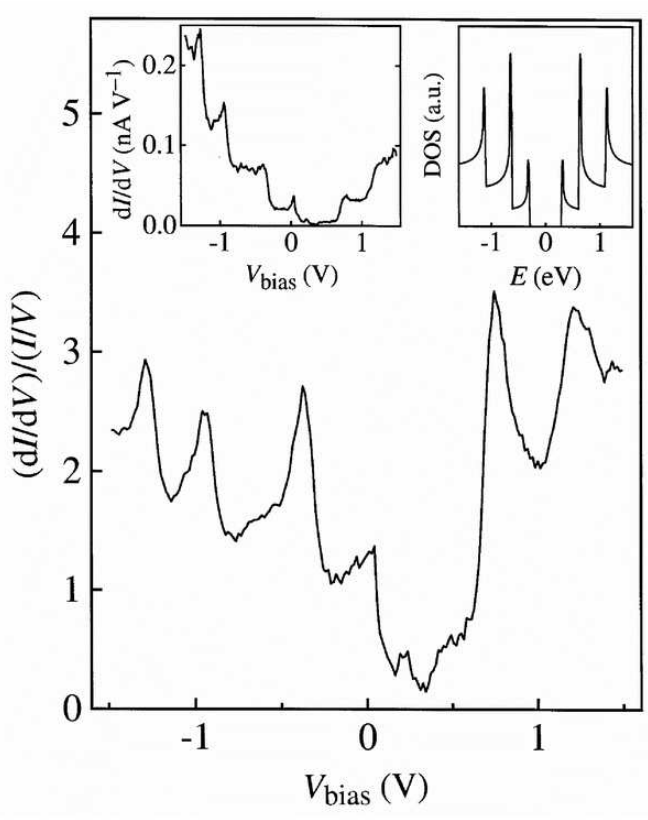

Figure 3.2: *Normalized differential (tunneling) conductance* $(dI/dV)/(I/V)$ *(which is a measure for the TDOS) versus bias voltage for a semiconducting SWNT. The asymmetric peaks correspond to VHS's at the onset of 1D energy bands of the NT. The left inset displays the raw* dI/dV *data, and the right inset the calculated TDOS for a (16,0) tube. The experimental peaks have a finite height and are broadened, which could be attributed to hybridization between the wavefunctions of the tube and the gold substrate. However, the overall shape of the experimental peaks still resembles that predicted by theory. (From [13].)*

The spectrum in Fig. 3.3 agrees remarkably well with the STS measurements for SWNTs (Fig. 3.2) but the broadening of the VHS's observed in MWNTs has probably a different origin than in SWNTs since MWNTs are not ballistic. The observation of VHS's demonstrates that the mean free path l cannot be much shorter than the NT circumference since for $l \ll 2\pi R$, all 1D band structure features would be expected to be washed out. Therefore, all the observed results can be consistent only if the mean free path is of the order of the circumference; not much larger, but also not much smaller. Transport in MWNTs has therefore to be characterized as quasi-ballistic. Hence, for typical MWNTs with $l \approx 2\pi R$, the characteristic subband features of the DOS should still be present, albeit considerably broadened and possibly shifted.

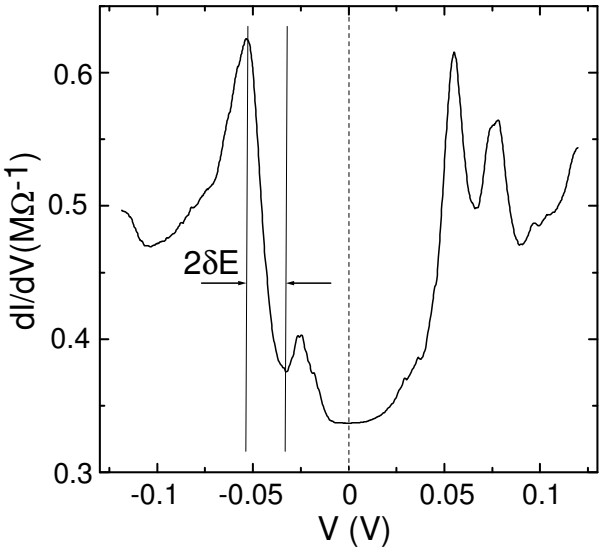

Figure 3.3: *Differential (tunneling) conductance dI/dV (which is a measure for the TDOS) measured on a single MWNT using a high-ohmic contact (300 kΩ) at $T = 4.2$ K. δE denotes the sharpness of the the observed VHS. Positive (negative) voltages correspond to empty (occupied) NT states. (Taken from [48].)*

Thus, for the interpretation of the measured spectrum it would be useful to know how VHS's are influenced by the presence of disorder, which is investigated in detail in Sec. 3.5. This question is clearly also of relevance to other quasi-1D quantum wires, such as long chain molecules.

3.2 Formulation of the problem

We consider a MWNT and assume that the electron-electron interaction is screened off by working on a metallic substrate which is typical for the experimental setup of STS measurements. For that reason, we can safely neglect interactions and treat only the non-interacting problem. Then, spin only contributes trivial factors of two and is ignored henceforth. In particular, it will not affect the TDOS apart from the overall prefactor of two. Additionally, disorder-induced scattering between the two distinct K points should be largely suppressed for reasons given in Sec. 2.3.1, and we thus consider only one K point. It should be stressed that in typical STS experiments, only the TDOS of the outermost shell is probed and hence, we assume in the following an effective single-shell model where inner shells only give rise to a disorder potential for electrons on the outermost shell. We are then left with the problem of determining the TDOS for (one species of) non-interacting disordered Dirac fermions on a cylinder. As we show below, an approximate yet accurate analytical solution to this problem can be given.

The corresponding problem on the plane is related to other applications, e.g., disordered d-wave superconductors or quantum Hall transitions, and has been addressed before by many authors [41, 42, 43, 49, 50]. However, the techniques used in these papers do not allow to directly address the question of relevance here, since they appear to be restricted to the true 2D limit.

In addition to the bulk case, we also address the *boundary TDOS* arising when one tunnels into the end of a MWNT. In reality, the end TDOS could of course be quite complex due to the formation of bound states. A few lattice spacings away from the end, however, we expect that the situation can be described by a continuum model, where bound state effects are negligible. Surprisingly, the presence of a boundary implies a drastic change in the TDOS despite the absence of electron-electron interactions, namely a strong suppression of the energy-dependent TDOS close to the boundary even in the absence of disorder, as will be shown below.

To make progress, we will now introduce an appropriate representation of the TDOS using the Greens function formalism. In terms of an Euclidean coherent-state path integral approach (we assume $T = 0$), the generating functional for the Greens function (partition function) is given by

$$Z = \int \mathcal{D}\psi^\dagger(\omega,\vec{k})\mathcal{D}\psi(\omega,\vec{k})\ \exp[S_0] = \prod_\omega Z_\omega\ ,$$

where the action S_0 corresponds to the Dirac Hamiltonian (2.4),

$$S_0 = \frac{1}{\beta}\sum_n \int \frac{d\omega}{2\pi}\frac{dk}{2\pi}\ \psi^\dagger(\omega,\vec{k})(i\omega - \vec{\sigma}\cdot\vec{k})\psi(\omega,\vec{k})\ .$$

Note that Z factorizes in ω even in the presence of a static disorder potential, as long as electron-electron interactions can be disregarded[1] [42, 43]. Hence, for a computation of the TDOS (this expression follows directly from Eq. (3.1)),

$$\nu(E,x) = -\frac{\mathrm{Im}}{\pi}\ \mathrm{Tr}_\sigma \langle\psi^\dagger(\vec{r})\psi(\vec{r})\rangle|_{i\omega\to E+i0^+}\ , \tag{3.2}$$

where the trace is over "spin-coordinates" in sublattice space, only the mode at a given frequency ω needs to be considered, and all other frequencies decouple. Then ω is simply a parameter of the theory, and the relevant action is

$$S_\omega = \frac{1}{\beta}\sum_n \int \frac{dk}{2\pi}\psi^\dagger(\vec{k})(i\omega - \vec{\sigma}\cdot\vec{k})\psi(\vec{k})\ . \tag{3.3}$$

Introducing the Greens function $G(E,\vec{k},x)$ via

$$\langle\psi^\dagger(\vec{r})\psi(\vec{r})\rangle|_{i\omega\to E+i0^+} = \mathrm{Tr}_{\vec{k}} G(E,\vec{k},x)\ , \tag{3.4}$$

[1] This is clear since when there are no genuine interactions between the fermions we can describe them in terms of exact energy eigenstates in the random potential.

the TDOS (3.2) reads

$$\nu(E,x) = -\frac{\mathrm{Im}}{\pi}\mathrm{Tr}_{\vec{k},\sigma} G(E,\vec{k},x) \ , \tag{3.5}$$

where the trace over momentum is defined by

$$\mathrm{Tr}_{\vec{k}} = \sum_n \int_{-\infty}^{\infty} \frac{dk}{2\pi} \ .$$

Prefactors in the Greens function are always chosen in order to recover the correct 1D normalization for the clean TDOS in the single-channel limit. Further, due to the symmetry of the TDOS, $\nu(-E) = \nu(E)$, within our model, we consider only $E > 0$. In all figures shown below, we take $R = 10$ nm, which is typical for arc discharge grown tubes, but qualitatively similar findings were obtained for other R as well, and the general equations are of course valid for any R. The subband spacing (which gives the distance between two neighboring VHS's), used as an intrinsic energy scale of the system, is then $D = \hbar v_F/R \approx 53$ meV.

3.3 Clean case

To be able to calculate both bulk and boundary TDOS, we study a semi-infinite ($x \geq 0$) tube, assuming a hard-wall potential at the boundary $x = 0$. This leads to the expansion

$$\psi(x,\tau) = \frac{1}{\beta}\sum_n \int_0^{\infty} \frac{dk}{\pi} \ \sin(kx) e^{i\omega_n \tau} \psi(k,\omega_n) \ ,$$

and together with the action (3.3) we readily find

$$\langle \psi^{\dagger}(\vec{r})\psi(\vec{r})\rangle = \sum_n \int_0^{\infty} \frac{dk}{2\pi} \frac{4\sin^2(kx)}{i\omega - \vec{\sigma}\cdot\vec{k}} \ ,$$

where we have already anticipated the correct 1D normalization. Hence, according to (3.4), the Greens function for energy $E > 0$ is defined as

$$G_0(E,\vec{k},x) = \frac{2\sin^2(kx)}{E - \vec{\sigma}\cdot\vec{k} + i0^+} \ . \tag{3.6}$$

It order to compute the TDOS (3.5), we explicitely write down the Greens function (3.6) as a matrix in 2×2 sublattice space,

$$G_0(E,\vec{k},x) = \frac{2\sin^2(kx)}{(E+i0^+)^2 - \vec{k}^2} \begin{pmatrix} E+i0^+ & k - iE_n \\ k + iE_n & E+i0^+ \end{pmatrix} .$$

Tracing over sublattice coordinates we have

$$\mathrm{Tr}_{\sigma} G_0(E,\vec{k},x) = \frac{4E\sin^2(kx)}{E^2 - k^2 - E_n^2 + i0^+} \ , \tag{3.7}$$

which can be written in a more convenient way using the Cauchy identity

$$\frac{1}{x+i0^+} = \frac{\mathcal{P}}{x} - i\pi\delta(x) \;, \tag{3.8}$$

where $\mathcal{P}$ denotes the Cauchy principal value. Further, the appearing δ-function can be decomposed into

$$\delta(E^2-k^2-E_n^2) = \frac{\Theta(E^2-E_n^2)}{2\sqrt{E^2-E_n^2}}\left[\delta(k-\sqrt{E^2-E_n^2})+\delta(k+\sqrt{E^2-E_n^2})\right].$$

Using these ingredients together with (3.5) we see that the principal value term of (3.7) does not contribute to the imaginary part and hence, we simply have to integrate over δ-functions,

$$\frac{\nu(E,x)}{\nu_{1\mathrm{D}}} = E\sum_n \int_{-\infty}^{\infty} dk \sin^2(kx) \frac{\Theta(E^2-E_n^2)}{\sqrt{E^2-E_n^2}}\left[\delta(k-\sqrt{E^2-E_n^2})+\delta(k+\sqrt{E^2-E_n^2})\right].$$

The final result then reads (since $\hbar = v_F = 1$ we have $\omega_n = E_n = nD$)

$$\frac{\nu(E,x)}{\nu_{1\mathrm{D}}} = 2E\sum_{n=-\infty}^{\infty} \frac{\sin^2(x\sqrt{E^2-E_n^2})}{\sqrt{E^2-E_n^2}}\Theta(E^2-E_n^2) \;, \tag{3.9}$$

where Θ is the Heaviside step function.[2] Throughout the paper, we use $\nu_{1\mathrm{D}} = 1/\pi\hbar v_F$ as natural unit for the TDOS (without spin and K point degeneracy). As one can see from Eqs. (3.9) and (2.5), the system can be gapped in the presence of a magnetic field B parallel to the tube axis. The gap varies as a function of B, and the pattern is periodic with period B_0 where the system becomes gapless again. Since the summation also includes negative values of n, the magnetic field causes a doubling of the VHS's (see Eq. (2.5) and Fig. 3.4).

3.3.1 Bulk limit

Letting $x \to \infty$, with $\sin^2(x\sqrt{E^2-E_n^2}) \to 1/2$, we obtain the *bulk TDOS* which is equal to the thermodynamic DOS (see also Ref. [51]),

$$\frac{\nu_0(E)}{\nu_{1\mathrm{D}}} = E\sum_n \frac{\Theta(E^2-E_n^2)}{\sqrt{E^2-E_n^2}} \;. \tag{3.10}$$

In the absence of a gap, the bulk TDOS approaches a constant and finite value for $E \to 0$, since then only $n = 0$ is possible. Clearly, the typical $1/\sqrt{E-E_n}$ VHS's of 1D systems appear at the onset of new subbands, $E = E_n$, see Fig. 3.4. We also want to mention that within the linear $\vec{k}$-approximation for the energy dispersion relation of graphene, the energy positions of the VHS's do not depend on the chirality but only on the diameter of the tube.

[2] Result (3.9) can be readily checked from the dispersion relation for Dirac fermions, $E(\vec{k}) = \sqrt{k^2+\omega_n^2}$, by using the alternative Greens function $\bar{G}_0(E,\vec{k},x) = \frac{2\sin^2(kx)}{E-E(\vec{k})+i0^+}$ instead of Eq. (3.6).

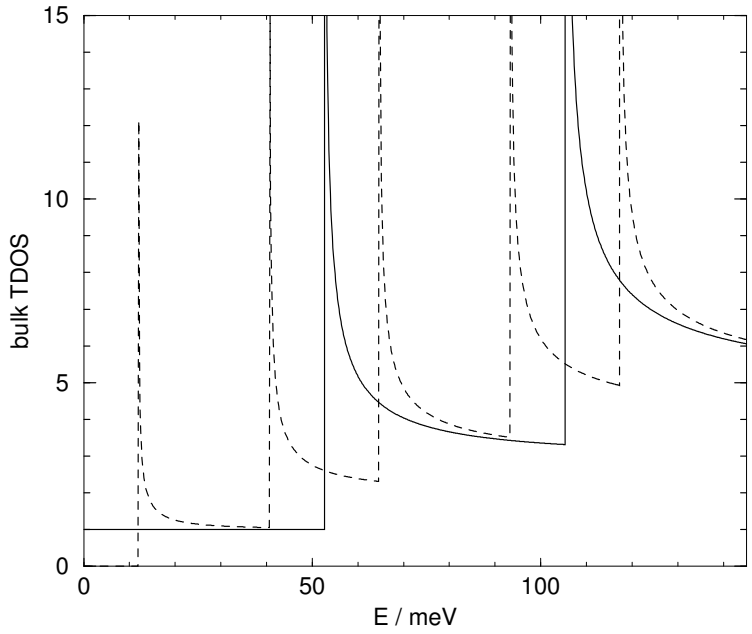

Figure 3.4: *Bulk TDOS of a clean tube. Without magnetic field the system is gapless and the bulk TDOS is finite for $E \to 0$ (solid curve). VHS's appear at the onset of new subbands. With magnetic field ($B = 3$ T), the system is gapped and the VHS's are doubled (dashed curve). The shift associated with the doubling of the VHS's is linear in B, see Eq. (2.5).*

3.3.2 Boundary limit

Near the boundary, however, we obtain a completely different picture than predicted by the standard VHS of the thermodynamic DOS. Expanding the sine in Eq. (3.9), $\sin^2(x\sqrt{E^2 - E_n^2}) \to x^2(E^2 - E_n^2)$, leads to the *boundary TDOS*

$$\frac{\nu_{\rm end}(E,x)}{\nu_{\rm 1D}} = 2x^2 E \sum_n \Theta(E^2 - E_n^2)\sqrt{E^2 - E_n^2}\,. \tag{3.11}$$

For $E < D$ and $B = 0$, this predicts $\nu(E) \sim E^2$ and hence, a vanishing TDOS for $E \to 0$ in contrast to the finite boundary TDOS of a doped tube. This behavior can be traced back to the linear dispersion relation of Dirac fermions. More interestingly, the typical 1D VHS of the bulk TDOS is drastically altered close to the boundary. Instead of a divergence, the only sign of the opening of new subbands is a non-analyticity at the threshold energy E_n, with a *square-root energy dependence of the boundary TDOS* above the threshold, see Fig. 3.5. Nevertheless, the phenomenon of an altered energy dependence of the boundary compared to the bulk TDOS close to a given VHS is quite general. The exponent governing the energy dependence of the TDOS above the threshold changes by one if we go from the bulk to the boundary limit, for both Dirac and Schrödinger fermions. In the limit $E \to 0$ (i.e., for $E < D$),

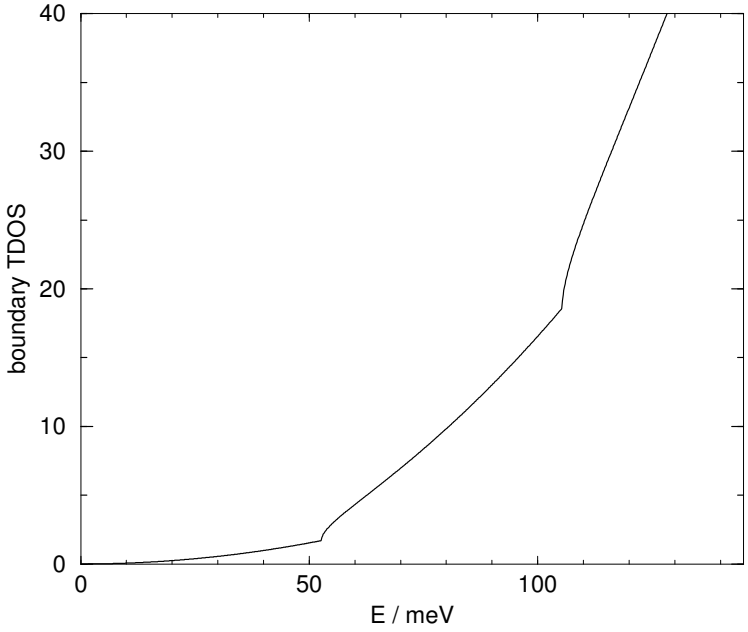

Figure 3.5: *The boundary TDOS of a clean tube exhibits a square-root non-analyticity instead of a divergence at the onset of new subbands, and vanishes* $\sim E^2$ *for* $E \to 0$. *Here, the scale is arbitrary since it depends on the precise distance to the boundary.*

however, there is a difference. For Dirac fermions, the exponent changes by two, whereas for Schrödinger fermions, the exponent still changes only by one (see Table 3.1).[3]

Looking at the boundary TDOS on a larger energy scale we find another interesting property. The non-analyticities then become less important and the sum in (3.11) can be replaced by an integral,

$$\nu(E) \sim E \int_{-E}^{E} d\epsilon \, \sqrt{E^2 - \epsilon^2} \sim E^3 \, ,$$

which leads to a cubic behavior of the TDOS, in contrast to the quadratic one for small energies. When we take into account the band cutoff, $n \leq N$, that is naturally given from the band structure, then the above relation holds for $E < ND$. For larger energies, the boundary TDOS again approaches a quadratic behavior in the limit $E \to \infty$.

The spatial crossover scale x^* between bulk and boundary behavior of the TDOS depends on energy. Focusing on E close to but above a given threshold E_n, this scale is

$$x^* \approx \frac{\hbar v_F}{\sqrt{E^2 - E_n^2}} \, .$$

[3]Using the Greens function $\bar{G}_0 = \frac{2\sin^2(kx)}{E - E(\vec{k}) + i0^+}$ with the dispersion relation for Schrödinger fermions, $E(\vec{k}) = k^2/2m + E_n$, one finds for the TDOS $\nu(E,x) \propto \sum_n \frac{\sin^2(x\sqrt{E-E_n})}{\sqrt{E-E_n}} \Theta(E - E_n)$.

	bulk	end
Dirac	$\sim 1/\sqrt{E-E_n}$	$\sim \sqrt{E-E_n}$
Schrödinger	$\sim 1/\sqrt{E-E_n}$	$\sim \sqrt{E-E_n}$
$E \to 0$		
Dirac	const.	$\sim E^2$
Schrödinger	$\sim 1/\sqrt{E}$	$\sim \sqrt{E}$

Table 3.1: *Energy dependence of the bulk/boundary TDOS for Dirac and Schrödinger fermions in the vicinity of a VHS (above the threshold E_n) and in the limit $E \to 0$.*

At $T = 0$, the bulk limit is reached for $x \gg x^*$, and the boundary limit for $x \ll x^*$. Because of the energy dependence of x^*, one could effectively use E to tune from the bulk to the boundary limit for a given position x. For finite temperatures T, if the thermal scale $x_T = \hbar v_F / k_B T$ is smaller than x^*, one should replace x^* by x_T.

3.4 Disordered case: theory

In this section, we compute the TDOS of a disordered MWNT using diagrammatic perturbation theory [44]. We will consider only the effects of static disorder as introduced in Sec. 2.3. Showing that the Born approximation breaks down close to the VHS, we have to sum the whole perturbation series. Within a non-crossing approximation (NCA) this can be done by using a self-consistent resummation technique leading to Eq. (3.18) which is the central result of this section. Using this result, we give an *a posteriori* justification for the NCA.

3.4.1 General remarks

It is known that disorder often has a profound influence on transport properties but only weakly affects the TDOS. The latter is no longer true, however, if the TDOS of the clean system vanishes linearly, $\nu(E) \sim E$, as is the case for 2D Dirac fermions, e.g., for a graphite sheet or a 2D d-wave superconductor [42, 43]. In the latter case, the standard procedure of averaging over disorder is complicated by the appearance of logarithmic singularities in the perturbative expansion of the single-electron self energy. The lowest-order Born approximation, see Fig. 3.6, is then given by $\Sigma^{(1)}(E) \sim E \ln E$ [43]. The second-order rainbow diagram, which is obtained by first-order renormalization of the internal electron line, contains an even stronger singularity, $\Sigma^{(2)}(E) \sim E \ln^2 E$. The diagram with crossing impurity lines corresponds to a vertex renormalization in the Born self energy diagram, leading to the same singularity as the rainbow diagram. In fact, logarithmic singularities appear in all orders of perturbation theory, including crossed diagrams. Therefore, in the 2D case, crossed diagrams must be treated on the same footing as the rainbow

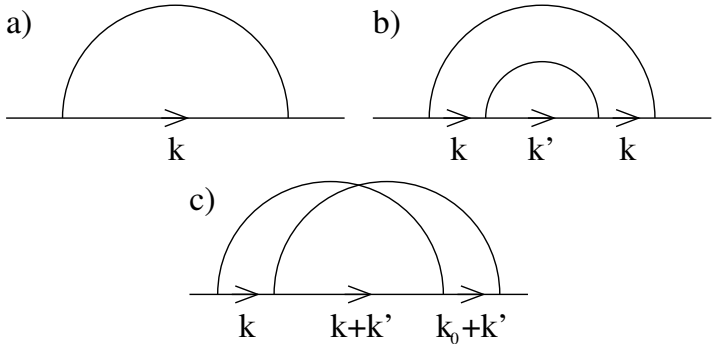

Figure 3.6: *First (a) and second (b,c) order self energy diagrams after disorder averaging. The straight line represents the bare propagator G_0, while the semi-circle line represents the disorder potential scattering. In the vector model, each vertex contributes an additional factor σ_μ, where one has to sum over $\mu = x, y$. Compared to the crossed diagram c), the rainbow diagrams a) and b) have no dependence upon external momentum $\vec{k}_0$.*

ones. In addition, in the single-channel 1D limit, it is also well known that crossed diagrams may be important. Since MWNTs are in-between the 1D and 2D limit, a careful study of the influence of crossed diagrams is mandatory.

As we will show in this section, the situation for MWNTs is quite different from the one in 2D as described above. First, there are *no logarithmic singularities* appearing in the self energy expansion. Second, a further simplification is provided by the fact that crossed diagrams are suppressed compared to the rainbow ones over a wide parameter and energy range of practical interest. Therefore, we are entitled to compute the TDOS within NCA. For simplicity, we focus on the bulk case here and, instead of Eq. (3.6), we then have

$$G_0(E, \vec{k}) = \frac{1}{E - \vec{\sigma} \cdot \vec{k} + i0^+} \; . \tag{3.12}$$

3.4.2 Born approximation

We start by looking at the self energy to lowest order in the disorder strength (Born approximation). Considering standard potential scattering (2.8), a scalar model emerges and the impurity averaging procedure gives [44]

$$\Sigma_V^{(1)}(E) = \Delta_V \mathrm{Tr}_{\vec{k},\sigma} G_0(E, \vec{k}) \; . \tag{3.13}$$

This expression exactly corresponds to the diagram (a) in Fig. 3.6. The semi-circle line contributes a factor Δ_V and a closed line means that one has to trace over the internal degrees of freedom, i.e., the sublattice index and the momentum. If one remembers that the straight line represents the bare propagator G_0, Eq. (3.13) can readily be written down. The corresponding expressions for higher-order terms are

found in exactly the same way. Using Eq. (3.12) and the Cauchy identity (3.8), one observes that the principal parts value vanishes, $\int_{-\infty}^{\infty} dk\, \mathcal{P}/(E^2 - E_n^2 - k^2) = 0$, resulting in

$$\Sigma_V^{(1)}(E) = -i\pi\Delta_V \nu_0(E) \;, \tag{3.14}$$

with $\nu_0(E)$ given in Eq. (3.10). Hence, in first order, the self energy is purely imaginary.

If we instead consider the gauge field disorder (2.6), we have to deal with a vector model, leading to additional factors σ_μ at each vertex,

$$\Sigma_A^{(1)}(E) = \Delta_A \mathrm{Tr}_{\vec{k},\sigma} \sum_{\mu=x,y} \sigma_\mu G_0(E,\vec{k})\sigma_\mu \;.$$

It is easily checked that

$$\sum_{\mu=x,y} \sigma_\mu G_0(E,\vec{k})\sigma_\mu = \frac{2E}{E^2 - k^2 - E_n^2 + i0^+}\, \mathbf{1} \;,$$

where $\mathbf{1}$ denotes the 2×2 identity matrix and hence, comparing with Eq. (3.7) we see that

$$2\mathrm{Tr}_\sigma G_0(E,\vec{k}) = \mathrm{Tr}_\sigma \sum_{\mu=x,y} \sigma_\mu G_0(E,\vec{k})\sigma_\mu \;.$$

Therefore, the result for the lowest-order self energy diagram in the vector model is just the same as for standard potential scattering besides an overall factor of two due to the "spin" degree of freedom as well as an additional factor due to the different disorder strength,

$$\Sigma_A^{(1)}(E) = 2\frac{\Delta_A}{\Delta_V}\Sigma_V^{(1)}(E) \;.$$

If we restrict ourselves to rainbow diagrams for the moment, the Nth-order self energy diagram for the scalar model is simply given by

$$\Sigma_V^{(N)}(E) = \Delta_V^N \mathrm{Tr}_{\{\vec{k}_i\},\sigma} G_0^2(E,\vec{k}_1)\ldots G_0^2(E,\vec{k}_{N-1})G_0(E,\vec{k}_N) \;.$$

As one can see, the r.h.s. factorizes completely and using $G_0^2(E,\vec{k}) = -\partial_E G_0(E,\vec{k})$, we arrive at

$$\Sigma_V^{(N)}(E) = \Sigma_V^{(1)}(E)(-\partial_E \Sigma_V^{(1)}(E))^{N-1} \;. \tag{3.15}$$

Apart from the overall factor of two, the same result is again found for the vector model. Within NCA, the special type of disorder is therefore not important. However, it could well be that crossed diagrams are important for the vector model, while we can establish the validity of NCA only for the scalar model (standard potential scattering). Since the latter is expected to represent the dominant disorder mechanism in MWNTs, we shall focus on the scalar model in what follows. Then, a single dimensionless parameter Δ serves as a measure for the disorder strength,

$$\Delta = \frac{\Delta_V R}{\hbar^2 v_F^2} \;.$$

Next, we address the breakdown of the Born approximation in the vicinity of a VHS. If we look at the second-order rainbow diagram in Fig. 3.6, which from Eqs. (3.14) and (3.15) is given by

$$\Sigma^{(2)}(E) = (\pi\Delta_V)^2 \nu_0(E)\partial_E\nu_0(E) \; ,$$

we see that the Born approximation must break down close to a VHS since

$$\left|\frac{\Sigma^{(2)}(E)}{\Sigma^{(1)}(E)}\right| = \pi\Delta_V\partial_E\nu_0(E) \; .$$

The r.h.s. diverges for E approaching the threshold E_n from above. We therefore must address also higher-order contributions to the self energy.

3.4.3 Resummation of the perturbation series

For the moment, we shall assume that one can neglect all crossed diagrams so that we can then treat the problem within NCA. The justification for this will be given *a posteriori* in the next section. But even within NCA, since the perturbation expansion is asymptotic, we have to arrange the order of summation in a physically meaningful way to avoid familiar but unphysical divergencies and inconsistencies. This would also be important for analyzing diagrams beyond NCA, see Ref. [44].

To this end, we follow the self-consistent iterative approach proposed by Lee [52] to calculate the TDOS of the disordered system. Within this approach, the self energy Σ_N including all contributions up to Nth order ($N \geq 1$) is

$$\Sigma_N(E) = \Delta_V \mathrm{Tr}_{\vec{k},\sigma} G_{N-1}(E,\vec{k}) \; , \tag{3.16}$$

with the corresponding Dyson equation

$$G_N^{-1}(E,\vec{k}) = G_0^{-1}(E,\vec{k}) - \Sigma_N(E) \; . \tag{3.17}$$

This form is then used to calculate the self energy Σ_{N+1}. In each order, an average over disorder is performed, and the resulting Greens function is then employed to calculate the next order. In the limit $N \to \infty$, this procedure converges and leads to the equation

$$\Sigma(E) = \Delta_V \mathrm{Tr}_{\vec{k},\sigma} G(E,\vec{k}) = \Delta_V \mathrm{Tr}_{\vec{k},\sigma} \frac{1}{G_0^{-1}(E,\vec{k}) - \Sigma(E)} \; , \tag{3.18}$$

which has to be solved self-consistently for the self energy.

The intuitive and physically appealing form of this result gives further support to this resummation approach. Additionally, in Appendix A we explicitly check that the diagrams up to fourth order are correctly contained in Eq. (3.18). From the analysis there, one can indeed expect that all higher-order terms will also be reproduced correctly. The TDOS then follows directly from Eqs. (3.5) and (3.18),

$$\nu(E) = -\frac{\mathrm{Im}}{\pi\Delta_V}\Sigma(E) \; . \tag{3.19}$$

Importantly, following our analysis, it is not possible to simply assume an energy-independent mean free path for all energies. Since the disorder-averaged Greens function satisfies the Dyson equation, we have an energy-dependent mean free time $\tau(E)$ defined by $-\mathrm{Im}\Sigma(E) = \hbar/2\tau(E)$, and therefore an energy-dependent mean free path $l(E) = v_F\tau(E)$.

3.4.4 Relevance of crossed diagrams

Next, we address the role of crossed diagrams. From the procedure outlined above, let us assume that we have constructed a proper Greens function which includes the effects of all non-crossed diagrams. We now check that the effect of the simplest crossed diagram is small compared to the one of the corresponding rainbow diagram in this order. For computational simplicity, we consider Schrödinger fermions, with the same conclusions expected also for Dirac fermions, especially in the vicinity of the VHS, where the Born approximation breaks down. The lowest-order crossed diagram is then given by

$$\Sigma_c^{(2)}(E,\vec{k}_0) = \Delta_V^2 \mathrm{Tr}_{\vec{k},\vec{k}'} \bar{G}(E,\vec{k})\bar{G}(E,\vec{k}+\vec{k}')\bar{G}(E,\vec{k}_0+\vec{k}') \;, \tag{3.20}$$

where $\vec{k}_0$ is the external momentum, and the Greens function

$$\bar{G}(E,\vec{k}) = \frac{1}{E - E(\vec{k}) - \Sigma(E)} \tag{3.21}$$

includes the effects of all non-crossed diagrams via $\Sigma(E)$. The dispersion relation is $E(\vec{k}) = \vec{k}^2/2m$ since we consider Schrödinger fermions here.

The dominant contribution to Eq. (3.20) comes from momenta with $|\vec{k}| \approx |\vec{k}_0| \approx |\vec{k}+\vec{k}'| \approx |\vec{k}_0+\vec{k}'| = E/v_F$. Therefore, only $k' \approx 0$ and $n' = 0$ give an appreciable contribution to the crossed self energy term $\Sigma_c^{(2)}$.[4] Accordingly, we can neglect terms proportional to k'^2, and a careful analysis of the pole structure leads to

$$\Sigma_c^{(2)}(E,\vec{k}_0) \approx i\Delta_V^2 \frac{m}{k_0} \mathrm{Tr}_{\vec{k}} \bar{G}(E,\vec{k}) \frac{\Theta(-k_0 k)\,\mathrm{sgn}(k_0)}{[E - E(\vec{k}_0) - \Sigma(E)]k/k_0 - [E - E(\vec{k}) - \Sigma(E)]} \;. \tag{3.22}$$

To estimate the contribution of $\Sigma_c^{(2)}$ to the TDOS, one has to add external propagators $\bar{G}(\vec{k}_0)$. In the presence of these external poles, the self energy can be estimated from Eq. (3.22) as

$$\Sigma_c^{(2)}(E,\vec{k}_0) \approx \frac{i\Delta_V}{2v_F} \partial_E \Sigma(E) \;. \tag{3.23}$$

The steps leading to Eqs. (3.22) and (3.23) are explained in Appendix B.

[4] There is a small contribution from $\vec{k}' = -2\vec{k}_0$, but due to its small phase space, $k' \approx 0$ is much more important.

If we compare Eq. (3.23) to the corresponding second-order rainbow diagram, $\Sigma^{(2)}(E) = \Sigma(E)(-\partial_E \Sigma(E))$, we have

$$\left| \frac{\Sigma_c^{(2)}(E, \vec{k}_0)}{\Sigma^{(2)}(E)} \right| \approx \frac{\Delta_V}{2v_F|\Sigma(E)|} \leq \frac{1}{2\nu(E)/\nu_{1\mathrm{D}}} \; . \tag{3.24}$$

Unless there is a gap for small energy, this ratio is always smaller than 1/2. This is, however, a conservative estimate since here we have neglected the real part Σ_R of the self energy, $\Sigma(E) = \Sigma_R(E) - i\pi\Delta_V\nu(E)$, see Eq. (3.19). Incorporating it would simply decrease the ratio (3.24). Obviously, for high energies, i.e., high order n of the VHS, this NCA approach should become exact. But even for the lowest-order VHS it is still expected to be quite accurate in the vicinity of the VHS. We therefore conclude that our NCA-type treatment is highly accurate in describing disorder effects for the VHS in MWNTs. At this point it should be stressed that in the true 2D limit, our arguments leading to Eq. (3.24) are not valid, and therefore no contradiction to Refs. [41, 42, 43, 49, 50] arises.

3.5 Disordered case: results

We now deduce a formula that is appropriate for numerical evaluation. In order to obtain both the bulk and boundary limit, we have to go back to the general (x-dependent) problem. For simplicity we suppress the functional dependencies of the self energy on E and x but keep in mind that we actually have $\Sigma = \Sigma(E, x)$.

Inserting (3.6) into (3.18) we then have

$$\Sigma = 2\Delta_V \mathrm{Tr}_{\vec{k},\sigma} \frac{\sin^2 kx}{E - \vec{\sigma}\cdot\vec{k} - \Sigma} \; .$$

Performing the trace in sublattice space, we are left with an integral,

$$\Sigma = \frac{2\Delta_V}{\pi} \sum_n \int_{-\infty}^{\infty} dk \frac{(E-\Sigma)\sin^2 kx}{(E-\Sigma)^2 - E_n^2 - k^2} \; ,$$

which can easily be done by means of contour integration in the complex plane. The two poles are $k_{1,2} = \pm\sqrt{(E-\Sigma)^2 - E_n^2}$ and, depending on the sign of $E - \Sigma_R$, these poles reside in different half-planes. For $\mathrm{sgn}(E-\Sigma_R) = +1$ we have k_1 in the upper and k_2 in the lower half-plane, whereas for $\mathrm{sgn}(E-\Sigma_R) = -1$ the situation is reversed. Since the sine-function is not bounded in the complex plane we write $\sin^2 kx = 1/2 - (\exp[2ikx] + \exp[-2ikx])/4$ and, closing the contour in either the upper or lower half-plane, the result is

$$\begin{aligned} \Sigma &= -i\Delta D \sum_n \frac{(E-\Sigma)\;\mathrm{sgn}(E-\Sigma_R)}{\sqrt{(E-\Sigma)^2 - E_n^2}} \\ &\times \left(1 - \exp\left[2i\;\mathrm{sgn}(E-\Sigma_R) \frac{x}{R} \frac{\sqrt{(E-\Sigma)^2 - E_n^2}}{D} \right] \right) , \end{aligned} \tag{3.25}$$

where Δ is the dimensionless disorder strength as introduced before. This equation can now be solved numerically and once we know the self energy we can compute the TDOS from Eq. (3.19).

3.5.1 Bulk limit

We start by discussing the results in the bulk limit, $x \to \infty$, where the exponential function in (3.25) vanishes,

$$\Sigma = -i\Delta D \sum_n \frac{(E-\Sigma)\,\mathrm{sgn}(E-\Sigma_R)}{\sqrt{(E-\Sigma)^2 - E_n^2}} \,. \tag{3.26}$$

According to Eq. (3.19), the TDOS then reads

$$\frac{\nu_{\mathrm{bulk}}(E)}{\nu_{\mathrm{1D}}} = \mathrm{Re} \sum_n \frac{(E-\Sigma(E))\,\mathrm{sgn}(E-\Sigma_R(E))}{\sqrt{(E-\Sigma(E))^2 - E_n^2}} \,, \tag{3.27}$$

where we restored all functional dependencies for clarity. The result (3.10) for the clean case is, of course, recovered in the limit $\Delta \to 0$. For $\Delta > 0$, the finite imaginary part of $\Sigma(E)$ in the denominator of (3.27) causes a broadening of the VHS, whereas the real part causes a shift of the peaks in energy. Equations (3.26) and (3.27) can be used to fit experimental data for the TDOS of MWNTs. Assuming that R is known, since Δ is the only fit parameter, the disorder strength can then be determined directly from the TDOS which would provide precious information on the level of disorder in the system.

For the numerical evaluation of Eq. (3.26), a cutoff for the summation over n has to be specified. Such a cutoff for the band index n is naturally given from the band structure. For instance, for armchair NTs, the number of subbands would be limited to $2N = 8\pi R/\sqrt{3}a$ [53]. For $R = 10$ nm, $N \approx 295$, and in the figures below, we use this cutoff such that $n \in [-295, 295]$. The results are, however, not very sensitive to the precise choice of this cutoff.

Figure 3.7 shows the strong *broadening of the VHS* due to the disorder. In addition, the position of the VHS is *shifted to smaller energies* with increasing Δ. This shift grows linearly with Δ, and the relative shift, compared to the position of the VHS in the clean system, can easily be up to 20%, depending on the disorder strength (note that the relative shift is independent of R). Since the radius of NTs is often determined from the relative positions of the VHS, this observation suggests that such interpretations need to be taken with some caution. The disorder-induced shift has to be taken into account to obtain correct results. With increasing order n of the VHS, the relative shift becomes, however, systematically smaller.

For sufficiently strong disorder, the peaks can even disappear completely above a certain energy threshold $E^*(\Delta)$. This is clear since the VHS, resulting from the opening of new subbands due to transverse momentum quantization, is destroyed

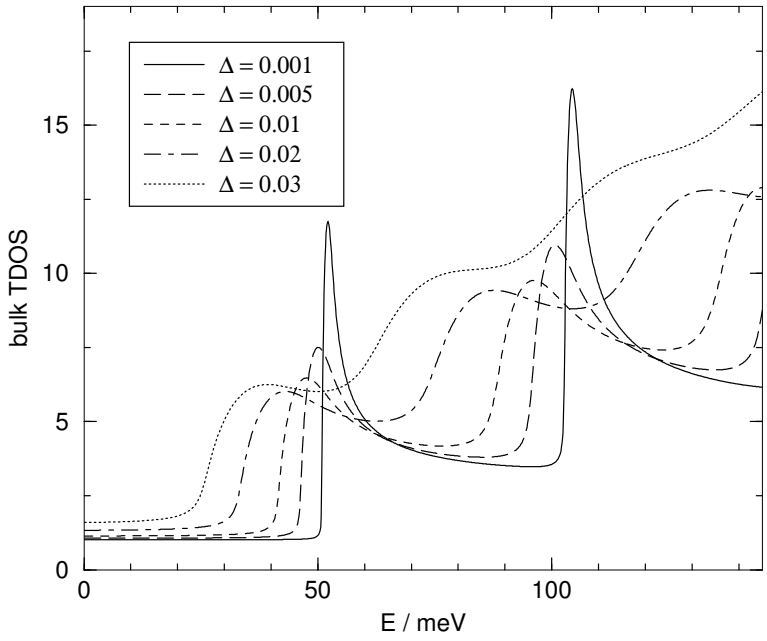

Figure 3.7: *Bulk TDOS of a disordered tube in the absence of a magnetic field for different values of the disorder strength Δ. The broadening of the VHS's with increasing Δ is clearly visible, as well as their shift towards smaller energies.*

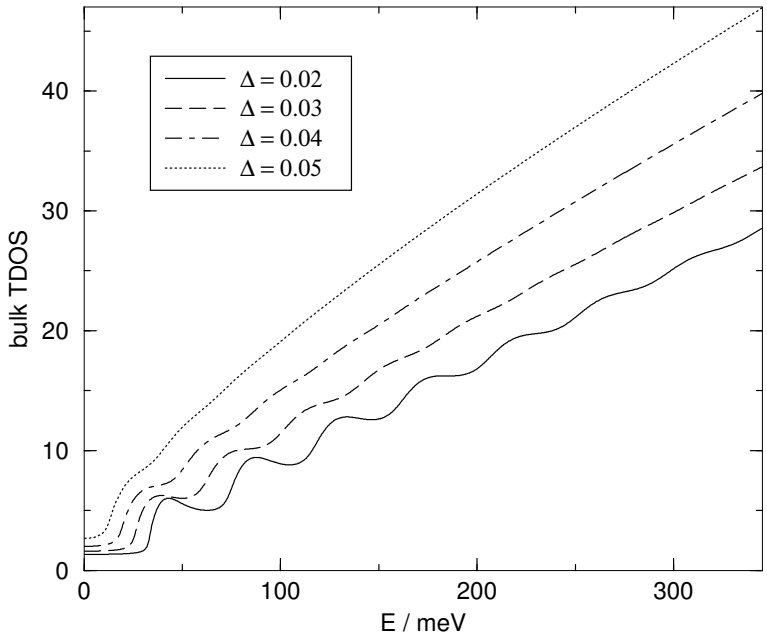

Figure 3.8: *Same setup as in Fig. 3.7 but for a wider energy range and stronger disorder. One clearly can trace the tendency of the VHS's to vanish with increasing Δ and E as well as the formation of a power law above a certain threshold (see also Fig. 3.10).*

once motion around the circumference becomes diffusive. This threshold energy decreases with increasing Δ (see Fig. 3.8).

In Fig. 3.9 we compare the TDOS and the corresponding mean free path. Using (3.19), the mean free path can be expressed in terms of the TDOS,

$$l(E) = \frac{R}{2\Delta} \frac{\nu_{1\mathrm{D}}}{\nu(E)} \ .$$

Importantly, the mean free path cannot be assumed to be simply a constant, but depends on energy. As one can estimate from Fig. 3.9, the VHS's are disappearing when $l(E) \leq R$. Hence, since many experiments on MWNTs suggest that l is of order of the circumference of the tube, the characteristic subband features of the TDOS should still be present, albeit considerably broadened and shifted (see Fig. 3.3).

In the region where no VHS's are present, i.e., above the threshold $E^*(\Delta)$, the TDOS behaves like a power law[5] with disorder-dependent exponent $\alpha = \alpha(\Delta) \approx 1 - 5\Delta \leq 1$,

$$\nu(E) \sim E^{\alpha} \ ,$$

which holds remarkably well for $\Delta \leq 0.05$, see Fig. 3.10. Note that energies here are absolute (not relative to E_F), and therefore this power law is unrelated to the findings of Refs. [48, 54, 55]. For $E < E^*(\Delta)$, there are deviations from the power law and the TDOS approaches a finite value for $E \to 0$. We also want to note that this power law has a different origin than the one found in the 2D case that rests upon the inclusion of crossed diagrams [43].

Next, we consider a fixed disorder strength Δ and vary the strength of a magnetic field applied parallel to the tube axis, see Fig. 3.11. Again, there is a doubling of the peaks corresponding to the VHS's, and the shift of the positions varies periodically with the magnetic field. The gap generated by the magnetic field survives even in the presence of disorder, but due to the disorder-dependent shift of the VHS's towards smaller energies, it gets partially filled with states and is therefore smaller compared to the clean case. However, magnetic field effects are essentially not (or only weakly) affected by disorder.

[5] In principle one would replace the sum by an integral, $\sum_{n=-N}^{N} \to R \int_{-\Lambda}^{\Lambda} d\epsilon$ with $\Lambda = ND$, to derive the power law analytically. This is, however, not so easily done since the functional dependencies in the resulting self-consistency equation for the self energy, that one has to solve, are quite nasty. Unfortunately, any helpful approximation destroys the desired result and hence, we cannot give an analytical expression for $\alpha(\Delta)$.

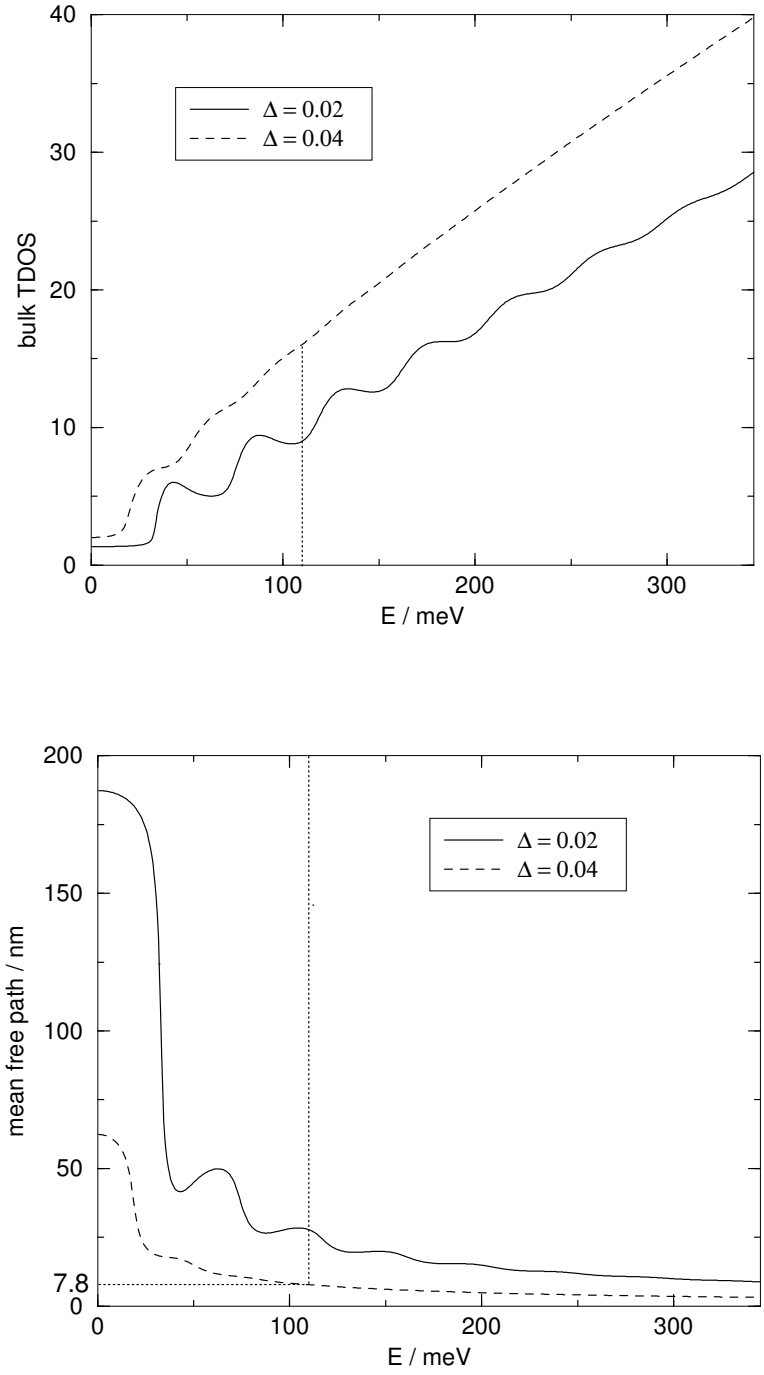

Figure 3.9: *Bulk TDOS (top) for two different disorder strengths and the corresponding mean free path $l(E)$ (bottom). Comparing both figures one can estimate the value of $l(E)$ where the VHS's disappear. One can see that approximately for $l(E) \leq R = 10$ nm, all van Hove peaks vanish as is indicated by the dotted line, which is a guide to the eye only, and for $\Delta = 0.04$ leads to $l(E) \approx 7.8$ nm.*

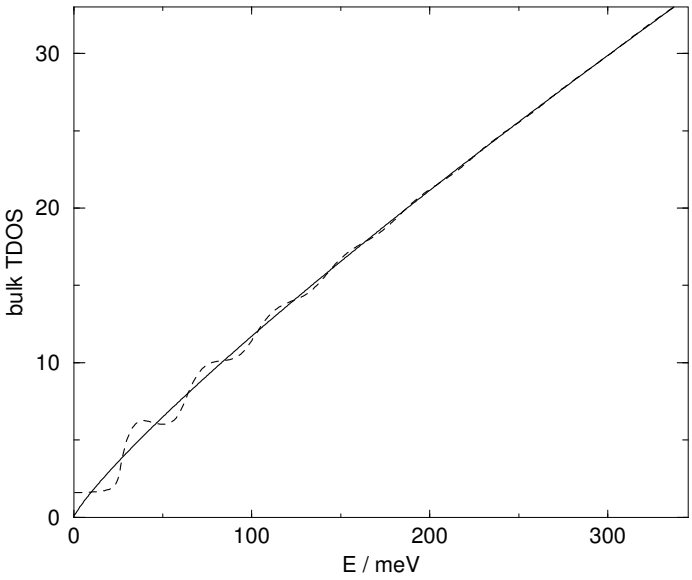

Figure 3.10: *Bulk TDOS (dashed line) for* $\Delta = 0.03$ *and the corresponding power law fit (solid line) according to* $\nu \sim E^{\alpha}$*, with* $\alpha \approx 0.85$*. The energy threshold, above which the power law is valid, can roughly be estimated to be* $E^* \approx 230$ *meV. Below, there are deviations from the power law behavior that increase in the limit* $E \to 0$*. Both* α *and* E^**, of course, depend on* Δ*.*

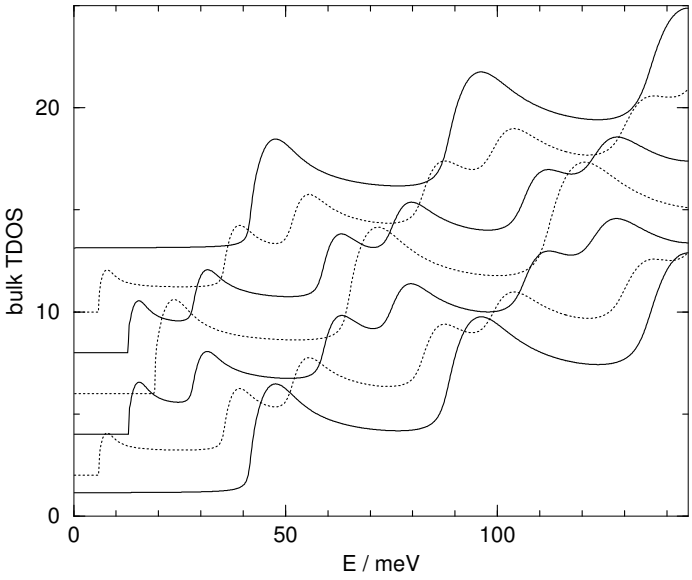

Figure 3.11: *Bulk TDOS for* $\Delta = 0.01$ *and different values of the magnetic field* B*. The curves corresponding to different* B *are shifted vertically by the same amount for better visibility. The lowest curve corresponds to* $B = 0$*, and* B *is increased in steps of* $\Delta B = 2.2$ *T. Notice the opening and closing of a gap with variation of* B*, and the periodicity in* B *with period* $B_0 = 13.2$ *T for* $R = 10$ *nm.*

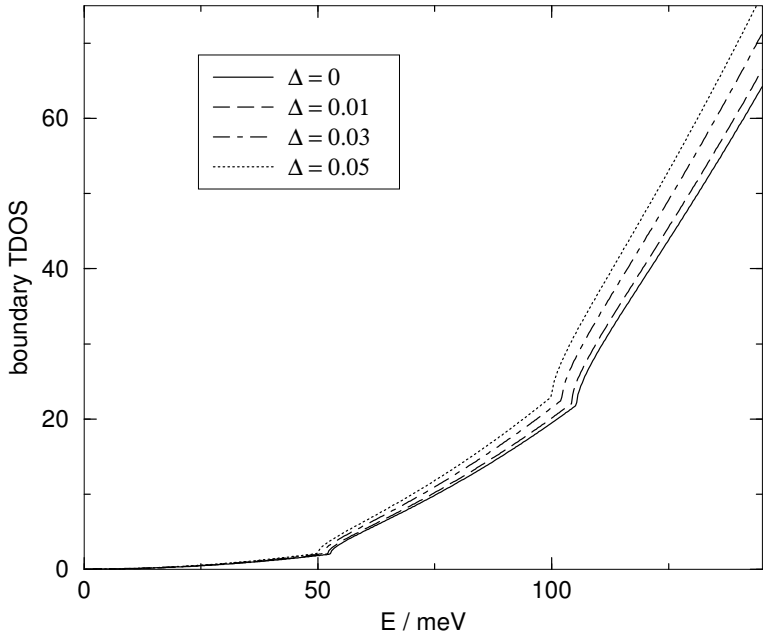

Figure 3.12: *Boundary TDOS for different values of the disorder strength Δ in the absence of a magnetic field. Disorder causes an increase of the TDOS that grows with increasing Δ, as well as a shift of the van Hove non-analyticities to smaller energies. For all curves in this plot, $x/R = 10^{-3}$.*

3.5.2 Boundary limit

Finally, we briefly turn to the boundary limit, $x \to 0$. Expanding the exponential function in (3.25) up to second order in x/R we have

$$\begin{aligned} \Sigma &= -4N\Delta\frac{x}{R}(E-\Sigma) \\ &\quad -2i\Delta\left(\frac{x}{R}\right)^2\sum_n \frac{E-\Sigma}{D}\,\mathrm{sgn}(E-\Sigma_R)\sqrt{(E-\Sigma)^2-E_n^2}\,, \end{aligned} \tag{3.28}$$

leading to the boundary TDOS (with restored functional dependencies)

$$\begin{aligned} \frac{\nu_{\mathrm{end}}(E,x)}{\nu_{\mathrm{1D}}} &= \frac{2}{1-4N\Delta x/R}\left(\frac{x}{R}\right)^2 \\ &\quad \times\ \mathrm{Re}\sum_n \frac{E-\Sigma(E,x)}{D^2}\,\mathrm{sgn}(E-\Sigma_R(E,x))\sqrt{(E-\Sigma(E,x))^2-E_n^2}\,. \end{aligned} \tag{3.29}$$

These relations are appropriate as long as $x/R \ll 1/4N\Delta$ and obviously, $\Delta \to 0$ gives the correct limit (3.11). Compared to the clean case, the disordered boundary TDOS is increased and the increase grows with larger disorder strength (see Fig. 3.12). The positions of the van Hove non-analyticities at the opening of new subbands are shifted to smaller energies while their form is not significantly changed

by the disorder but approximately retains a square-root energy dependence above the threshold. Compared to the bulk case, the shift in the boundary case is much smaller.

The quadratic behavior of ν_{end} in the regime $0 < E < D$ remains unchanged by the disorder as well as the cubic behavior on the larger scale $0 \ll E \ll ND$. The presence of disorder basically leads to a prefactor that enhances the boundary TDOS. In the presence of a magnetic field one observes essentially the same as in the bulk case, i.e., a doubling of the non-analyticities and the periodic opening and closing of a gap.

3.6 Comparison with experiments

It is difficult to quantitatively compare our results with currently available experimental data. But one can check for qualitative agreement. The reported differential tunneling conductance in [48] (see Fig. 3.3) exhibits broadened (and possibly shifted) VHS's. The radius estimated from the distance between the two first-order subbands deviates from the directly measured one by $\approx 10\%$. This deviation could result from the disorder-dependent shift as predicted by our theory. Therefore, both findings are consistent with our results. However, to surely attribute these effects to disorder one would need more data exhibiting stronger deviations in order to rule out measurement uncertainties.

Hence, it would be necessary to measure the differential conductance up to higher energies, i.e., higher orders of the VHS. Further, specific disorder variation, e.g., by fast ion bombarding, would be helpful to check the predictions made by our model. Especially, it would be interesting whether one can see the predicted power law for large disorder strength.

Periodically shifted conductance peaks in a parallel magnetic field were observed, e.g., in [54]. Although a detailed comparison with our results has not yet been done, a systematic investigation focusing on only the lowest VHS could easily reveal the doubling as well as the periodicity, depending on the tube radius.

STS measurements in the boundary limit were carried out for both SWNTs [28] and MWNTs [56]. Sharp resonances in the tunneling conductance were observed at the last few nm at the end of the NTs. However, these resonances were identified as localized states corresponding to a particular cap structure, i.e., a specific arrangement of pentagons (topological defects) at the end.

Several lattice spacings away from the tube end, where our model is supposed to be accurate, the situation is different. There, the subband edges fade out and no VHS's (divergencies) were found in the tunneling spectrum [27, 28, 56], as is hinted at by our calculation. However, to unambiguously observe the predicted square-root non-analyticities seems to be difficult and, to the best of our knowledge, has not yet been done. But again, our results are in qualitative agreement with the experiments.

3.7 Conclusions

In this chapter, we have calculated the TDOS of disordered multichannel quantum wires, with special emphasis on MWNTs. In the present theory, electron-electron interactions are supposed to be screened off by a metallic substrate or a close-by gate. Focusing on potential scattering disorder, within a non-crossing approximation, a self-consistent non-perturbative summation of all diagrams for the self energy yields an analytical result for the disorder-broadened VHS's in such a system. For given radius of the MWNT, our result involves only one parameter (the disorder strength Δ), which should allow for a detailed comparison to STS experiments on MWNTs. We also stress that it is in general not possible to define an energy-independent mean free path for all energies.

Remarkably, the standard Born approximation breaks down in the vicinity of a VHS, and one has to include higher-order diagrams for the self energy. We have demonstrated that this problem can be approximately yet accurately solved by combining a non-crossing approximation with an iterative self-consistent summation of all remaining diagrams. The theory can then be applied to the energy dependence of the TDOS, and reveals remarkable differences in the bulk and boundary limits. These effects could be observed experimentally using available technology.

In the bulk limit, we predict broadened VHS's that are shifted to smaller energies compared to the clean case. For high energies (above a certain threshold), the TDOS behaves as a power law in energy, with a disorder-dependent exponent. In the boundary limit, VHS's appear only as non-analyticities at the opening of new subbands, with a square-root energy dependence of the TDOS above the threshold. This behavior is basically unchanged in the disordered case, but we observed a shift of the non-analyticities to smaller energies and a disorder-dependent increase of the TDOS.

Chapter 4

Luttinger liquid theory

In this chapter we first motivate the Luttinger liquid picture by describing the Fermi liquid theory and its breakdown in 1D. We argue that bosonization is a powerful tool for describing interacting 1D metals and therefore explain its basic properties for a spinless system. Afterwards, we generalize the method to the more complicated case of a SWNT.

4.1 Motivation

The fundament of the theoretical description of metals in more than 1D is the Fermi liquid theory (FLT) which accounts for the behavior of the conduction electrons in conventional metallic systems. The central assumption of FLT is that the low-energy excited states of the interacting electron gas can be classified in the same way as a reference non-interacting electron gas which leads to the central concept of quasi-particles [57]. Conceptually, a quasi-particle excitation is generated from free electrons by adiabatically switching on the electron-electron interaction[1] after preparing a system state with, say, one electron in an excited state above the ground state Fermi sea. The quasi-particles are in one-to-one correspondence with the bare electrons (holes) and, specifically, obey Fermi-Dirac statistics and carry the same quantum numbers as ordinary electrons (holes). Thus, the free Fermi gas is the solvable model on which FLT is built.

The electron-electron interaction has three main effects: (i) it renormalizes the dynamical properties of the quasi-particles such as their effective mass; (ii) it gives them a finite lifetime diverging, however, as $\tau \sim (E - E_F)^{-2}$ as the Fermi surface is approached; (iii) it introduces new collective modes. The existence of quasi-particles formally shows up through a finite jump of the momentum distribution function at the Fermi surface, corresponding to a finite residue of the quasi-particle pole in the Greens function. FLT is approximate but not perturbative and well understood.

[1] This should, but need not, work when interactions are repulsive, not too strong, and at low energies.

It becomes an asymptotically exact solution of a given many-body problem for low energies and small wavevectors ($E \to E_F, |\vec{k}| \to k_F, T \to 0$).

FLT is equivalent to the assumption that the Greens function

$$G(k,\omega) = \frac{1}{G_0^{-1} - \Sigma(k,\omega)} \ ,$$

with the self energy Σ containing all the many-body effects, possesses a single pole of residue z_k close to the Fermi surface (z_k is also called quasi-particle weight and gives the magnitude of the jump of the momentum distribution function of the bare particles at the Fermi surface). The breakdown of FLT in 1D is signaled by the appearance of multiple poles or vanishing z_k.[2] Accordingly, in 1D metals there are no fermionic quasi-particles, and it turns out that only particle-hole excitations determine the dynamics of an excited state. Unlike in 3D, the corresponding excitation spectrum in 1D has a wide region of forbidden states at low energy and finite momentum, and shrinks to a one-parameter form $\omega \approx vq$ in the limit $\omega, q \to 0$. This implies that the particle-hole excitations (respectively collective charge and spin fluctuations constructed by appropriate linear combinations) form stable, particle-like elementary excitations of the system which are described by an effective harmonic oscillator Hamiltonian and obey bosonic commutation rules. These charge and spin fluctuations are also dispersing with different velocities (in the interacting case) which means that an incoming electron seems to fall apart into separate elementary charge and spin excitations which then spatially separate with time (spin-charge separation). The correlations between the excitations are anomalous and show up as interaction dependent non-universal power laws in many physical quantities where those of ordinary metals are characterized by universal (interaction independent) powers. The reasons for these peculiar properties are found in the very special Fermi surface topology of 1D fermions, i.e., in a 1D chain, one has simply two Fermi points $\pm k_F$.

All these properties mentioned above are generic for 1D fermion systems and particular prominent in a 1D model of interacting fermions with strictly linear dispersion relation proposed by Tomonaga [58] and Luttinger [59] and solved exactly by Mattis and Lieb [60]. The resulting non-Fermi liquid state is commonly called Luttinger liquid (LL), a name coined by Haldane [61]. The LL is best understood as an effective theory for the low-energy excitations of a 1D metal (with gapless charge and spin excitations) or, in other words, for interacting 1D electron systems (provided they remain gapless). The elementary bosonic modes, together with operators changing the particle number in the system, can be used to construct the

[2] Since in 1D for a single branch with linear dispersion, momentum conservation automatically implies energy conservation, the phase space for an electron to relax by creating an electron-hole excitation is less constrained compared to, e.g., 3D. This leads to a divergent rate for such scattering processes which drives the electron spectral weight to zero, even for weak interactions. Accordingly, FLT breaks down in such systems for arbitrarily weak interactions.

Fermi liquid	Luttinger liquid
• describes fermions in 3D • elementary excitations are fermionic quasi-particles • correlation functions for interacting and non-interacting system are qualitatively the same • energy independent TDOS	• describes fermions in 1D • elementary excitations are of bosonic nature → spin-charge separation • correlation functions are power laws with (non-universal) interaction-dependent exponents • TDOS strongly suppressed for $E \to E_F$

Table 4.1: *Comparison of some important Fermi and Luttinger liquid features.*

entire low-energy sector of the Hilbert space. Finally, bosonization allows, through an operator identity representing a fermion operator in terms of charge and spin bosons, to calculate all correlation functions of the LL, so that one has direct access to all physical properties of interest. When the electron dispersion is approximated by a linear law, the resulting model can be solved exactly in the presence of electron-electron interactions which enters the theory as a single dimensionless parameter.

To summarize, a LL is characterized by three important properties. First, its elementary excitations are not fermionic quasi-particles but bosonic collective modes. The absence of quasi-particles is visible explicitly in the single-particle spectral function. Second, fermion operators acquire anomalous dimensions implying that all correlation functions of a LL exhibit power-law behavior with exponents depending on the interaction strength and are therefore non-universal. Hence, in order to prove LL theory, it is not sufficient that one or more particular experiments show power-law correlations. In addition, the power-law exponents they measure must yield consistent values for the interaction strength. The third point is the spin-charge separation explained above which is due to the Hamiltonian describing the system being a sum of a charge and spin part, each describing harmonic oscillators. Both anomalous dimensions and spin-charge separation are sufficient conditions for the breakdown of a quasi-particle picture for interacting 1D electron systems. Some of the main differences between FLT and LL theory are summarized in Table 4.1.

The LL concept provides a paradigm for non-Fermi liquid physics and may have some relevance also for higher-dimensional systems, e.g., in relation to high-temperature superconductivity. The range of validity of the LL model is usually set by $E \ll D$, where D is the electronic band width and E is the relevant energy scale, namely either the thermal scale $k_B T$ or the applied voltage eV. Most measurements, in fact, only probe correlations on energy scales small compared to the Fermi energy so that indeed only the low-energy sector of a given model is of importance. Moreover, only at low energies we can hope to excite only a few degrees of freedom, for which a meaningful comparison to theoretical predictions can be attempted. The

to-date perhaps cleanest experimental observations of LL behavior were established in transport experiments for SWNTs [62, 63].

4.2 Bosonization

Now, we want to substantiate the concepts discussed in the previous section. For simplicity, we here only consider the spinless case and later generalize the formulas we need. Again, we set $\hbar = 1$.

Bosonization of a fermionic system is possible in 1D since the low-energy excitations can be completely described in terms of collective charge and spin density oscillations. In the model studied by Tomonaga and Luttinger, a special dispersion relation was assumed, where one linearizes around the two Fermi points $\pm k_F$ present in 1D, $E(k) = v_F(\pm k - k_F)$. At sufficiently low energy scales, such a procedure should clearly be possible. Accordingly, the bosonization approach is usually appropriate for low temperatures, where only excitations near the Fermi surface are relevant. In fact, in SWNTs, as already mentioned, the dispersion relation is highly linear anyways. Thus, we have to consider three types of particles. Right-movers (R) have momenta $k \approx k_F$ and velocity v_F while left-movers (L) have momenta $k \approx -k_F$ and velocity $-v_F$. The third type of particles are inert electrons deep in the Fermi sea which play no role in the low energy physics (see Fig. 4.1). To avoid (various) mathematical subtleties due to the infinite Dirac sea, we always assume a finite band cutoff.

One can now equivalently express the non-interacting problem in terms of collective plasmon (density wave) excitations. Technically, in the "bosonization" language [64], for the simplest case of a spinless single-channel system, these bosonic excitations can be expressed in terms of a (bosonic) displacement field $\theta(x)$ and its canonical momentum $\Pi(x)$ (i.e., $[\theta(x), \Pi(x')]_- = i\delta(x - x')$),

$$H = \frac{v_F}{2} \int dx \left\{ \Pi^2(x) + [\partial_x \theta(x)]^2 \right\} ,$$

such that the density fluctuations are $\rho(x) = \partial_x \theta(x)/\sqrt{\pi}$. Electron-electron interactions then describe a bilinear coupling of these density fluctuations,

$$H_U = \frac{1}{2\pi} \int dx\, dx'\, \partial_x \theta(x) U(x - x') \partial_{x'} \theta(x') ,$$

and therefore the full interacting problem can be written as a free theory in the displacement field,

$$H_{\mathrm{LL}} = \frac{v_F}{2} \int dx \left\{ \Pi^2(x) + \frac{1}{g^2} [\partial_x \theta(x)]^2 \right\} . \tag{4.1}$$

This is the so-called Luttinger liquid Hamiltonian. In the long-wavelength limit, one can approximate the Fourier transform $\widetilde{U}(k)$ of the 1D interaction potential by

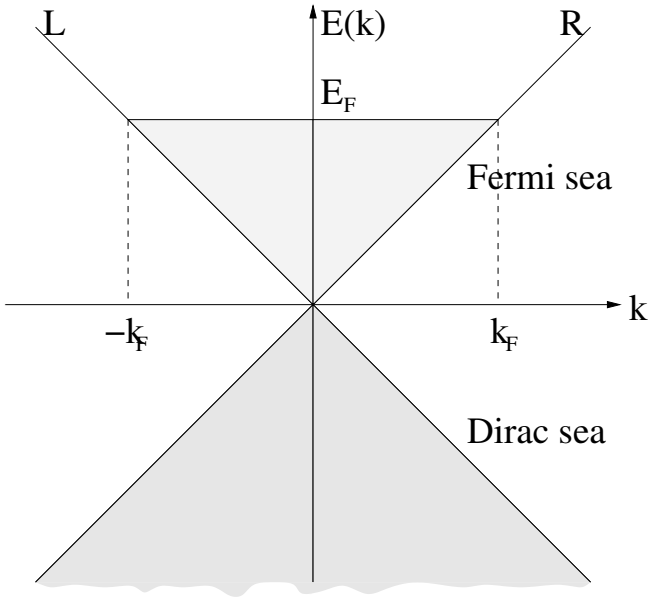

Figure 4.1: *Dispersion relation of the Tomonaga-Luttinger model with infinite Dirac sea and the Fermi sea filled up to the Fermi energy E_F. One can also see the two branches of the right- and left-movers.*

a constant $U_0 = \widetilde{U}(0) - \widetilde{U}(2k_F)$,[3] and the dimensionless interaction parameter g in Eq. (4.1) is given then by

$$g = \frac{1}{\sqrt{1 + U_0/\pi v_F}} \,.$$

We have $0 < g \leq 1$ for repulsive interactions, with small g meaning strong interactions, while $g > 1$ for attractive interactions. The limit $g = 1$ describes the non-interacting Fermi gas (*not* a Fermi liquid), and the limit $g \to 0$ leads to a classical Wigner crystal. Since the model (4.1) is equivalent to a set of harmonic oscillators[4] it can be solved exactly. This is the great advantage of the Bose representation, that also the interacting system is described by a free theory where the only effect of the interaction is to renormalize the Fermi velocity, $v_F \to v_F/g$. In contrast, in the Fermi representation the interaction leads to quartic terms in the Fermi operators which makes it in general quite difficult to handle.

The Holy Grail of bosonization is that the (fermionic) creation operator for a right- or left-moving electron ($r = R/L = \pm$) can equivalently be expressed in terms of the bosonic phase fields $\theta(x)$ and $\phi(x) = \int^x dx' \, \Pi(x')$ by means of the

[3]Equivalently one can assume a point interaction, $U(x - x') = U_0 \delta(x - x')$, which directly gives $\tilde{U}(k) = U_0$. Of course, this is a mathematical trick since a true δ-function would have no effect.

[4]Using $\Pi(x) = \partial_x \phi(x)$ and the commutation relations (4.3) for θ and ϕ it is easy to obtain the equations of motion from (4.1), $\partial_t^2 \theta = v^2 \partial_x^2 \theta$ with $v = v_F/g$ (and similarly for ϕ). Therefore, $H_{\rm LL}$ describes a wave propagating at velocity v.

"bosonization identity" (for details see, e.g., [64]),

$$\psi_r(x) \simeq \frac{1}{\sqrt{2\pi a}} \exp\left[irk_F x + i\sqrt{\pi}\left\{\phi(x) + r\theta(x)\right\}\right] , \tag{4.2}$$

where $a \approx 1/k_F$ is a lattice constant.[5] The phase fields itself fulfill the algebra

$$\begin{aligned} [\theta(x), \theta(x')]_- &= [\phi(x), \phi(x')]_- = 0 , \\ [\theta(x), \phi(x')]_- &= \frac{i}{2}\mathrm{sgn}(x - x') . \end{aligned} \tag{4.3}$$

4.3 Luttinger liquid theory for single-wall nanotubes

The generic band structure of a metallic SWNT is shown in Fig. 4.2. Up to energy scales $E < D \approx 1$ eV, the dispersion relation around the Fermi points is, to a very good approximation, linear. If the x-axis is taken along the tube direction and the circumferential variable is $0 < y < 2\pi R$, quantization of transverse motion then allows for a contribution $\propto \exp[iny/R]$ to the wavefunction. However, excitation of angular momentum states other than $n = 0$ costs a huge energy of order D. In an effective low-energy theory, assuming that the SWNT is not excessively doped, we may thus omit all transport bands except $n = 0$. Evidently, the SWNT forms a 1D quantum wire with only two transport bands intersecting the Fermi energy. In contrast to conventional systems like semiconductor quantum wires, LL effects in SWNTs are not restricted to the meV range but may even be seen at room temperature since the approximation of linearizing the dispersion relation is here provided by nature in an essentially exact way.

In the same way as done in Sec. 2.2 one can expand the electron operator for spin $\sigma = \pm$ in terms of the Bloch functions living on the two sublattices, see Eq. (2.1), but with the difference that due to the restriction $n = 0$ this expansion now introduces slowly varying 1D fermion operators $\psi_{p\alpha\sigma}$ that depend only on the x-coordinate,

$$\Psi_\sigma(x, y) = \sum_{p\alpha} \varphi_{p\alpha}(x, y)\psi_{p\alpha\sigma}(x) .$$

Neglecting Coulomb interactions for the moment, the 2D massless Dirac Hamiltonian (2.2) describing the effective low-energy theory for graphene reduces to

$$H = -v_F \sum_{p\alpha\sigma} p \int dx\, \psi^\dagger_{p\alpha\sigma}(x)\partial_x \psi_{-p\alpha\sigma}(x) .$$

[5] To be more precise, one would have to add "Klein factors" in (4.2). These are non-Hermitian operators that increase the total particle number in one of the branches by one and are necessary since the boson fields all conserve the total particle number. They also ensure proper anticommutation between right- and left-going operators. In the thermodynamic limit $L \to \infty$, where L is the system length, this is, however, of minor importance since a change in the particle number represents a shift of k_F by a quantity of order $1/L$.

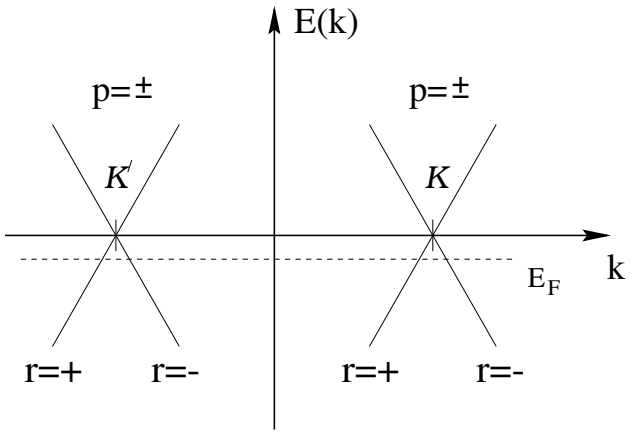

Figure 4.2: *Schematic band structure of a metallic SWNT. A right- and left-moving branch ($r = \pm$) is found near each of the two Fermi points $k = \alpha k_F$ with $\alpha = \pm$, corresponding to K and K', respectively. Right- and left-movers arise as linear combinations of the sublattices $p = \pm$. The Fermi energy (dashed line) is shifted away from neutrality by doping and/or external gates.*

Switching from sublattice description ($p = \pm$) to the right-/left-movers ($r = \pm$), which are linear combinations of the sublattice states,

$$\psi_{p\alpha\sigma} = \sum_r U_{pr}\psi_{r\alpha\sigma} \quad \text{with} \quad U_{pr} = \frac{1}{\sqrt{2}}\begin{pmatrix} 1 & i \\ 1 & -i \end{pmatrix},$$

implies two copies of massless 1D Dirac Hamiltonians for each spin direction,[6]

$$H = -iv_F \sum_{r\alpha\sigma} r \int dx\, \psi^\dagger_{r\alpha\sigma}(x)\partial_x\psi_{r\alpha\sigma}(x)\ . \tag{4.4}$$

In this representation, a bosonization formula generalizing Eq. (4.2) applies [66], now with four bosonic phase fields $\theta_a(x)$ and their canonical momenta $\Pi_a(x) = \partial_x\phi_a(x)$, with flavor index $a = c+, c-, s+, s-$,

$$\begin{aligned}\psi_{r\alpha\sigma} \;&\simeq\; \frac{1}{\sqrt{2\pi a}}\exp\Big[ik_F\alpha x + i\frac{\sqrt{\pi}}{2}(\phi_{c+} + r\theta_{c+} \\ &+\; \alpha\phi_{c-} + r\alpha\theta_{c-} + \sigma\phi_{s+} + r\sigma\theta_{s+} + \alpha\sigma\phi_{s-} + r\alpha\sigma\theta_{s-})\Big]\ .\end{aligned}$$

The four channels correspond to the total (+) and relative (−) charge (c) and spin (s) channel, respectively. They are obtained from combining charge and spin degrees

[6]Therefore, a perfectly contacted and clean SWNT has four conducting channels and is hence expected to have the quantized conductance $G = 4e^2/h$. Due to the difficulty of fabricating sufficiently good contacts this value has not been experimentally observed so far. However, in recent experiments conductance values very close to this theoretical prediction were obtained [65].

of freedom as well as symmetric and antisymmetric linear combinations of the two Fermi points. The algebra now reads

$$[\theta_a(x), \phi_{a'}(x')]_- = \frac{i}{2}\delta_{aa'}\mathrm{sgn}(x-x') \ ,$$

while all other commutators vanish.

When including the electron-electron interaction and at sufficiently high temperatures (above the gap temperature of $T \approx 0.1$ mK) where it is justified to neglect non-linearities associated with the forward and backward scattering coupling constants [67], the bosonized expression of the Hamiltonian reads,

$$H = \frac{v_F}{2}\sum_a \int dx \left\{ \Pi_a^2 + \frac{1}{g_a^2}(\partial_x \theta_a)^2 \right\} \ ,$$

and hence, SWNTs constitute a realization of a LL with an additional flavor index.[7] The dimensionless interaction strength for the different channels is

$$g_{c+} = \left\{ 1 + \frac{8e^2}{\pi\kappa\hbar v_F} \ln\left(\frac{L}{2\pi R}\right) \right\}^{-1/2} \leq 1 \ ,$$

κ is the dielectric constant, while for all other channels, $g_{a\neq c+} = 1$. Since the dependence on L and R is only logarithmically, basically all SWNTs studied at the moment are characterized by typically $g_{c+} = 0.2$ to 0.3 [62, 63]. Hence, a SWNT constitutes a strongly correlated system and one can expect that the electronic properties thus differ from what is expected by FLT. The plasmon velocities of the four modes are $v_a = v_F/g_a$, and hence the charged ($c+$) mode propagates with significantly higher velocity than the three neutral modes which are unaffected by the interaction.

A power-law suppression $\nu(\epsilon) \sim \epsilon^\alpha$ of the TDOS in the limit $\epsilon \to 0$ is expected for a strongly correlated electron gas described by LL theory, where the energy ϵ is measured relative to the Fermi level [68]. When we assume f transport channels, the exponent α governing the scaling is depending on the geometry, i.e., whether one tunnels into the bulk or into the end of the system. Setting $\alpha = \eta - 1$ one finds,

$$\begin{aligned} \eta_{\mathrm{end}} &= \frac{1}{f}\left(\frac{1}{g} + f - 1\right) \ , \\ \eta_{\mathrm{bulk}} &= \frac{1}{f}\left\{\frac{1}{2}\left(g + \frac{1}{g}\right) + f - 1\right\} \ , \end{aligned} \tag{4.5}$$

where g is the interaction constant in the charged mode. Hence, for a SWNT we would have

$$\alpha_{\mathrm{end}} = \frac{1}{4}\left(\frac{1}{g_{c+}} - 1\right) \ . \tag{4.6}$$

[7] For NTs doped away from half-filling, umklapp-processes suffer a momentum mismatch at the Fermi surface, thereby becoming ineffective. The validity of the Luttinger model is then only limited by the exponentially small backscattering scale [66].

Similar anomalies have recently been observed by Bockrath *et al.* for SWNTs [63]. Their measurement and analysis provide the first demonstration for LL behavior in carbon NTs due to long-range Coulomb interactions.[8] The ratio of the exponents $\alpha_{\rm end}/\alpha_{\rm bulk} > 2$ is interaction dependent and reflects the fact that for tunneling into the end of the system there is only one direction for the electron to escape while for tunneling into the bulk there are two. Further, it is clear that the exponents add up for a certain tunneling geometry, e.g., when the tunneling is from the end of one NT into the end of another NT then the TDOS will be governed by $\alpha_{\rm end-end} = 2\alpha_{\rm end}$.

As we will see in the next chapter, electron-electron interactions strongly modify the low-energy excitations in a quantum wire leading to striking predictions for the transport in the presence of one or several impurities.

[8] Also for MWNTs one observes a strong suppression of tunneling into the tube but with different origin than for SWNTs. In recent experiments on intrinsically (hole-) doped MWNTs (where $E_F \approx 0.5$ eV), Bachtold *et al.* have shown that the tunneling conductance vanishes as a power law in temperature and in bias voltage [54]. A proper theoretical explanation for this behavior was given in [55]. It was shown that this zero-bias anomaly in the TDOS of doped MWNTs can be explained in terms of electron-electron interactions in conjunction with diffusive motion, which effectively leads to a very efficient Coulomb blockade for tunneling into the MWNT. Due to the strong interactions, this power law can be thought of as a non-perturbative Al'tshuler-Aronov anomaly. It was also shown that the presence of a boundary implies a universal doubling of the boundary exponent, $\alpha_{\rm end} = 2\alpha_{\rm bulk}$, which holds only in the diffusive limit.

Chapter 5

Resonant tunneling and Kondo effect

After discussing basic properties of quantum dots, especially the phenomenon of Coulomb blockade, we turn to the general problem of tunneling through such a device. In this context we briefly describe the Kondo effect as well as the relevant tunneling mechanisms. Subsequent to these introductory remarks we review the theory of resonant tunneling through a double-barrier structure (forming a quantum dot) in a LL. Due to exciting recent experimental results this problem attracted renewed attention by theorists and, due to partly conflicting results, led to a controversial discussion in the literature. We discuss the results for both spinless and spinful fermions thereby focusing, for simplicity, on symmetric barriers only.

5.1 Introduction

5.1.1 Quantum dots - artificial atoms

Quantum dots (QDots) are nanometer-scale structures, where one confines a few to a few thousand electrons, e.g., in 2D electron gases in semiconductor heterostructures by means of suitable gates or in NTs by strong bends acting as local barriers. Due to the confinement, QDots have discrete energy levels and in many respects they are like artificial atoms. The great advantage of QDots compared to real atoms is, however, the ease with which its properties can be tuned. Especially the number of electrons in a QDot can be precisely controlled and varied during an experiment. The general setup is depicted in Fig. 5.1.

In contrast to real atoms, one can study transport through a QDot via attached leads. For temperatures and bias voltages that are low compared to the charging energy $E_c = e^2/2C$, i.e., the energy required to add an electron to the island (C is the capacitance of the dot), electric transport through the device is blocked due to

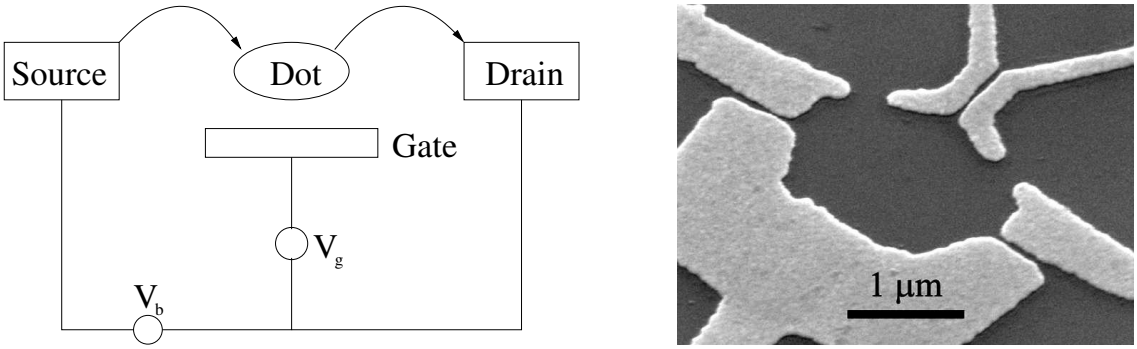

Figure 5.1: *General setup of a quantum dot (left). The number of electrons sitting on the dot can be controlled by adjusting both the gate voltage V_g and the bias voltage V_b. The right picture shows a semiconductor quantum dot where the confinement of the electrons in a 2D electron gas is provided by suitable gates on top of the sample.*

quantized charge tunneling (Coulomb blockade) [69]. A voltage V_g applied to the back gate (capacitively, C_g, coupled to the QDot) can then have a pronounced effect on the device conductance since transport through the dot is restored when V_g is tuned to special values, where N and $N+1$ electron-states are degenerate and an electron can be added with no cost of energy ("charge degeneracy"). To illustrate this we consider an isolated QDot, with a certain charge $-Ne$, coupled by tunneling barriers to external leads. The preferred charge due to V_g is then $C_g V_g$ and hence, $E_c = (Ne - C_g V_g)^2/2C$, see Fig. 5.2.

Therefore, upon changing the gate voltage, a gap in the differential conductance opens and closes in a periodic manner which gives rise to a pattern of periodic conductance peaks at zero bias, $V_b = 0$ (see Fig. 5.3). These peaks occur when the energy change due to the tunneling of one electron onto or out of the QDot equals the Fermi energy of the leads. Thus, both bias and gate voltage can be used to modulate the conductance leading to diamond-shaped regions where the conductance is suppressed (Coulomb diamonds, see Fig. 5.4). Within each diamond, the number of electrons on the QDot is fixed, and new electrons are added one by one to the island upon increasing V_g (single electron tunneling).

Applications of QDots include, e.g., single electron transistors that control currents at the level of a single electron and have been proposed as a future alternative to conventional Si electronic components. However, most of them operate at cryogenic temperatures, which strongly limits their practical application. A device which operates at room temperature can be built of a carbon NT [71]. Generally, a single electron transistor consists of a conducting island connected by tunnel barriers to two metallic leads. At low enough energies when Coulomb blockade becomes operative, conduction (at a single electron level) can be controlled by tuning the voltage on a close-by gate, rendering this three-terminal device a transistor.

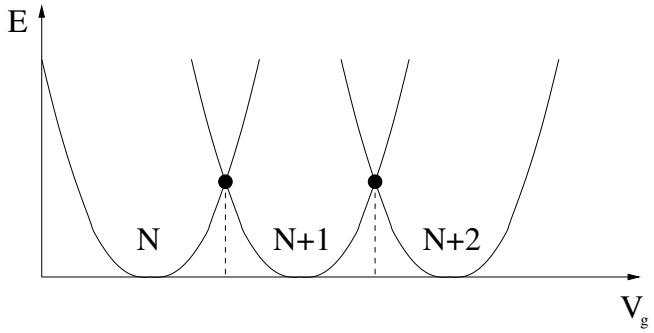

Figure 5.2: *Charging energy as a function of gate voltage. The number of electrons N on the island is indicated as well as the transitions (charge degeneracy points) at gate voltages corresponding to half-integer N.*

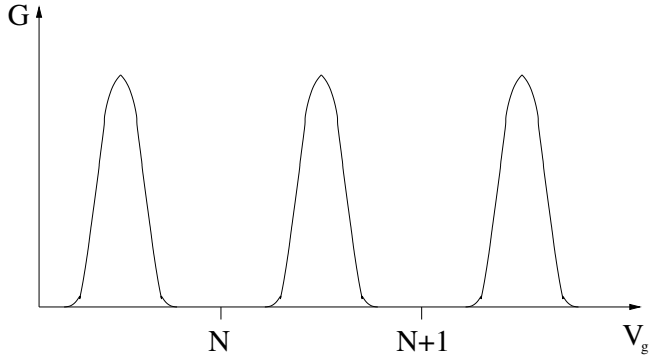

Figure 5.3: *Conductance as a function of gate voltage (i.e. number of electrons on the island). Peaks occur at half-integer values of N.*

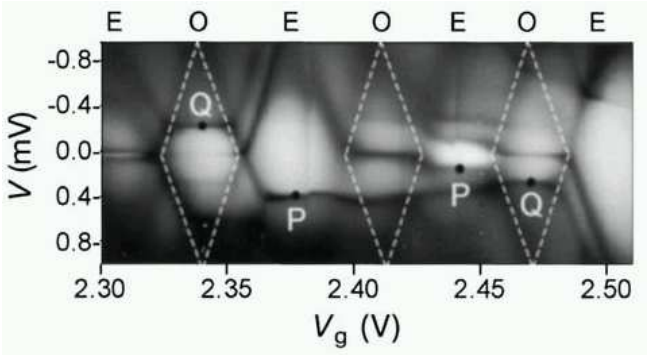

Figure 5.4: *Greyscale plot of the differential conductance dI/dV through a SWNT QDot with Au source and drain contacts, and a substrate gate contact ($T = 75$ mK). Dark/light areas correspond to low/high conductance while E,O indicate an even or odd number of electrons on the dot. The dashed lines outline the odd Coulomb diamonds and are a guide to the eye only. Horizontal features such as those labelled P and Q could suggest higher-order processes involving two levels. (From [70].)*

5.1.2 Kondo effect

Arising in the prototypical case from the interaction between the magnetic moment of a localized impurity and delocalized electrons in a metallic host, the Kondo effect[1] has been used to explain the enhanced low-temperature scattering from magnetic impurities in metals [72], but also occurs in transport through QDots.

The simplest model of a magnetic impurity was introduced by Anderson in 1961 and has only one electron level (also for small QDots it has come to be the "canonical model"). The Hamiltonian, including the coupling to the leads, is

$$H_{\mathrm{dot}} = \epsilon_0 \sum_s d_s^\dagger d_s + E_c d_\uparrow^\dagger d_\uparrow d_\downarrow^\dagger d_\downarrow + t\left[\left(\psi_{1s}^\dagger + \psi_{2s}^\dagger\right) d_s + \mathrm{h.c.}\right] ,$$

where $\psi_{is}^\dagger$ creates an electron with spin s in lead i while $d_s^\dagger$ creates an electron with spin s on the dot. The energy level of the dot is denoted by ϵ_0 (we assume $\epsilon_0 = -E_c/2$ and $k_B T \ll E_c$) and the tunneling matrix element between the leads and the dot by t. The electron can tunnel from the impurity and escape provided its energy lies above the Fermi level, otherwise it remains trapped. In this picture, the defect has spin 1/2 and its z-component is fixed either to spin up or spin down.

However, so-called exchange processes can take place that effectively flip the spin of the impurity from spin up to spin down, or vice versa, while simultaneously creating a spin excitation in the Fermi sea. This spin exchange qualitatively changes the energy spectrum of the system. When many such processes are taken together, one finds that a new state, known as the Kondo resonance, is generated with exactly the same energy as the Fermi level. Such a resonance is very effective in scattering electrons with energies close to the Fermi energy. Since the same electrons are responsible for the low-temperature conductivity, the strong scattering contributes greatly to the resistance.

When a small system with a well defined number of electrons (like a QDot) is connected to electrodes, Kondo physics can also strongly affect the low-temperature electronic properties of the device [73]. When the number of electrons, N, confined on the island is odd we have a localized spin ($S = 1/2$) between large electron seas in the leads. In this situation, second-order (spin-flipping) processes can occur. Similar processes, which change the total spin on the island , add up coherently to form a correlated many-electron-state in which electrons in the two leads are strongly coupled, allowing current to flow even under blockade conditions if $T \ll T_K$, where T_K is the Kondo temperature. When N is even, however, there is no equivalent process and thus no current ("even-odd asymmetry"). Accordingly, a localized half-integer spin on a QDot acts as a magnetic impurity leading to the Kondo effect which

[1] Traditionally, Kondo effect means the increase of the resistance as the temperature is lowered below a certain threshold (Kondo temperature). Although this behavior does not involve a phase transition, the Kondo temperature completely determines the low-temperature electronic properties of the material. Note that usually a lower temperature implies a lower resistance due to reduced thermal scattering, and the resistance saturates below about 10 K due to static defects, or vanishes below the critical temperature in the case of a superconductor.

now increases the conductance (instead of the resistance) at low temperatures, and is even able to make the dot completely transparent (*unitary limit*). In other words, the Kondo effect produces the opposite behavior in a QDot compared to that of a bulk metal.

Where does this difference originate from? In a real metal, electron states are described by plane waves and scattering from impurities mixes waves with different momenta. The corresponding momentum transfer increases the resistance. In a QDot, all electrons have to travel through the island. The Kondo resonance now makes it easier for states belonging to the two opposite electrodes to mix. This mixing is responsible for the increase of the conductance.

Kondo physics in carbon NTs has been demonstrated experimentally by Nygard *et al.* [70] who considered a 1D QDot formed by a metallic SWNT with 3D metal (gold) reservoirs. This allowed for the observation of Kondo resonances for very large electron numbers on the dot, and approaching the unitary limit.

5.1.3 Tunneling mechanisms

We will now comment on the relevant tunneling mechanisms and the resulting consequences. Sequential tunneling (ST) or, to be more precise, *incoherent resonant tunneling* with independent tunneling events from the leads onto the island and from the island into the other lead, occurs via an unoccupied level within the energy window between μ_L and μ_R, which are the chemical potentials of the left and right lead. The number of electrons on the dot changes according to $N \to N+1 \to N \to N+1 \ldots$. To give an analogy, this would correspond to two one-photon processes in optics. In *coherent resonant tunneling* (CRT) the electron coherently tunnels from one lead through a quantum state on the island to the other lead. Hence, in this case the island should be regarded as a single impurity.

At low temperatures ($k_B T \ll E_c$), the conductance through a QDot in the Coulomb blockade valley is exponentially suppressed. This results from the fact that the process of electron transport through the dot involves a *real* transition to the state in which the charge on the island differs by e from the thermodynamically most favorable value (sequential tunneling). Going beyond the lowest order perturbation theory allows one to consider processes in which states of the dot with a "wrong" charge participate in the tunneling process as *virtual* states.

Cotunneling (CT) is a second order process with only virtual occupation of an energy level on the dot and gives the leading contribution to the activationless transport. Such a process cannot be separated into two steps and would correspond to a two-photon process in optics. In the *inelastic* CT mechanism, an electron tunnels from the lead into one of the vacant single-particle levels on the dot, while an electron occupying some other level tunnels out of the dot, see Fig. 5.5. As a result, transfer of charge e across the island is accompanied by a simultaneous creation of an electron-hole pair on the dot. Inelastic CT wins versus ST at low temperatures.

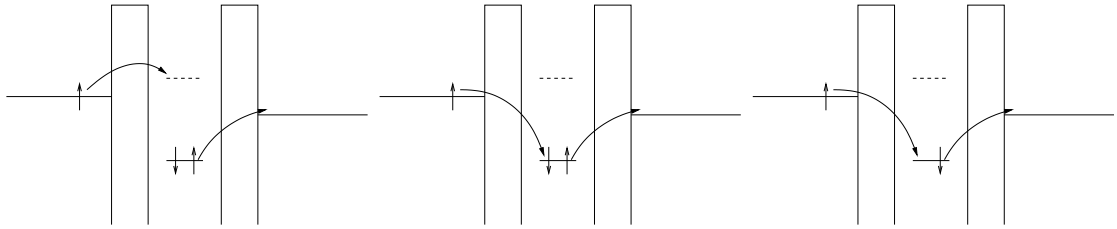

Figure 5.5: *Inelastic (left) and elastic (middle) cotunneling as well as spin-flip cotunneling leading to the Kondo resonance (right).*

Contrarily, in the *elastic* CT process, no electron-hole pairs are excited and the electron tunnels via the same level. In other words, occupation numbers of the energy levels on the dot in the initial and final states of the CT process are exactly the same. At low temperatures, elastic CT is the more important process compared to the inelastic one.

The Kondo effect comes from elastic CT in all orders via the topmost occupied state of the QDot. This state is special since if the number of electrons on the dot is odd, this level is filled by a single electron only and is spin-degenerate. Therefore, the ground state of the QDot is characterized not only by the occupation of the energy levels, but also by the dot's spin. This opens the possibility of a CT process in which the transfer of an electron between the leads is accompanied by a flip of the electron's spin with simultaneous flip of the spin of the island (spin-flip CT process, see Fig. 5.5). The amplitude of such a process, calculated in fourth order in the tunneling matrix element, diverges logarithmically when the energy E of an incoming electron approaches the Fermi energy. Since $E \sim T$, this singularity in the transmission amplitude translates into a dramatic enhancement of the conductance across the island at low temperatures, approaching the unitary limit for $T \to 0$.

5.2 Resonant tunneling in a Luttinger liquid

The problem of resonant tunneling through a double-barrier structure in a LL was first studied a decade ago [37, 74, 75], but has recently attracted renewed and widespread attention by theorists [76-83]. This is primarily caused by novel exciting experimental realizations of double-barrier structures in interacting 1D quantum wires presumably described by LL theory. After reviewing the theoretical results we briefly describe the (not yet completely understood) experimental situation, also as a motivation for our own work presented in the next chapter.

5.2.1 Single-barrier problem

We first want to recall the situation of an infinite LL with a single impurity where the difference to a Fermi liquid already becomes dramatic. According to Landauer's

theory the conductance of a single-channel wire with a barrier is given by $G = |t|^2 G_0$, where $|t|^2$ is the transmission probability through the barrier and $G_0 = e^2/h$. This result holds even at finite temperatures, assuming the transmission probability is independent of energy, as is often the case for barriers that are sufficiently above or below the Fermi energy. In 1D, interactions play a crucial role in that they form charge density correlations which are easily pinned by even the smallest barrier, resulting in *zero* transmission and, hence, a vanishing conductance at zero temperature. At finite temperatures the correlation length is finite and the conductance decreases as a power law of temperature. To understand the line of reasoning we want to explain the situation in a bit more detail and therefore consider a repulsively interacting LL with a single barrier.

We first assume a weak impurity at, say, $x = 0$. In this limit, the barrier itself can be treated as a small perturbation. Integrating out all degrees of freedom away from $x = 0$ leads to an effective action. The resulting problem can be solved by using renormalization group theory, and the corresponding flow equation shows that at very low temperatures the backscattering becomes very strong. This implies that at $T = 0$ even a very small barrier will be impenetrable (scales to infinity), and effectively breaks the system into two decoupled parts. Hence, the conductance should vanish.

In the opposite limit of a large barrier, the perturbative calculation sketched above provides no direct way to treat the problem and hence, the starting point is different. Now, one has to consider a system consisting of two semi-infinite wires coupled by a weak tunneling barrier. This situation can appropriately be described by a tunneling Hamiltonian, and tunneling from one part to the other can be considered as a perturbation. Applying the same steps as before, one finds that the hopping term scales to zero (i.e., the tunneling perturbation is irrelevant) and thus, the conductance again should vanish.

Using Fermi's golden rule, one can express the current through the impurity in terms of the boundary TDOS. At zero temperature and for repulsive interaction, the linear conductance is strictly zero which reflects the suppressed TDOS in a LL. When $g = 1$, a linear $I - V$ curve is predicted, consistent with expectations for non-interacting electrons which are partially transmitted through the barrier. At finite temperature a power-law behavior for the conductance is predicted, $G \sim T^{\frac{2}{g}-2}$.

5.2.2 Double-barrier problem

Is resonant tunneling through a double-barrier structure possible when the system under consideration is an interacting LL? Since even an arbitrarily weak single impurity causes the zero-temperature conductance to vanish, one might have been inclined to guess that a series arrangement of two barriers could only further enhance the backscattering, so that resonances are simply not present at $T = 0$. However, this is not the case and perfect resonances are possible in a (repulsively interacting)

LL incident on a double-barrier structure (in striking contrast to the single-impurity case) but with completely different behavior compared to the standard Fermi liquid case. We note that, as the double-impurity problem in a LL is not integrable, exact solutions covering a wide parameter range of interest for this transport problem are out of reach, in marked contrast to the situation for a single impurity [84].

For simplicity, we focus exclusively on the case of symmetric barriers. Although this case does not seem to be very realistic since any randomness in the barriers and/or nanowire would cause asymmetry, the experimentally reported asymmetry is not very large [71], and the resulting effect can be expected to be small and negligible.

Fermi liquid case

The conductance due to incoherent resonant tunneling of a particle between two Fermi liquid leads is easily calculated using the Landauer formula,

$$\frac{G_{FL}}{G_0} = \int dE \left(-\frac{df}{dE}\right) |t(E)|^2 \ ,$$

where $|t(E)|^2$ has a Lorentzian line shape centered around the resonant energy ϵ_0,

$$|t(E)|^2 = \frac{\Gamma^2}{(E-\epsilon_0)^2+\Gamma^2} \ ,$$

and $f(E)$ is the Fermi function. When $T \gg \Gamma$ (we put $k_B = 1$) one finds that [85]

$$\frac{G_{FL}}{G_0} = \frac{\pi\Gamma}{4T}\frac{1}{\cosh^2[\epsilon/2T]} \ , \tag{5.1}$$

where $\epsilon = \epsilon_0 - \mu$ is the energetic distance from the peak and μ the chemical potential in the leads. The main outcome of this analysis is the line shape of the resonance being the derivative of the Fermi function, its full width at half maximum has a linear dependence on T, and the area under the peak (or the peak height multiplied by T) is proportional to Γ and should be independent of temperature.

Luttinger liquid: spinless case

We now consider the situation of two impurities creating an island between two semi-infinite LL leads in the case of repulsively interacting spinless fermions. Starting from the weak-barrier (strong-tunneling) limit[2] it was shown [37] that for symmetric barriers, resonances with perfect transmission can be achieved by fine-tuning a single parameter, e.g., the gate voltage controlling the number N of electrons on the island.[3] These resonance peaks can be observed at half-integer N and become

[2]This starting point is appropriate for describing coherent transport at low temperatures.

[3]For attractive interactions, the barriers become irrelevant, there are no resonances and one recovers the full LL conductance without fine-tuning.

infinitely sharp as $T \to 0$ which is in striking contrast to the non-interacting case where the line width becomes temperature independent for $T \to 0$. Thus, the interactions suppress all off-resonance conductance, and the conductance exactly at the resonance crucially depends on the interaction strength g. In particular, for $1/4 < g < 1$ one recovers the full LL conductance while for $g < 1/4$ zero conductance is obtained[4] (CRT regime, see [37, 74]). In the regime $1/4 < g < 1/2$ a Kosterlitz-Thouless transition should occur, with the result that for weak barriers there should still be a resonance, while for strong barriers a resonance is only found for $g > 1/2$.

For $g > 1/4$, the $2k_F$-backscattering term $V^{(1)}$ (all other terms are irrelevant) increases under renormalization according to $dV^{(1)}/dl = \lambda V^{(1)}$, where l is the renormalization group flow parameter and $\lambda = 1 - g > 0$. One expects (see [37]) the conductance for small T and ϵ (the energetic distance from the peak) to be described by a universal scaling function,

$$G(T, \epsilon)/G_0 = f_g(X) \;\text{ with }\; X = c\epsilon/T^{1-g} \,, \tag{5.2}$$

where c is a non-universal dimensionful constant. Accordingly, rescaled resonance curves for different temperatures should collapse onto a single universal master curve. For $X \ll 1$ (high temperatures), one finds from a perturbative calculation that

$$f_g(X) = 1 - X^2 + \mathcal{O}(X^4) \,, \;\text{ with }\; X^2 \sim T^{2g-2} \,,$$

while for $X \gg 1$ (low temperatures), one has

$$f_g(X) \approx X^{-2/g} \sim T^{\frac{2}{g}-2} \,,$$

see [37]. The scaling arguments leading to this result can be backed up by an exact non-perturbative calculation (via refermionization) for $g = 1/2$. Moreover, the line shape is predicted to be non-Lorentzian. As a result of (5.2), at low temperatures the resonance width should scale as $w \sim T^{1-g}$.

In 1998, Furusaki [76] has treated the *incoherent* resonant tunneling regime (conventional ST), taking into account CT contributions that are important away from the resonance peak. The incoherent regime allows for a master equation approach, whose validity requires at the least (i) that the barriers are strong (i.e. weak tunneling where $G \ll G_0$), and (ii) that temperature T is sufficiently high. Remarkably,

[4] For $g > 1/4$ only the $2k_F$-backscattering term is relevant and fine-tuning this term to zero then corresponds to tuning to a resonance. For $g < 1/4$ also the $4k_F$-backscattering term becomes relevant and usually destroys the resonance. Higher-order backscattering terms have systematically increasing scaling dimensions and are therefore less relevant. A simple explanation of the infinite sharpness of the resonance can be given as follows. An electron in a localized state between two barriers in a LL is unable to decay at $T = 0$ since the TDOS into the leads vanishes. Hence, the electron remains localized forever, with an infinite lifetime. At finite temperature, the TDOS into a LL is non-zero away from the Fermi energy and thus, the electron will be able to decay resulting in a thermally broadened resonance peak.

for sufficiently strong interactions, $g < 1/2$, the approach works down to zero temperature provided condition (i) is met. However, for $g \geq 1/2$, it breaks down below a temperature T^* determined by the barrier strength, where a crossover to coherent resonant tunneling occurs since then the tunneling rates through the left and right barrier grow with decreasing temperature. Then, the line shape approaches the universal form predicted in [37]. In the incoherent regime, the line width w of the resonance peak has a linear temperature dependence, $w \sim T$, while the peak conductance $G_{\max} \sim T^{\alpha_{\rm end}-1}$.

Experimentally more relevant is the shape of the peak as a control parameter (e.g. the gate voltage) is tuned through the resonance. In the presence of interactions, the tails of the resonance line are expected to be strongly suppressed compared to the non-interacting case. For LL leads, the line shape in the incoherent regime is [76] (we put $\hbar = k_B = 1$)

$$\frac{G_{\rm seq}}{G_0} = \frac{\Gamma_0 (\pi T/D)^{\alpha_{\rm end}}}{4\,\Gamma[1/g] T \cosh[\epsilon/2T]} \left| \Gamma\left[\frac{1}{2g} + i\frac{\epsilon}{2\pi T}\right]\right|^2 , \tag{5.3}$$

where $\Gamma[x]$ denotes the Gamma function, ϵ is the energetic distance from the peak, D the electronic band width, and Γ_0 the hybridization matrix element between leads and the dot. This obviously differs from conventional Fermi liquid predictions, see Eq. (5.1), albeit the difference is not drastic. With the charging energy $E_c = \pi v_F/g^2 d$ for a dot of length d, the quantity ϵ is related to $\delta N = N - 1/2$ via $\epsilon = E_c \delta N$. Furthermore, for a barrier of strength V, with a dimensionless g-dependent constant c_g, the hybridization is $\Gamma_0 = c_g D(\pi V/D)^{-2g}$ [86].

The line shape in Eq. (5.3) is very close to the Fermi liquid case (5.1) and evidently characterized by a linear temperature dependence of the line width. In the tails of a peak, the conductance vanishes exponentially. For not too strong barriers, CT then takes over, with the leading term given by [76]

$$\frac{G_{\rm cot}}{G_0} = \frac{c\Gamma^2[1/g]}{2\Gamma[2/g]} \frac{\Gamma_0^2}{(|\epsilon| + 2\pi T)^2} \left(\frac{\pi T}{D}\right)^{2\alpha_{\rm end}} , \tag{5.4}$$

where c is a dimensionless constant of order unity. Deviations from the $w \sim T$ behavior directly indicate violations of the incoherent ST mechanism, either due to CRT, CT, or because one is outside the strong barrier limit.

Very recent work [82, 83] approached the problem by considering weak electron-electron interactions, $g = 1 - \kappa$, with $\kappa \ll 1$. Then, one does not have to rely on bosonization methods, where technical problems arise for intermediate barrier heights. Generalizing earlier work on the single-barrier limit [87], in Ref. [82] a renormalization method is used to solve the problem in the limit of weak tunneling, however, with partly conflicting results. In [83] the problem is treated using a fermionic renormalization group method. The advantage of this method is that it allows one to treat weak as well as strong barriers on an equal footing. However, the underlying idea of treating resonant tunneling as elastic scattering process is

possible only to lowest order in κ, as electrons are no longer good quasi-particles [83]. Within this limited range of applicability, however, their analysis appears to confirm the standard ST picture of resonant tunneling [37, 74, 76] for strong barriers. In addition, Ref. [83] predicts that for weak barriers at sufficiently low temperatures, a sharp Lorentzian resonance peak with $G_{\max} = G_0$ is possible, whose line width vanishes as a power law. This resonance is predicted to remain perfect down to $T = 0$.

A recently proposed new tunneling mechanism, *correlated* ST [71, 81], which is in contradiction to the incoherent ST picture and therefore led to a controversial discussion in the literature, will be discussed in the next section together with the relevant experimental data.

Luttinger liquid: spinful case

Most of the above picture can be carried over to the case of spinful fermions [76]. However, including spin, there can arise important differences. If the charge on the island is odd, there will be a spin degeneracy as for a local magnetic moment. However, the Kondo effect in a QDot connected to LL leads has been argued to be strongly suppressed [76] except possibly in the coherent low-temperature regime with weak barriers [37]. For a QDot connected to Fermi liquid leads, the logarithmic increase of the conductance with decreasing temperature, reaching the unitary limit for $T \to 0$, reflects the marginal relevance (in the renormalization group sense) of virtual tunneling. The reason for the suppression in the LL case can be seen in Eq. (5.4). Thinking of the Kondo problem as elastic CT in all orders of Γ_0, we see that it should not be present because CT is an irrelevant process at low temperatures,[5] $G_{\rm cot} \propto T^{2\alpha_{\rm end}}$.

For spinful fermions, assuming $SU(2)$ spin invariance, we define g via the relation $g^{-1} = (g_c^{-1} + 1)/2$ [74], where g_c is the usual LL parameter in the charge channel, see also (4.5). For SWNTs we would have $g^{-1} = (g_{c+}^{-1} + 3)/4$, instead.

5.2.3 Experimental results

Auslaender *et al.* [88] have measured the low temperature conductance of a one-dimensional island embedded in a single mode quantum wire. The quantum wire was fabricated using the cleaved edge overgrowth technique and the tunneling was through a single state of the island. Their results show that the resonance line shape can be fitted by (5.1) while the intrinsic line width decreases in a power-law fashion as the temperature is reduced. Their results were claimed to be in quantitative agreement with Furusaki's theory of incoherent resonant tunneling in a LL [76].

[5] Only for $g = 1/2$ there exists an analog of the Kondo effect [76]. Then, one can show [37] that on resonance the tunneling is marginally relevant leading to a logarithmic increase of the conductance with decreasing temperature when higher-order terms are included.

On the other hand, Postma *et al.* [71] have probed transport through a double barrier artificially created in a metallic SWNT (see Fig. 5.6). In metallic NTs, strong bends have been shown to act as nanometer-sized tunnel barriers for electron transport [89], and such NT devices have been fabricated with different island lengths ranging between 20 and 50 nm.

When both bias and gate voltage are tuned, Coulomb diamonds demonstrating Coulomb blockade (i.e., single electron tunneling) are observed. If we consider the temperature dependence of a single conductance peak ($V_b = 0$), the experimental data shows that the peak height $G_{\max}$ and the peak width w both decrease with decreasing temperature (Fig. 5.7). A quantitative analysis reveals a power-law behavior for the conductance maximum at low temperatures, $G_{\max} \sim T^{0.68}$, whereas the resonance width follows a linear temperature dependence, $w \sim T$. Notice that the conductance is predicted to vanish in the limit $T \to 0$.

These experimental results have been interpreted in terms of *correlated* ST [71, 81], since the standard picture of incoherent resonant tunneling [76] is inconsistent with the observed temperature dependence of the conductance peak height. Thorwart *et al.* [81] showed, using a master equation approach in the limit of weak tunneling where one can use the instanton approximation, that higher-order tunneling processes in combination with correlations among tunneling events on and off the island dominate the behavior of G for high temperatures. For thermal lengths larger than the width of the 1D dot, these correlations should invalidate the conventional ST picture leading to a linear temperature dependence of the resonance width, $w \sim T$, and a power-law temperature dependence of the conductance maximum, $G_{\max} \sim T^{\alpha_{\mathrm{end-end}}-1}$. Now, the scaling is governed by $\alpha_{\mathrm{end-end}} = 2\alpha_{\mathrm{end}}$, which is typical for tunneling between the ends of two LLs.[6] However, this mechanism has been questioned by a number of authors [82, 83], but without offering a consistent explanation of the experimental data.

Finally, in this context also other experiments on SWNTs are of interest, where Fabry-Perot type oscillations in the conductance of a double-barrier structure with nearly transparent barriers were observed [65, 90, 91, 92]. Remarkably, it is experimentally possible to tune the barrier strength via additional gate voltages from weak to strong barriers, and to observe the corresponding crossover from Fabry-Perot type oscillatory behavior to ST (Coulomb blockade) peaks [92].

[6] In a coherent tunneling event, the island can be seen as a single impurity and hence, the tunneling occurs between the ends of two LLs. This is a reasonable assumption, since the thermal length $L_T = \hbar v_F / k_B T = 70$ nm at 300 K is larger than the distance between the two barriers in the experiment [71] at all temperatures.

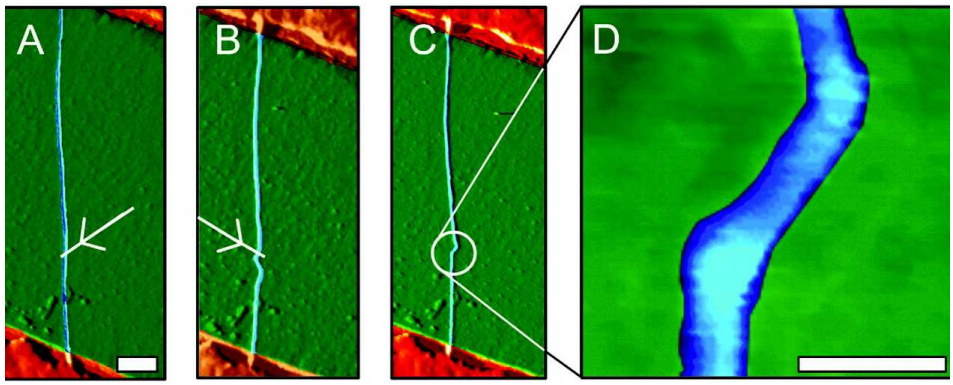

Figure 5.6: *Fabrication of the NT device using an atomic force microscope. (A) NT between Au electrodes on top of a Si/SiO_2 substrate (bar = 200 nm). The tip is pressed down onto the substrate and moved along the path indicated by the arrow. (B) NT after creation of a buckle. A second dragging action is performed as indicated by the arrow. (C) Double-buckle NT device. (D) Enlarged image of the double-buckle device (bar = 20 nm). (Taken from [71].)*

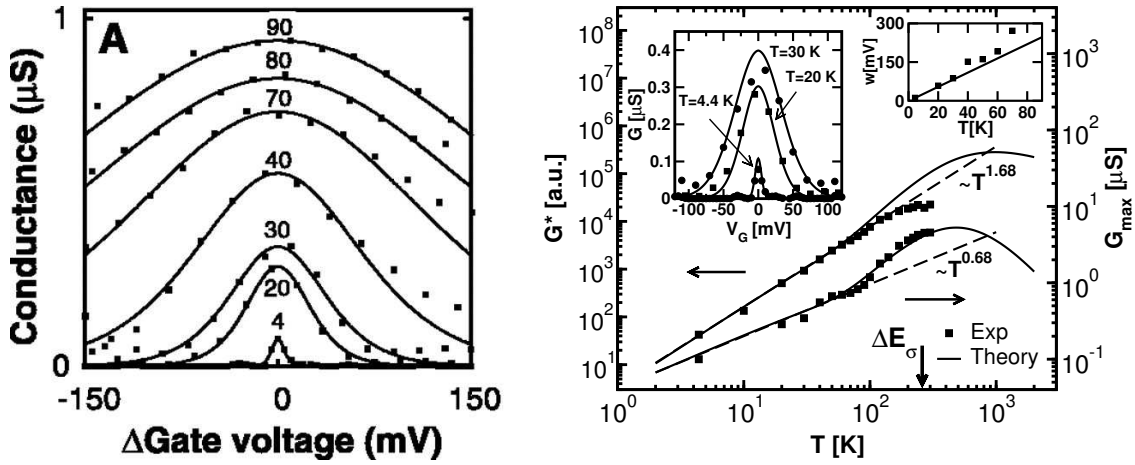

Figure 5.7: *Left: zero-bias conductance versus gate voltage for a single conductance peak. The numbers above the curves indicate the temperature in Kelvin, respectively. Solid lines show fits to Eq. (5.1). (From [71].) Right: quantitative analysis of the measured data. G^* denotes the integrated conductance. Solid lines represent the theoretical prediction for $g_{c+} = 0.23$, dashed lines correspond to the power laws (notice the double-logarithmic scale). The left inset shows single conductance peaks while the right inset shows the peak width versus temperature. (From [81].)*

Chapter 6

Nanotube quantum dot

In this chapter the resonant tunneling through a double-barrier structure in a SWNT is studied. The motivation for this work was given in the last chapter where we reviewed recent experimental results and the resulting controversial discussion of resonant tunneling in a LL.

First, we present a general theoretical model for a LL with two impurities containing the limit of spinless fermions as well as the spinful case and the SWNT. We derive the effective action by integrating out the bulk degrees of freedom away from the location of the two tunneling barriers. Within this model we then determine the resonance condition analytically in both the weak- and strong-barrier limit by means of a cumulant expansion and a symmetry consideration, respectively. Further, in order to obtain the full line shape of the resonance for arbitrary single-barrier transmission, we develop a real-time (Keldysh) quantum Monte Carlo (QMC) approach. An alternative would be to use standard Euclidean-time QMC simulations, and then use analytic continuation techniques to extract the conductance. In Ref. [93], the latter approach was chosen for the single-barrier problem, where the analytic continuation was performed using Padé approximants. We have also tried this for the double-barrier problem, but found it to be completely uncontrolled and unreliable. This is not too surprising as the analytic continuation of numerical data is mathematically ill-defined and known to work only in fortunate cases. In contrast, the Keldysh QMC simulation suffers from the well-known sign problem due to quantum interference of different real-time paths [94]. This poses a problem to simulations at very low temperatures, but nevertheless allows us to study a wide parameter regime of interest in a perfectly well-controlled way. The single-barrier problem was studied successfully by this technique before [95, 96], and the present work represents the generalization to the more challenging double-barrier case. Note that in the single-barrier problem, it has been possible to reach the asymptotic low-temperature regime [95].

Below, we will pay particular attention to how the barrier strength influences the physical mechanisms of transport through the double barrier, having in mind the actual experimental setup of Ref. [92]. To keep the number of free parameters

manageable, we shall present results for the linear conductance only for symmetric barriers and temperatures well below the single-particle spacing on the dot. Thereby we also focus on the most interesting and controversial regime. While it is possible to use our approach also for finite interaction range, we only consider the standard case of an effective short-range interaction.

The validity of our method is demonstrated for the non-interacting case by comparing numerical results to the exact solution (for arbitrary barrier height) which can be obtained via refermionization. We identify the coherent resonant tunneling regime where the line shape shows universal scaling behavior. The line width is found to have a power-law temperature dependence in accordance with theoretical predictions. Further, we identify the regime of correlated sequential tunneling but do not find any evidence for the incoherent sequential tunneling regime which resolves the controversy described in the previous chapter. With spin, we identify resonant tunneling peaks, but no Kondo effect can be found in this setup.

6.1 Theoretical model

To keep our following discussion as general as possible we will consider an infinite LL with $f = 1, 2, 4$ flavors, and $a = 1, \ldots, f$ corresponding to the different channels which are LLs with interaction parameters g_a ($g_1 < 1$ while $g_{a\neq 1} = 1$) and velocities $v_a = v_F/g_a$. The case $f = 1$ describes a spinless LL while $f = 2$ describes the spinful case and $f = 4$ corresponds to a SWNT. Throughout the whole chapter we set $\hbar = 1$.

We consider a SWNT dot formed by two barriers modeled by short-ranged scattering potentials $V_\pm$ centered at $x = \pm d/2$, i.e., $V(x) = \sum_{p=\pm} V_p \delta(x - pd/2)$. This gives rise to the contribution $H_V = \int dx V(x)\rho(x)$ to the Hamiltonian, where $\rho(x) = \psi^\dagger(x)\psi(x)$. Ignoring electron-electron umklapp- and backscattering processes, the Euclidean action in terms of the bosonic phase fields $\theta_a(x, \tau)$ reads

$$S = \frac{1}{2\beta v_F} \sum_{a,n} \int \frac{dk}{2\pi} \left(\omega_n^2 + v_a^2 k^2\right) |\tilde{\theta}_a(k, \omega_n)|^2 + S_{\mathrm{imp}}[q] \,, \tag{6.1}$$

where $\beta = 1/k_B T$ is the inverse temperature and the Matsubara frequencies are $\omega_n = 2\pi n/\beta$. The impurity part is given by [66]

$$S_{\mathrm{imp}}[q] = \sum_{p=\pm} V_p \int_0^\beta d\tau \left\{ \prod_a \cos\left[q_{ap}(\tau) + \frac{p\pi}{f} N_a^{(0)}\right] + \delta_{f4} \prod_a \sin\left[q_{ap}(\tau) + \frac{p\pi}{f} N_a^{(0)}\right] \right\}, \tag{6.2}$$

where we have used the substitution

$$q_{ap}(\tau) = \sqrt{\frac{4\pi}{f}} \theta_a(pd/2, \tau) \tag{6.3}$$

for later convenience. Additionally, we made use of the Fourier conventions

$$\begin{aligned}\theta(x,\tau) &= \frac{1}{\beta}\sum_n \int \frac{dk}{2\pi}\tilde{\theta}(k,\omega_n)e^{i\omega_n\tau+ikx}\ ,\\ \tilde{\theta}(k,\omega_n) &= \int dx\int_0^\beta d\tau\theta(x,\tau)e^{-i\omega_n\tau-ikx} = \tilde{\theta}^*(-k,-\omega_n)\ .\end{aligned}$$

The external "charges" $N_a^{(0)}$ are given by

$$N_a^{(0)} = \sqrt{\frac{f}{\pi}}\int_{-d/2}^{d/2} dx\langle\partial_x\theta_a\rangle\ ,$$

where $\langle\ldots\rangle$ denotes a quantum average with respect to S, and their physical meaning will be discussed later.

To make progress, we integrate out the bulk modes $\theta_a(x)$ away from the location $x = \pm d/2$ of the two tunneling barriers. Since the corresponding Hamiltonian is quadratic, this trace can be performed exactly and is done by introducing Lagrange multipliers to enforce (6.3). Additionally, we introduce new fields according to

$$\begin{aligned}Q_a(\tau) &= \sqrt{f/4\pi}\left\{\theta_a(d/2,\tau)+\theta_a(-d/2,\tau)\right\},\\ N_a(\tau) &= \sqrt{f/\pi}\left\{\theta_a(d/2,\tau)-\theta_a(-d/2,\tau)\right\},\end{aligned} \tag{6.4}$$

so that

$$\theta_a(pd/2,\tau) = \sqrt{\frac{\pi}{f}}\left\{Q_a(\tau)+\frac{p}{2}N_a(\tau)\right\}. \tag{6.5}$$

The physical interpretation of these fields is that the average phase Q_a corresponds to "charge" of type a being transferred across the double barrier and is therefore related to the current I_a through the two barriers, $I_a = (ie/2)(dQ_a/d\tau)$, while the phase difference N_a corresponds to "charge" of type a sitting on the island. We will consider only the equilibrium situation here, and we allow for

$$\langle N_a(\tau)\rangle \equiv N_a^{(0)} = \frac{|\Delta E_a|}{\Delta\epsilon} \neq 0\ ,$$

due to external gates or a magnetic field for $a = c+, s+$, respectively, and $\Delta\epsilon = \pi v_F/fd$ is the level spacing. Therefore, by tuning the gate voltage we can adjust $N_{c+}^{(0)}$ via $|\Delta E_{c+}| = |E_F|$, and by tuning the magnetic field B we can vary $N_{s+}^{(0)}$ via $|\Delta E_{s+}| = g_e\mu_B B$, where g_e denotes the Landé-factor and μ_B the Bohr magneton. In contrast, $N_{c-}^{(0)}$ is not tunable but actually very small[1] so that we can put $N_{c-}^{(0)} = 0$, and $N_{s-}^{(0)} = 0$ always. Since for laboratory magnetic fields $N_{s+}^{(0)}$ is always very small, we mainly focus on $N_{s+}^{(0)} = 0$.

After doing all the algebra (see Appendix C) we finally end up with the effective action

$$S_{\rm eff}[Q_a,N_a] = \sum_{a,n\neq 0}\frac{\pi|\omega_n|}{2f\beta g_a}\left\{\frac{4|\tilde{Q}_a(\omega_n)|^2}{1+e^{-|\omega_n|/\omega_a}}+\frac{|\tilde{N}_a(\omega_n)|^2}{1-e^{-|\omega_n|/\omega_a}}\right\}+\int_0^\beta d\tau V_{\rm eff}[Q_a(\tau),N_a(\tau)]\ , \tag{6.6}$$

[1]This term reflects KK' symmetry breaking and is important for very large barriers only.

where we have introduced $\omega_a = v_a/d$. In order to prevent unphysical ultraviolet divergences, the Matsubara frequencies are restricted by $|\omega_n| \leq \omega_c$, where ω_c denotes a suitable UV cutoff. Further, we have included the zero-mode $n = 0$ into the impurity part, rendering $V_{\rm imp}$ into the effective potential

$$V_{\rm eff}[Q_a, N_a] = V_{\rm imp}[Q_a, N_a] + \frac{1}{2}\sum_a E_a \delta N_a^2 \,, \tag{6.7}$$

where $\delta N_a = N_a - N_a^{(0)}$ and $E_a = \pi v_F/fdg_a^2$ is the charging energy ($a = c+$) or the level spacing ($a = c-, s+, s-$), respectively. Obviously, the field N_a has a mass gap while Q_a remains massless. The impurity potential has the general form

$$V_{\rm imp}[Q_a, N_a] = \sum_p V_p \left\{ \prod_a \cos\left[\frac{2\pi}{f}\left(Q_a + \frac{p}{2}N_a\right)\right] + \delta_{f4} \prod_a \sin\left[\frac{2\pi}{f}\left(Q_a + \frac{p}{2}N_a\right)\right]\right\}. \tag{6.8}$$

Note that the sine term is only present in the $f = 4$ case.

6.2 Resonance condition

The next step is to determine the resonance condition for a system described by the effective model (6.6). This can be done analytically in both the weak- and strong-barrier limit. The central result of this section is summarized in Table 6.1.

6.2.1 Weak-barrier limit

First, we consider the weak-barrier limit where $V_p \ll E_F$. Since N_a has a mass gap, one can safely integrate out all fields $\{N_a\}$ under a cumulant expansion for the effective potential of the field Q_a [74]. For simplicity, we only consider the symmetric case, $V_+ = V_- = V$.

The first order term of the cumulant expansion (which corresponds to $2k_F$-backscattering) is given by $V^{(1)} = \langle V_{\rm imp}\rangle_N$, where $\langle \ldots \rangle_N$ denotes the quantum average over the fields $\{N_a\}$, with the final result (see Appendix D)

$$\begin{aligned} V^{(1)} &= \frac{V}{2^{f-1}} \exp\left[-\frac{\pi^2}{2f^2}\sum_a \langle \delta N_a^2\rangle_N\right] \sum_{\{\sigma_a\}=\pm} \cos\left[\frac{2\pi}{f}\sum_a \sigma_a Q_a\right] \\ &\times \cos\left[\frac{\pi}{f}\sum_a \sigma_a N_a^{(0)}\right]\left(1 + \delta_{f4}\prod_a \sigma_a\right). \end{aligned} \tag{6.9}$$

A resonance in the conductance requires $V^{(1)} = 0$, since otherwise this term would grow under a renormalization group transformation leading to a vanishing conductance at $T = 0$. Assuming $1 + \delta_{f4}\prod_a \sigma_a \neq 0$, the condition for a resonance reads

$$\sum_a \sigma_a N_a^{(0)} = \frac{f}{2}(2n+1) \,, \tag{6.10}$$

with n being an arbitrary integer number. For $f = 1$, Eq. (6.10) implies resonances at $N^{(0)} =$ half-integer, while for $f = 2$ we have

$$\begin{aligned} N_c^{(0)} &= n + n' + 1 = \text{even/odd integer}, \\ N_s^{(0)} &= n - n' = \text{odd/even integer}. \end{aligned}$$

In the case of a SWNT ($f = 4$), we have to take into account that $N_a^{(0)} = 0$ for $a = c-, s-$, and therefore condition (6.10) results in

$$\begin{aligned} N_{c+}^{(0)} &= 2(n + n') + 2 \, , \\ N_{s+}^{(0)} &= 2(n - n') \, . \end{aligned}$$

In the absence of a magnetic field (since then also $N_s^{(0)},\ N_{s+}^{(0)} = 0$), a simple formula summarizes the resonance condition for different f,

$$N_1^{(0)} = \frac{f}{2}(2n + 1) \, , \tag{6.11}$$

where $N_1^{(0)}$ corresponds to the (total) charge channel.

The next step is to check the stability of such a resonance specified by the condition (6.10). Suppose we have tuned the $2k_F$-backscattering term (6.9) to zero, then the transmission will depend on whether the next-to-leading terms are relevant or not (higher-order terms in the cumulant expansion systematically become less relevant). Accordingly, we have to analyze the stability under perturbations that are generated in second order of the cumulant expansion (corresponding to $4k_F$-backscattering),

$$V^{(2)} = \frac{1}{2}\left(\langle V_{\text{imp}}^2 \rangle_N - \langle V_{\text{imp}} \rangle_N^2\right) .$$

The result is also derived in Appendix D and reads

$$\begin{aligned} V^{(2)} &= \frac{V^2}{2^{2f+1}} \sum_{p,p',\{\sigma_a,\sigma_a'\}=\pm} \prod_a \exp\left[i\frac{2\pi}{f}(\sigma_a + \sigma_a')Q_a\right] \exp\left[i\frac{\pi}{f}(p\sigma_a + p'\sigma_a')N_a^{(0)}\right] \\ &\times \left(\exp\left[-\frac{\pi^2}{2f^2}(p\sigma_a + p'\sigma_a')^2 \langle \delta N_a^2 \rangle_N\right] - \exp\left[-\frac{\pi^2}{f^2}\langle \delta N_a^2 \rangle_N\right]\right) \\ &\times \left(1 + \delta_{f4}\prod_a \sigma_a\right)\left(1 + \delta_{f4}\prod_a \sigma_a'\right) . \end{aligned} \tag{6.12}$$

In general, $V^{(2)}$ does not vanish, even on resonance. We now assume that

$$\prod_a \sigma_a \neq -1 \ \text{ and } \ \prod_a \sigma_a' \neq -1 \, , \tag{6.13}$$

which, of course, is only important for the case $f = 4$. To see whether the resonance is stable or not one has to determine the most relevant perturbation generated by $V^{(2)}$. Therefore, we consider the operator

$$\hat{O} = \prod_a \exp\left[i\frac{2\pi}{f}(\sigma_a + \sigma_a')Q_a\right] ,$$

which has the scaling dimension[2] (see Appendix D)

$$\Delta = \frac{2}{f}\sum_a (1+\sigma_a\sigma'_a)g_a \ , \tag{6.14}$$

and becomes relevant for $\Delta < 1$. In the spinless case, $f = 1$, Eq. (6.14) yields

$$\Delta = 2(1+\sigma\sigma')g = 4g \ ,$$

since only $\sigma = \sigma' = \pm 1$ is possible, and hence, $V^{(2)}$ becomes relevant for $g < 1/4$ or, in other words, the resonance remains stable for all $g > 1/4$. For $f = 2$, we have

$$\Delta = (1+\sigma_c\sigma'_c)g_c + (1+\sigma_s\sigma'_s) = 2g_c \ ,$$

since only $\sigma_c = \sigma'_c = \pm 1$ and $\sigma_s = -\sigma'_s$ has to be considered (the case $\sigma_s = \sigma'_s$ is irrelevant, $\Delta > 1$). Accordingly, the resonance remains stable for all $g_c > 1/2$. In the case of a SWNT ($f = 4$) the scaling dimension is

$$\Delta = \frac{1}{2}\left\{(1+\sigma_{c+}\sigma'_{c+})g_{c+} + \sigma_{s+}\sigma'_{s+} + \sigma_{c-}\sigma'_{c-} + \sigma_{s-}\sigma'_{s-} + 3\right\} .$$

The (probably expected) result $\Delta = g_{c+}$ is prevented by (6.13) and hence, one has at least $\Delta = g_{c+} + 1 > 1$. Therefore, $V^{(2)}$ is always irrelevant in this case. This remarkable and surprising result is solely due to the presence of the sine term in the impurity potential (6.8). As a consequence, in SWNTs the resonance remains stable for all values of the interaction strength while for $f \neq 4$ the resonance is only stable for $g_1 > f/4$. Thus, the general stability criterion then reads

$$g_1 > \frac{f}{4}(\delta_{f1} + \delta_{f2}) \ . \tag{6.15}$$

The main results of this section are again summarized in Table 6.1.

6.2.2 Strong-barrier limit

Since the cumulant expansion only works in the weak-barrier limit we need also to check what happens in the opposite case when the barriers are very strong and hence, tunneling is weak. We anticipate that in this limit the physics associated with the Coulomb blockade should become operative. Provided the capacitance of the dot is small, the charge on the island will be fixed, and the charging energy represents a large energy barrier to add another electron. Transmission through the

[2]Operators whose influence grows on large scales (small momenta) are called *relevant*. The problem of relevancy of perturbations can be formulated and solved in a general form. Therefore, we introduce the *scaling dimension* Δ, that is given by $\langle \hat{O}(\vec{r})\hat{O}^\dagger(\vec{r}\,')\rangle \sim |\vec{r}-\vec{r}\,'|^{-2\Delta}$. Then, the following theorem holds: A local perturbation with scaling dimension Δ (and zero conformal spin) is *relevant* if $\Delta < 1$ and *irrelevant* if $\Delta > 1$. The case $\Delta = 1$ is called *marginal* and needs further investigation to decide whether the perturbation needs to be taken into account or not.

f	resonance condition	stability criterion
1	$N^{(0)} = n + \frac{1}{2}$	$g > \frac{1}{4}$
2	$N_c^{(0)} = 2n + 1$	$g_c > \frac{1}{2}$
4	$N_{c+}^{(0)} = 4n + 2$	stable $\forall\ g_{c+}$

Table 6.1: *Resonance condition and stability criterion for the different cases* $f = 1, 2, 4$ *in the absence of a magnetic field.*

dot will thereby be strongly suppressed until the gate voltage is adjusted to a point where the energy cost to add another electron vanishes.

Now, we expect resonances when tunneling events connect different minima of the effective potential [37]. Assuming that we start in a minimum, the hopping process then has to be a symmetry transformation of V_{eff}. Therefore, we consider the general transformation of the variables N_a and Q_a,

$$\begin{aligned} N_a &\rightarrow 2N_a^{(0)} - N_a \ , \\ Q_a &\rightarrow Q_a + \zeta_a \ , \end{aligned} \tag{6.16}$$

which transforms the effective potential (6.7) into (again $V_+ = V_- = V$)

$$\begin{aligned} V_{\text{eff}} \ \rightarrow \ & V \sum_p \left\{ \prod_a \cos\left[\frac{2\pi}{f} \left(Q_a + \frac{p}{2} N_a \right) + \frac{2\pi}{f} \left(\zeta_a - p N_a^{(0)} \right) \right] \right. \\ + \ & \left. \delta_{f4} \prod_a \sin\left[\frac{2\pi}{f} \left(Q_a + \frac{p}{2} N_a \right) + \frac{2\pi}{f} \left(\zeta_a - p N_a^{(0)} \right) \right] \right\} + \frac{1}{2} \sum_a E_a \left(N_a - N_a^{(0)} \right)^2 , \end{aligned}$$

(note that $p \rightarrow -p$ has no influence). If we, for the moment, only consider the transformation of Q_a, we see that there exists a general symmetry of V_{eff} when

$$\begin{aligned} f = 1 \ &: \ \zeta = 0 \ , \\ f = 2 \ &: \ \zeta_a = 0, 1 \ \forall\ a \ , \\ f = 4 \ &: \ \zeta_a = 0, 1, 2, 3 \ \forall\ a \ , \\ &\quad \ \zeta_a = 0, 2 \text{ (each 2 times)} \ , \\ &\quad \ \zeta_a = 1, 3 \text{ (each 2 times)} \ . \end{aligned}$$

This general symmetry, however, does not give rise to a resonance. But when $N_a^{(0)}$ is tuned to a special value, there can be an additional symmetry present. As we will see, the presence of this extra symmetry precisely corresponds to the condition for resonance.

Demanding invariance of V_{eff} under the full transformation (6.16) then leads to the condition

$$\zeta_a + p N_a^{(0)} = \lambda_a^p \bmod f \ ,$$

where λ_a^p is an integer number that can be assumed as $\lambda_a^p = 0, \ldots, f-1$, without loss of generality. Due to the structure of V_{eff} there exists an additional restriction for λ_a^p depending on f,

$$\begin{aligned} f = 1 \;&:\; \lambda^p = 0 \,, \\ f = 2 \;&:\; \lambda_a^p = 0, 1 \;\forall\; a \,, \\ f = 4 \;&:\; \lambda_a^p = \text{even, odd} \;\forall\; a \,. \end{aligned} \tag{6.17}$$

In principle, there are three possibilities for λ_a^p to be composed:

$$(1) \quad \lambda_a^p = 2\eta_a^p \;\; \forall\; a \tag{6.18}$$
$$\Rightarrow \; \zeta_a = \hat{\eta}_a^+ \bmod f \,, \; N_a^{(0)} = \hat{\eta}_a^- \,,$$
$$(2) \quad \lambda_a^p = 2\eta_a^p + 1 \;\forall\; a \tag{6.19}$$
$$\Rightarrow \; \zeta_a = (\hat{\eta}_a^+ + 1) \bmod f \,, \; N_a^{(0)} = \hat{\eta}_a^- \,,$$
$$(3) \quad \lambda_a^p = 2\eta_a^p + \delta_{p-} \;\forall\; a \tag{6.20}$$
$$\Rightarrow \; \zeta_a = \left(\hat{\eta}_a^+ + \frac{1}{2}\right) \bmod f \,, \; N_a^{(0)} = \hat{\eta}_a^- + \frac{1}{2} \,,$$

with integer η's and $\hat{\eta}_a^p = \eta_a^+ + p\eta_a^-$.

For $f = 1$, only (6.20) corresponds to a non-trivial symmetry leading to

$$N^{(0)} = n + \frac{1}{2} \,, \; \zeta = \frac{1}{2} \,,$$

with integer n. Here, a possible magnetic field has, of course, no influence. For $f = 2$, there are several non-trivial additional symmetries possible (see Table 6.2). The absence of a magnetic field, leading to $N_s^{(0)} = 0$, further selects only one of these possibilities,

$$N_c^{(0)} = 2n + 1 \text{ with } \zeta_c = 1 \,, \; \zeta_s = 0 \text{ or } \zeta_c = 0 \,, \; \zeta_s = 1 \,.$$

In [37], this resonance was assigned to a sort of Kondo effect since the transformation with $\zeta_c = 1$, $\zeta_s = 0$ was interpreted as tunneling of an electron from the left to the right lead in combination with a spin flip of the electron and the dot while $\zeta_c = 0$, $\zeta_s = 1$ should correspond to a process where an electron in one lead flips its spin and that of the island. However, as argued in [76], a true Kondo effect (corresponding to elastic CT in all orders) is not possible since CT is irrelevant. As we will show in Sec. 6.4, resonances at odd integer values of $N_c^{(0)}$ correspond to resonant tunneling peaks, but no Kondo effect can be found in this setup. For $B \neq 0$, resonances can (in principle) also occur at $N_c^{(0)} =$ even or $N_c^{(0)} =$ half-integer. However, since then also a precise tuning of $N_s^{(0)}$ to special values is necessary and in general requires very high magnetic fields, $B = 0$ is more important. For $f = 4$, the additional non-trivial symmetries are listed in Table 6.3. For $B = 0$, the only surviving one is

$$N_{c+}^{(0)} = 4n + 2 \text{ with } \zeta_{c+} = 0 \,, \; \zeta_{a\neq 1} = 2 \text{ or } \zeta_{c+} = 1 \,, \; \zeta_{a\neq 1} = -1 \,.$$

		ζ	$N^{(0)}$	λ^+	λ^-
$\hat{\eta}^+ = 2n$	(6.18)	0	$2n$	0	0
	(6.19)	1	$2n$	1	1
	(6.20)	$\frac{1}{2}$	$2n + \frac{1}{2}$	1	0
$\hat{\eta}^+ = 2n + 1$	(6.18)	1	$2n + 1$	0	0
	(6.19)	0	$2n + 1$	1	1
	(6.20)	$-\frac{1}{2}$	$2n - \frac{1}{2}$	1	0

$\zeta_a = \pm\frac{1}{2}\ \forall\ a$	$N_a^{(0)} = 2n \pm \frac{1}{2}\ \forall\ a$
$\zeta_c = \frac{1}{2}\ ,\ \zeta_s = -\frac{1}{2}$	$N_c^{(0)} = 2n + \frac{1}{2}\ ,\ N_s^{(0)} = 2n - \frac{1}{2}$
$(\zeta_c, \zeta_s) = (1,0),\ (0,1)$	$N_c^{(0)} = 2n + 1\ ,\ N_s^{(0)} = 2n$

Table 6.2: *Possible symmetries for $f = 2$ can be combined from the first table (the index a is suppressed). Non-trivial additional symmetries taking into account (6.17) are listed below (corresponding conditions with $c \leftrightarrow s$ are also possible).*

		ζ	$N^{(0)}$	λ^+	λ^-
$\hat{\eta}^+ = 4n$	(6.18)	0	$4n + 2$	2	2
	(6.19)	1	$4n + 2$	3	3
	(6.20)	$\frac{1}{2}$	$4n - \frac{3}{2}$	3	2
$\hat{\eta}^+ = 4n + 1$	(6.18)	1	$4n - 1$	0	2
	(6.19)	2	$4n - 1$	1	3
	(6.20)	$\frac{3}{2}$	$4n - \frac{1}{2}$	1	2
$\hat{\eta}^+ = 4n + 2$	(6.18)	2	$4n$	2	2
	(6.19)	-1	$4n$	3	3
	(6.20)	$-\frac{3}{2}$	$4n + \frac{1}{2}$	3	2
$\hat{\eta}^+ = 4n + 3$	(6.18)	-1	$4n + 1$	0	2
	(6.19)	0	$4n + 1$	1	3
	(6.20)	$-\frac{1}{2}$	$4n + \frac{3}{2}$	1	2

$\zeta_{c+,s+} = 1\ ,\ \zeta_{c-,s-} = 2$	$N^{(0)}_{c+,s+} = 4n + 3$
$(\zeta_{c+}, \zeta_{s+}, \zeta_{c-,s-}) = (1,-1,2),\ (2,0,-1)$	$N^{(0)}_{c+} = 4n + 3\ ,\ N^{(0)}_{s+} = 4n + 1$
$(\zeta_{c+}, \zeta_{s+}, \zeta_{c-,s-}) = (2,0,2),\ (-1,1,-1)$	$N^{(0)}_{c+} = 4n\ ,\ N^{(0)}_{s+} = 4n + 2$

Table 6.3: *Possible symmetries for $f = 4$ can be combined from the first table (the index a is suppressed). Non-trivial additional symmetries taking into account (6.17) are listed below (corresponding conditions with $c+ \leftrightarrow s+$ are also possible).*

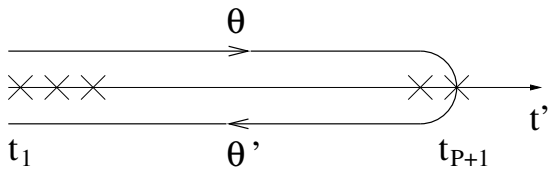

Figure 6.1: *Keldysh contour $\mathcal{C}$ with the field θ living on the forward branch, and θ' on the backward branch.*

In the presence of a magnetic field, resonances are (in principle) possible for all integer values of $N_{c+}^{(0)}$, however, one would expect no "half-integer resonances".

Thus, in the absence of a magnetic field, where we effectively have $N_{a\neq 1}^{(0)} = 0$, the only non-trivial condition for an extra symmetry is

$$N_1^{(0)} = \frac{f}{2}(2n+1) \; ,$$

which coincides with the resonance condition (6.11) obtained from the cumulant expansion in the weak-barrier limit.

6.3 Functional integral approach

In this section we develop a real-time (Keldysh) functional integral approach that allows for the numerically exact computation of the conductance at finite temperature and possibly finite voltage through the quantum dot. For simplicity, we only consider $f = 1, 2$ (charge and possibly spin). To formulate the QMC algorithm, we use the linear combinations introduced in (6.4). The quadratic part of the Euclidean action, after integrating out the boson-field degrees of freedom away from $x = \pm d/2$, is then

$$S_E = \sum_{a,\omega_n} \frac{\pi|\omega_n|}{2f g_a \beta} \left\{ \frac{4|\tilde{Q}_a(\omega_n)|^2}{1+\exp[-|\omega_n|/\omega_a]} + \frac{|\tilde{N}_a(\omega_n)|^2}{1-\exp[-|\omega_n|/\omega_a]} \right\}, \tag{6.21}$$

see also (6.6). We will now develop a QMC scheme for the conductance similar to Ref. [95].

Consider the discretized Keldysh contour $\mathcal{C}$ running from $t = 0$ to $t_{\max}$ and back to zero,[3] see Fig. 6.1. We keep $t_{\max}$ finite and define the time spacing by $\Delta_t = t_{\max}/P$ with Trotter number P. At times $t_j = (j-1)\Delta_t$ for $j = 1, \ldots, P$, we have the fields

[3]The actual idea of Keldysh-formalism is that the system under consideration is in a well defined equilibrium state at $t = -\infty$. Then, one propagates the system in time up to the point $t = +\infty$ (the contour runs infinitesimally above the real axis) thereby adiabatically switching on the interaction and other physical influences. Afterwards, one propagates back to $t = -\infty$ (the contour now runs infinitesimally below the real axis). Thus, all influences besides the interaction cancel since the contour is passed through in both directions leading to the opposite sign.

Q_{aj}, N_{aj} living on the forward branch, and Q'_{aj}, N'_{aj} on the backward branch. Note that the unknown initial state is unimportant since we only need the QMC result for $t \to \infty$ which, of course, is independent of the initial state.

The impurity contribution to the action (where the weight in the real-time functional integral is $\exp[iS]$) is found from (6.5), (6.8) with $S_{\rm imp} = -\sum_{j=1}^{P} \Delta_t \{V_{\rm imp}(j) - V'_{\rm imp}(j)\}$,

$$S_{\rm imp} = -\sum_{p=\pm} \Delta_t V_p \sum_{j=1}^{P} \left\{ \prod_a \cos\left[\sqrt{\frac{4\pi}{f}}\theta_{aj}(pd/2)\right] - \prod_a \cos\left[\sqrt{\frac{4\pi}{f}}\theta'_{aj}(pd/2)\right] \right\}.$$

To do the QMC, it is convenient to switch to the Coulomb gas picture by expanding the impurity propagator for sufficiently small $\Delta_t V_p$. Following Ref. [95], we choose a second-order propagator (so the short-time propagator is correct up to third-order corrections in $\Delta_t V_p$). With Coulomb gas charges σ_{ajp} (σ'_{ajp}), that live on the forward (backward) branch of $\mathcal{C}$ and can take values $0, \pm 1, \pm 2$, the expansion reads (see Appendix E for details)

$$\begin{aligned} e^{iS_{\rm imp}} &= \sum_{\{\sigma,\sigma'\}=0,\pm1,\pm2} \left(\prod_{j,p} G_p^{(f)}(\sigma_{ajp}) G_p^{*(f)}(\sigma'_{ajp}) \right) \\ &\times \exp\left[-i\frac{2\pi}{f} \sum_{a,j,p} \left\{ \sigma_{ajp}\left(Q_{aj} + \frac{p}{2}N_{aj}\right) - \sigma'_{ajp}\left(Q'_{aj} + \frac{p}{2}N'_{aj}\right) \right\} \right]. \end{aligned} \tag{6.22}$$

From there we can easily read off the explicit form of the propagators $G_p^{(f)}(\sigma)$. It is most convenient to switch at this stage to half-integer or integer "quasi-classical" charges $\eta_{ajp} = (\sigma_{ajp} + \sigma'_{ajp})/2$, and integer "quantum" charges $\xi_{ajp} = \sigma_{ajp} - \sigma'_{ajp}$. Since $|\sigma|, |\sigma'| \leq 2$, we have (for both signs) to ensure $|\eta_{ajp} \pm \frac{1}{2}\xi_{ajp}| \leq 2$, and, in addition, these numbers must be integer, i.e., one cannot choose η freely for given ξ and vice versa. In order to have the product GG^* in the Coulomb gas expansion (6.22) valid up to order $(\Delta_t V_p)^2$, one must have $|\xi_{ajp}| \leq 2$ and

$$|\eta_{ajp} + \frac{1}{2}\xi_{ajp}| + |\eta_{ajp} - \frac{1}{2}\xi_{ajp}| \leq 2\,,$$

(this statement is non-trivial but can easily be checked explicitly). The respective non-zero entries of the "Greens function"

$$\tilde{G}_p^{(f)}(\xi_a, \eta_a) = G_p^{(f)}(\xi_a + \eta_a/2) G_p^{*(f)}(\xi_a - \eta_a/2) \tag{6.23}$$

are shown in Tables 6.4 and 6.5 for $f = 1$ and $f = 2$, respectively. Because of the IR divergence in the Q_a-action (6.21), only configurations subject to electroneutrality in the form

$$\sum_{j=1}^{P} \sum_{p=\pm} \xi_{ajp} = 0 \tag{6.24}$$

for arbitrary a do contribute to the partition function.

ξ	η	$\tilde{G}_p^{(1)}$
0	0	$1-2\alpha_p^2$
0	± 1	α_p^2
1	$\pm 1/2$	$\mp i\alpha_p$
-1	$\pm 1/2$	$\pm i\alpha_p$
± 2	± 1	$-\alpha_p^2/2$
± 2	∓ 1	$-\alpha_p^2/2$
± 2	0	α_p^2

Table 6.4: *Non-zero entries of the Greens function (6.23) for the spinless case* $f=1$. *We use* $\alpha_p = \Delta_t V_p/2$.

We now need to address the coupling to external voltages. First, the coupling to a gate voltage favors an "external charge" $N^{(0)}$ on the dot in the $a=1$ channel. This can be introduced by letting $N_1 \to N_1 + N^{(0)}$ on both branches of the Keldysh contour. Using Eq. (6.22), this leads to a factor

$$\mathcal{A}_{\text{gate}} = \exp\left[-\frac{i\pi N^{(0)}}{f}\sum_{j=1}^{P}\sum_{p=\pm} p\xi_{1jp}\right]$$

in the real-time partition function. Second, the applied bias voltage V_b can be introduced by noting that Q_1 is just the charge transferred across the dot. This amounts to shifting Q_1 on both branches according to

$$Q_1(t) \to Q_1(t) + \frac{feV_b}{2\pi}(t-t_0)\ ,$$

with some arbitrary reference time t_0 that drops out finally due to electroneutrality (6.24) . This shift definitely works in the weak-barrier limit, as is clear from Ref. [97]. However, up to the usual prefactor discussion of factors of g_c due to the influence of attached reservoirs, it also works in the opposite limit of strong barriers, as is explained in the appendix of Ref. [37]. We then expect that this prescription really works throughout the whole parameter space, albeit possibly prefactors in the strong-barrier limit could be wrong. Using again Eq. (6.22) this leads to the factor

$$\mathcal{A}_{\text{bias}} = \exp\left[-i\Delta_t eV_b\sum_{j=1}^{P} j\sum_{p=\pm}\xi_{1jp}\right]$$

in the partition function. With the above shift in Q_1, the current-voltage characteristics can be obtained from

$$I(V_b) = (fe^2/h)V_b + e\langle\dot{Q}_1\rangle\ .$$

While our QMC method can obtain the full non-linear conductance, we focus exclusively on the linear conductance,

$$\frac{G}{fe^2/h} = 1 - \lim_{t\to\infty}\partial_t I_B(t)\ . \tag{6.25}$$

ξ_1	ξ_2	η_1	η_2	$\tilde{G}_p^{(2)}$
0	0	0	0	$1-4\alpha_p^2$
0	0	±1	±1	α_p^2
±1	±1	$\mp1/2$	$\mp1/2$	$i\alpha_p$
±1	∓1	$\mp1/2$	$\pm1/2$	$i\alpha_p$
±1	±1	$\pm1/2$	$\pm1/2$	$-i\alpha_p$
±1	∓1	$\pm1/2$	$\mp1/2$	$-i\alpha_p$
±2	±2	0	0	α_p^2
±2	∓2	0	0	α_p^2
±2	0	±1	0	$-\alpha_p^2$
±2	0	∓1	0	$-\alpha_p^2$
±2	0	0	±1	α_p^2
±2	0	0	∓1	α_p^2
0	±2	±1	0	α_p^2
0	±2	∓1	0	α_p^2
0	±2	0	±1	$-\alpha_p^2$
0	±2	0	∓1	$-\alpha_p^2$

Table 6.5: *Non-zero entries of the Greens function (6.23) for the spinful case $f=2$. Here we use $\alpha_p = \Delta_t V_p/4$.*

We thus have to compute $I_B(t)$ at sufficiently long times, where the time derivative can be obtained easily by numerical differentiation of the expectation value

$$I_B(t_j) = -\frac{2\pi}{f}\partial_{V_b}\left\langle \frac{Q_{1j}+Q'_{1j}}{2}\right\rangle = \langle \hat{I}_B(t_j)\rangle \ . \tag{6.26}$$

From Eq. (6.22) it is apparent that we can extract the expectation value (6.26) by considering

$$\sum_p \frac{\partial}{\partial \xi_{1jp}} \exp\left[-i\frac{\pi}{f}\sum_{a,k,p'}\xi_{akp'}\left\{Q_{ak}+Q'_{ak}+\frac{p'}{2}(N_{ak}+N'_{ak})\right\}\right] = -\frac{2\pi i}{f}(Q_{1j}+Q'_{1j})\exp[\ldots] \ ,$$

such that we get I_B from the formal correspondence

$$\hat{I}_B(t_j) = \partial_{V_b}\frac{1}{2i}\sum_{p=\pm}\frac{\partial}{\partial\xi_{1jp}} \ .$$

The ξ-derivative does not act on ξ's in the Greens function $\tilde{G}$ nor on the bias factors $\mathcal{A}_{\rm bias}$ and $\mathcal{A}_{\rm gate}$, but only on terms coming from the expansion (6.22). Alternatively, one can develop a generating functional approach that leads to the same final

answers. Expanding $\mathcal{A}_{\rm bias}$ to lowest order in V_b finally gives

$$I_B(t_k) = \frac{1}{Z}\sum_{\{\xi,\eta\}} \exp\left[-i\frac{\pi N^{(0)}}{f}\sum_{j,p} p\xi_{1jp}\right]\left(\prod_{j,p}\tilde{G}_p^{(f)}(\xi_{ajp},\eta_{ajp})\right) A_k(\xi,\eta)\ ,$$

with

$$A_k(\xi,\eta) = -\frac{1}{2}\left(\sum_{j',p'} j'\xi_{1j'p'}\right)\sum_{p'}\frac{\partial}{\partial\xi_{1kp'}}\left\langle \exp\left[-i\frac{\pi}{f}\sum_{a,j,p}\right.\right. \tag{6.27}$$
$$\times\quad \left.\left.\left\{\xi_{ajp}\left(Q_{aj}+Q'_{aj}+\frac{p}{2}(N_{aj}+N'_{aj})\right)+\eta_{ajp}\left(Q_{aj}-Q'_{aj}+\frac{p}{2}(N_{aj}-N'_{aj})\right)\right\}\right]\right\rangle .$$

It then only remains to compute the above average which is over the Gaussian Q_a, N_a degrees of freedom (see Appendix E). This is an equilibrium average which is most conveniently done in Euclidean time using S_E in Eq. (6.21), supplemented by analytic continuation to real time (which here is unproblematic since done exactly). The result can be put into the standard framework of dissipative quantum mechanics [86] by defining spectral densities

$$J_{\pm,a}(\omega) = \frac{\pi g_a\omega}{f}\left(1\pm\cos[\omega/\omega_a]\right)e^{-\omega/\omega_c}\ .$$

Associated correlation functions are ($\lambda=\pm$)

$$L_a^\lambda(t) = \frac{1}{\pi}\int_0^\infty d\omega\frac{J_{\lambda,a}(\omega)}{\omega^2}\frac{\cosh[\omega(\beta/2-it)]-\delta_{\lambda,+}\cosh[\omega\beta/2]}{\sinh[\omega\beta/2]}\ ,$$

where the subtraction of the $t=0$ part for $\lambda=+$ reflects the IR divergence leading to electroneutrality (6.24). The resulting contribution to the action, the so-called "influence functional" $S'=i\Phi$ [86], is then in discretized notation given by

$$\Phi = \sum_{a,p,p'}\sum_{j=1}^{P}\sum_{k=1}^{j}\left\{\xi_{ajp}\left(S^+_{ajk}+pp'S^-_{ajk}\right)\xi_{akp'}+2i\xi_{ajp}\left(R^+_{ajk}+pp'R^-_{ajk}\right)\eta_{akp'}\right\}, \tag{6.28}$$

with matrices for $k<j$ given by

$$\begin{aligned} S^\lambda_{ajk} &= \mathrm{Re}\left[L_a^\lambda([j-k]\Delta_t)\right], \\ R^\lambda_{ajk} &= \mathrm{Im}\left[L_a^\lambda([j-k]\Delta_t)\right], \end{aligned}$$

and diagonal elements [98] (see Appendix E)

$$\begin{aligned} R^\lambda_{ajj} &= -\frac{1}{\pi}\int_0^\infty d\omega\frac{J_{\lambda,a}(\omega)}{\omega^2}\frac{1-\sin[\omega\Delta_t]/\omega\Delta_t}{\omega\Delta_t}\ , \\ S^\lambda_{ajj} &= \frac{1}{\pi}\int_0^\infty d\omega\frac{J_{\lambda,a}(\omega)}{\omega^2}\coth[\omega\beta/2]\left\{\frac{1-\cos[\omega\Delta_t]}{(\omega\Delta_t)^2}-\frac{1}{2}\delta_{\lambda,+}\right\}. \end{aligned}$$

Note that the influence functional (6.28) then has the real part

$$\Phi' = \frac{1}{2}\sum_{a,p,p'}\sum_{j,k}\xi_{ajp}\xi_{akp'}\left\{S^+_{ajk}+pp'S^-_{ajk}\right\}, \tag{6.29}$$

ξ	$G_p^{(1)}(\xi, z)$	$G_p'^{(1)}(\xi, z)$
0	$1 - 2\alpha_p^2(1 - \cos z)$	$-2\alpha_p^2 \sin z$
± 1	$\pm 2\alpha_p \sin[z/2]$	$\pm\alpha_p \cos[z/2]$
± 2	$\alpha_p^2(1 - \cos z)$	$\alpha_p^2 \sin z$

Table 6.6: *Greens function (6.31) for the spinless case $f = 1$. Listed is also the derivative $G' = \partial_z G$ needed later on. We use $\alpha_p = \Delta_t V_p/2$.*

ξ_1	ξ_2	$G_p^{(2)}(\xi_1, \xi_2, z_1, z_2)$	$G_p'^{(2)}(\xi_1, \xi_2, z_1, z_2)$
0	0	$1 - 4\alpha_p^2(1 - \cos z_1 \cos z_2)$	$-4\alpha_p^2 \sin z_1 \cos z_2$
± 1	± 1	$\pm 2\alpha_p \sin[(z_1 + z_2)/2]$	$\pm\alpha_p \cos[(z_1 + z_2)/2]$
± 1	∓ 1	$\pm 2\alpha_p \sin[(z_1 - z_2)/2]$	$\pm\alpha_p \cos[(z_1 - z_2)/2]$
0	± 2	$2\alpha_p^2(\cos z_1 - \cos z_2)$	$-2\alpha_p^2 \sin z_1$
± 2	0	$-2\alpha_p^2(\cos z_1 - \cos z_2)$	$2\alpha_p^2 \sin z_1$
± 2	± 2	$\alpha_p^2(1 - \cos[z_1 + z_2])$	$\alpha_p^2 \sin[z_1 + z_2]$
± 2	∓ 2	$\alpha_p^2(1 - \cos[z_1 - z_2])$	$\alpha_p^2 \sin[z_1 - z_2]$

Table 6.7: *Greens function (6.31) for the spinful case $f = 2$ (only nonzero entries are shown). We use $\alpha_p = \Delta_t V_p/4$. The derivative is with respect to z_1, $G' = \partial_{z_1} G$.*

where we redefine the diagonal elements $S^-_{ajj} \to 2S^-_{ajj}$, and define the elements for $j < k$ symmetrically (we do this only in the real part). The imaginary part of Φ can be written as $-i \sum_{a,k,p} z_{akp}(\xi_a)\eta_{akp}$, with auxiliary variables

$$z_{akp}(\xi_a) = -2 \sum_{j \geq k} \sum_{p'} \xi_{ajp'} \left\{ R^+_{ajk} + pp' R^-_{ajk} \right\}. \tag{6.30}$$

Since the η's only appear linearly (and otherwise only in $\tilde{G}$), we can now perform the trace over all η-variables analytically. This leads to effective Greens functions

$$G_p^{(f)}(\xi_{ajp}, z_{ajp}) = \sum_{\{\eta\}} \tilde{G}_p^{(f)}(\xi_{ajp}, \eta_{ajp}) \exp\left[i \sum_a z_{ajp}\eta_{ajp} \right], \tag{6.31}$$

where the sum goes over the possible values of η_{ajp} for a given ξ-configuration. Carrying out the summation leads to Tables 6.6 and 6.7 for $f = 1$ and $f = 2$, respectively.

Since the integrand in the partition function is invariant under the change $\xi \to -\xi$ for all charges, the gate voltage factor can be written as a cosine. We can then perform the formal ξ-derivative in Eq. (6.27) and obtain

$$I_B(t_k) = \frac{1}{Z} \sum_{\{\xi\}} A_k(\xi) \cos\left[\pi N^{(0)} \sum_{j,p} \frac{p\xi_{1jp}}{f} \right] \exp[-\Phi'] \prod_{j,p} G_p^{(f)}(\xi_{ajp}, z_{ajp}) \,, \tag{6.32}$$

where the normalization is obtained for $A_k \to 1$, the ξ's are subject to electroneutrality (6.24), Φ' is specified in Eq. (6.29), and the z's in Eq. (6.30). The A_k follow from Eq. (6.27)

$$A_k = -\frac{1}{2}\left(\sum_{j',p'} j'\xi_{1j'p'}\right)\left(-2\sum_{j,p} S^+_{1jk}\xi_{1jp} + \sum_{j,p,p'} \frac{\partial z_{1jp}}{\partial \xi_{1kp'}} \frac{G_p'^{(f)}(\xi_{ajp}, z_{ajp})}{G_p^{(f)}(\xi_{ajp}, z_{ajp})}\right).$$

With Eq. (6.30), we get for $j \leq k$ (otherwise zero):

$$\sum_{p'} \frac{\partial z_{1jp}}{\partial \xi_{1kp'}} = -4R^+_{1kj} \ ,$$

and hence the final form

$$A_k = \Delta_t \left(\sum_{j',p'} j'\xi_{1j'p'}\right)\left(\sum_{j,p} S^+_{1jk}\xi_{1jp} + 2\sum_{j\leq k,p} R^+_{1kj} \frac{G_p'^{(f)}(\xi_{ajp}, z_{ajp})}{G_p^{(f)}(\xi_{ajp}, z_{ajp})}\right).$$

This is a real-valued quantity, as are all the other quantities appearing in Eq. (6.32). Remarkably, although we are dealing with a real-time sign problem, it effectively looks just like a fermion one.

6.4 Non-interacting case

We now discuss resonant tunneling for a 1D non-interacting electron gas corresponding to $g = 1$ in the LL picture. This special case is very convenient since it allows for an exact solution via refermionization, where gate and bias voltages are coupled in exactly as in the previous section. The analytical result obtained here will then serve as a precise check to be passed by our QMC approach. For simplicity, we will only consider symmetric barriers while our QMC method can also handle the asymmetric case.

For $g = 1$ and spinless fermions, the time-dependent Hamiltonian equivalent to the action studied in the last section is (see also (4.1))

$$H(t) = \frac{v_F}{2}\int dx \ \left\{\Pi^2 + (\partial_x\theta)^2\right\} + V\sum_{p=\pm} \cos\left[p\pi N^{(0)} + \sqrt{4\pi}\theta(pd/2, t) + eV_b t\right]. \tag{6.33}$$

The current is then

$$I = \frac{e^2}{h}V_b + \frac{e}{\sqrt{\pi}}\langle\partial_t\theta(x,t)\rangle \ , \tag{6.34}$$

where x is arbitrary and $t \to \infty$. Below we evaluate the current at $x \to \infty$. Using

$$\lambda = \pi V/\omega_c \tag{6.35}$$

as dimensionless barrier strength parameter (ω_c is the UV cutoff), we can refermion-

ize the Hamiltonian (6.33) using fermion operators for right- and left-movers ($r = \pm$) according to (4.2). The refermionized Hamiltonian is then

$$H(t) = -iv_F \sum_{r=\pm} r \int dx\ \psi_r^\dagger \partial_x \psi_r + v_F \lambda \sum_{p,r=\pm} \psi_r^\dagger(pd/2)\psi_{-r}(pd/2) e^{ir(p\pi N^{(0)} + eV_b t)}$$

(see also (4.4)) leading to the equations of motion

$$\left(\frac{1}{v_F}\partial_t \pm \partial_x\right)\psi_\pm^\dagger(x,t) = i\lambda \sum_{p=\pm} \delta(x - pd/2) e^{\mp i(p\pi N^{(0)} + eV_b t)} \psi_\mp^\dagger(x,t)\ .$$

Away from $x = \pm d/2$, the solutions are simply plane waves, which are connected via standard jump conditions (details of the following computation are given in Appendix F). Using the ansatz

$$\psi_r^\dagger(x,t) = \int \frac{dk}{2\pi} e^{-iv_F kt + irkx} \times \begin{cases} a_{rk}^\dagger\ , & x < -d/2 \\ b_{rk}^\dagger\ , & |x| < d/2 \\ c_{rk}^\dagger\ , & x > d/2 \end{cases} \tag{6.36}$$

these conditions read

$$\begin{pmatrix} b_{+,k}^\dagger \\ b_{-,k-eV_b/v_F}^\dagger \end{pmatrix} = \mathcal{T}_{a\to b} \begin{pmatrix} a_{+,k}^\dagger \\ a_{-,k-eV_b/v_F}^\dagger \end{pmatrix} \tag{6.37}$$

with the transfer matrix

$$\mathcal{T}_{a\to b} = \frac{1}{4-\lambda^2} \begin{pmatrix} 4+\lambda^2 & i4\lambda e^{i(\pi N^{(0)} + kd - eV_b d/2v_F)} \\ -i4\lambda e^{-i(\pi N^{(0)} + kd - eV_b d/2v_F)} & 4+\lambda^2 \end{pmatrix}, \tag{6.38}$$

and a similar transfer matrix $\mathcal{T}_{b\to c}$ where the only change is the sign in the argument of the exponential function. Then, we can express the c's in terms of the a's using $\mathcal{T}_{a\to c} = \mathcal{T}_{b\to c}\mathcal{T}_{a\to b}$. Finally, the current follows from translating Eq. (6.34) into the fermionic picture,

$$I = \frac{e^2}{h} V_b - \frac{ev_F}{h} \int dk \left\{ \langle c_{+k}^\dagger c_{+k} \rangle - \langle c_{-k}^\dagger c_{-k} \rangle \right\}. \tag{6.39}$$

Expressing c_{+k} in terms of a_{+k} and c_{-k}, and using

$$\langle a_{+k}^\dagger a_{+k} \rangle = \langle c_{-k}^\dagger c_{-k} \rangle = f(v_F k) = \frac{1}{e^{v_F k\beta} + 1}\ , \tag{6.40}$$

it is a straightforward matter to obtain the linear conductance in closed form for $g = 1$, arbitrary temperature, and arbitrary barrier height (6.35). The result is with

$$w(\lambda) = \frac{(4-\lambda^2)^2}{8\lambda(4+\lambda^2)} \tag{6.41}$$

and the derivative of the Fermi function, $-df/dE = \beta/4\cosh^2[E\beta/2]$, given by

$$\frac{G(N^{(0)},\beta)}{G_0} = \int_{-\infty}^{\infty} dE \left(-\frac{df}{dE}\right) \frac{w^2}{\cos^2[\pi(N^{(0)}+E/\Delta\epsilon)]+w^2} \,, \tag{6.42}$$

where $\Delta\epsilon = \pi v_F/d$ and $G_0 = e^2/h$ (see Fig. 6.2). We stress that this solution is valid for arbitrary barrier height λ as long as $\beta\omega_c \gg 1$; otherwise bosonization and refermionization are only approximations. Furthermore, for the spin-1/2 case ($f = 2$), with G now measured in units of $G_0 = 2e^2/h$, the solution (6.42) also applies with the changes $N^{(0)} \to N^{(0)}/2$ and $\lambda \to \lambda/2$. From Eq. (6.42) we observe that the resonance is always located at half-integer values of $N^{(0)}/f$, where the conductance is periodic in $N^{(0)}$ with period f (we put $0 \leq N^{(0)} \leq f$). This shows that the $f = 2$ peaks at odd integer $N^{(0)}$ as predicted in previous sections and observed in the QMC data below just correspond to standard resonant tunneling peaks since there is no Kondo effect in the non-interacting limit.

The infinite-barrier limit is reached already for $\lambda = 2$, see Eq. (6.41), where the associated phase shift is in the unitary limit and further increase of λ would lead to unphysical predictions. In that limit, $w(\lambda) \to 0$ and the conductance indeed vanishes for all $N^{(0)}$ as it should. The exact formula (6.42) with (6.41) captures also the weak-barrier limit. For $T = 0$, Eq. (6.42) simply yields

$$\frac{G(N^{(0)})}{G_0} = \frac{1}{1+(\cos[\pi N^{(0)}]/w)^2} \,. \tag{6.43}$$

For weak barriers ($w \gg 1$), the dimensionless conductance then has the broad line shape $G(N^{(0)})/G_0 = 1-(\cos[\pi N^{(0)}]/w)^2$, where it is meaningless to speak of a line width. For strong barriers, Eq. (6.43) leads to the standard Breit-Wigner Lorentzian line shape for the resonance peak, with line width $w\Delta\epsilon/\pi$.

Since the line shape in both the strong- and weak-barrier limits can be characterized by the single parameter w, we also compare our QMC data for $g < 1$ below to Eq. (6.43), taking $w = w_g(\beta)$ as fit parameter.

6.5 Quantum Monte Carlo

We first want to give a brief introduction to Monte Carlo (MC) methods by summarizing the basics of this technique. In the next step, we explain in detail our quantum Monte Carlo (QMC) algorithm used to compute the conductance according to the results of Sec. 6.3, and demonstrate its applicability by comparing the numerical results for $g = 1$ to the exact solution (6.42). In the remainder of this section, we then present the results for spinless and spinful interacting fermions as well as a detailed discussion where we draw connections to the models and experiments described in Sec. 5.2.

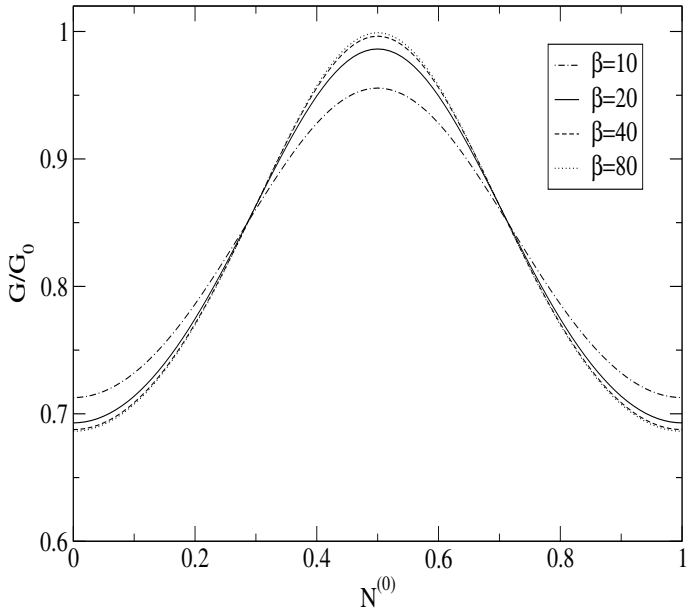

Figure 6.2: *Conductance peak according to (6.42) for different temperatures, barrier strength* $\lambda = \pi/10$*, and* $\Delta\epsilon = \pi/2$ *(we put* $\omega_c = 1$*). As one can see, the zero-temperature limit is already approximately reached for* $\beta = 40$*.*

6.5.1 Basics

A long sequence of random numbers constitutes the backbone of any MC simulation [99]. The MC technique is a powerful numerical technique to solve problems involving high-dimensional integrals and derives its name from a game very popular in Monaco. The children get together at the beach and throw pebbles at random on a square which has a circle inscribed in it. From the fraction of the pebbles that fall inside the circle, one can estimate the value of π (rejection technique, i.e., from a set of random numbers discard those that do not follow the desired distribution).

A typical problem arising in physics is to compute expressions like

$$\langle F \rangle = \frac{\sum_C F(C) \exp[-\beta E(C)]}{\sum_C \exp[-\beta E(C)]} \,, \tag{6.44}$$

which denote the expectation value of an observable F and the summation is over all configurations C of the configuration space. In general the configuration space is very large, much too large that one could do the summation explicitly.[4] But, most of the configurations typically give a vanishing contribution to the expectation value due to their small weight. MC technique now assumes that the expectation value can be approximated by evaluating F on a suitable set of independent "typical"

[4]As an example consider the Ising model on a 10^3 lattice, i.e., a cubic lattice with 10 sites in each direction. This model has $2^{1000} \approx 10^{300}$ configurations which is much more than even the fastest computer could have done in the age of the universe so far.

configurations $\{C_1, \ldots, C_N\}$ and taking the mean afterwards,

$$\langle F \rangle \approx \frac{1}{N} \sum_{i=1}^{N} F(C_i) \ .$$

The probability of the configuration C_i to be part of this set should be proportional to the corresponding Boltzmann weight $\exp[-\beta E(C_i)]$. Notice that the value of π in the children's game can be computed only because the area of the basic square is known. Otherwise, one is reduced to computing ratios of the kind (6.44).

The goal is now to construct a stochastic process, more precisely a Markov process,[5] whose stationary density coincides with a given density. For a physical system with Hamiltonian H this density is just given by

$$\rho = \frac{1}{Z} e^{-\beta H} \ ,$$

where Z denotes the partition function. One can show that this Markov process is realized when using transition rates $P(a \to b)$ satisfying the condition of *detailed balance*,

$$P(a \to b)\rho(a) = P(b \to a)\rho(b) \ ,$$

which is a sufficient though not necessary condition. Detailed balance is always fulfilled when using, e.g., the ansatz introduced by Metropolis *et al.* [100]

$$P(a \to b)dt = \begin{cases} e^{-\beta \Delta H} & : \quad \Delta H \geq 0 \\ 1 & : \quad \text{otherwise} \end{cases} = \min(1, e^{-\beta \Delta H}) = \min\left(1, \frac{\rho(b)}{\rho(a)}\right) .$$

Hence, rejections are the basic method by which MC enforces the correct density. If the jump leads to a smaller energy ($\Delta H < 0$), b is always accepted. If b has a larger energy, the acceptance of this state for the instant $t + dt$ becomes increasingly improbable the larger the energy difference is. The principle of *ergodicity*,

$$P(a \to \ldots \to b) > 0 \ \ \forall \ a, b$$

in combination with detailed balance insures that the simulation will converge to the correct probability density. Notice, that MC converges (probably) slowly, but surely (if implemented correctly)!

In order to simulate this stochastic process, computational effort can be drastically reduced by the fact [101] that the two steps

- check whether there should be a jump at all
- if yes, decide into which state

can be replaced by

- choose a possible state b
- check whether to jump into this state.

[5] That is a process with no "long-time-memory", i.e., the conditional probability depends only on the last point of the Markov chain, $P(x_n \leq x | x_{n-1}, \ldots, x_0) = P(x_n \leq x | x_{n-1})$.

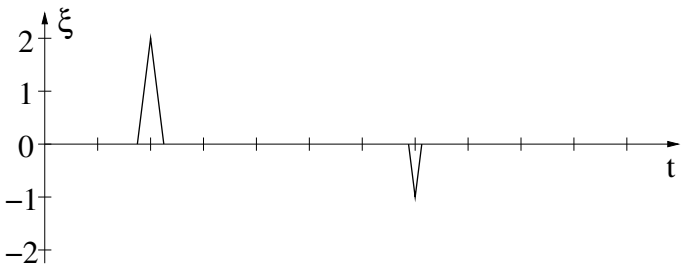

Figure 6.3: *MC moves of the kind (6.45) generate "kinks" at certain points in the configuration space.*

6.5.2 Simulation

Now, we aim to compute the current $I_B(t_k)$ according to (6.32). The QMC simulation then proceeds by generating a Metropolis trajectory according to the weight $W(\xi)$ defined as

$$W(\xi) = \left| \cos\left[\pi N^{(0)} \sum_{j,p} \frac{p\xi_{1jp}}{f} \right] \exp[-\Phi'] \prod_{j,p} G_p^{(f)}(\xi_{ajp}, z_{ajp}) \right| ,$$

with $s = \pm 1$ denoting the sign of this expression. The MC averaging is done using

$$I_B(t_k) = \frac{\langle sI_k \rangle}{\langle s \rangle} .$$

The sign problem manifests itself in a small average sign $\langle s \rangle$ for low temperatures and long real times $t_{\max}$. Since for intermediate-to-high temperatures, the regime $I_B(t) \propto t$ is reached quite fast, it is still possible to cover a large region of the relevant parameter space before the sign problem becomes overwhelming. The average sign in the data reported below was always larger than 10^{-3}. Note that one can obtain the full time-dependent function $I_B(t_k)$ in one MC run.[6]

The simplest MC moves that keep ergodicity are moves of $2f$ (randomly picked) "spins", see Fig. 6.3, according to

$$\begin{aligned} \xi_{ajp} &\rightarrow \xi'_{ajp} = \xi_{ajp} + \Delta_a , \\ \xi_{akp'} &\rightarrow \xi'_{akp'} = \xi_{akp'} - \Delta_a , \end{aligned} \tag{6.45}$$

with $|\Delta_a| = 1$ and $(j,p) \neq (k,p')$. Obviously, electroneutrality (6.24) is preserved by (6.45). Since these ("kink" generating) moves cost a huge energy they are quite rare, i.e., the corresponding acceptance ratio is very small. Nevertheless, they are important and necessary to ensure ergodicity.

[6] We point out that there is a rather subtle exclusion problem with the above formulation, completely analogous to the single-barrier scheme [95]. Fortunately, the resolution to this problem is possible in an identical manner as in Ref. [95], and we refer the reader to this work for details.

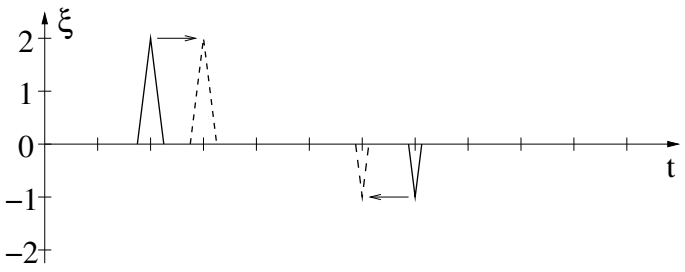

Figure 6.4: *MC moves of the kind (6.46) exchange neighboring "spins" and therefore move the "kinks" in configuration space.*

The second move that has to be considered is the "kink" moving one. Again, $2f$ randomly picked "spins" are changed (to keep electroneutrality),

$$\begin{aligned} \xi_{ajp} &\rightarrow \xi'_{ajp} = \xi_{ajp} + \bar{\Delta}_a = \xi_{akp'} \ , \\ \xi_{akp'} &\rightarrow \xi'_{akp'} = \xi_{akp'} - \bar{\Delta}_a = \xi_{ajp} \ , \end{aligned} \tag{6.46}$$

with $|\bar{\Delta}_a| = \xi_{akp'} - \xi_{ajp}$ and $k = j + 1$. Hence, neighboring "spins" are exchanged which is always possible (see Fig. 6.4).

In the remainder, we specialize to symmetric barriers, $V_+ = V_- = V$, and consider temperatures well below the single-particle level spacing, $\beta^{-1} \ll \Delta\epsilon$. The QMC approach will now be used to extract numerically exact data for the conductance of a double-barrier structure in a Luttinger liquid.

We now proceed to demonstrate that our QMC approach indeed reproduces (6.42), where $g = 1$ represents the most difficult case from a numerical point of view. Since the simulation method passes this check, where the sign problem is most pronounced, it can be trusted in as a reliable and accurate tool for $g < 1$. In Fig. 6.5, we show the output of characteristic QMC simulations for $I_B(t)$ in the conductance valley ($N^{(0)} = 0$) at $g = 1$. For sufficiently long times, this function has a well-defined linear slope which determines the conductance $G(N^{(0)}, \beta)$ via Eq. (6.25). We use a linear regression fit to obtain the slope and corresponding error bars. But one has to be careful, since the data can appear to be quite linear, however, at a certain t^* there is a bend and the slope changes. In this case it is necessary to check whether this bend has a physical origin or is just artificial, e.g., due to violations of ergodicity. Practically, when the bend occurs at t^* also for altered parameters $t_{\max}$ and P, we attribute a physical meaning to it. Otherwise, when only the last few points (independent of the special parameters) deviate from the linear behavior, we believe it to be an artificial effect.

Typically, at least 10^6 MC samples were accumulated to obtain $I_B(t)$ for a given parameter set. Trotter convergence was reached for discretizations $\Delta_t V \leq 0.1$. On a Xeon processor (2 GHz), our code performs at an average speed of about 10^5 samples per hour (for $P = 40$ time steps and $f = 1$). Error bars in the conductance

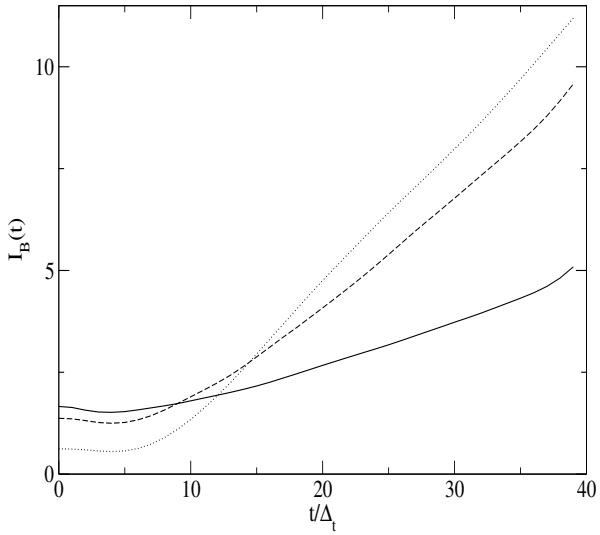

Figure 6.5: *QMC data for the time-dependent function $I_B(t)$ (see text) for $g = 1$, $N^{(0)} = 0$, $\beta = 40$, $\Delta\epsilon = \pi/2$, with $V = 0.05$ (solid curve), $V = 0.1$ (dashed curve) and $V = 0.2$ (dotted curve). Energies are in units of $\omega_c = 1$.*

$G(N^{(0)}, \beta)$ refer to both standard stochastic MC errors and to errors from fitting the long-time behavior by a linear slope.

We have extensively checked the QMC algorithm for $g = 1$ versus Eq. (6.42) at various temperatures and V, and found rather good agreement. Results for the conductance of spinless non-interacting electrons are shown in Fig. 6.6. Within error bars, the exact result (6.42) is indeed accurately reproduced. We note that $\beta\omega_c = 40$ is already close to the $T = 0$ limit where Eq. (6.43) applies, see Fig. 6.2. In a similar way, the validity of our approach has been established for $f = 2$.

6.5.3 Results for spinless interacting fermions

We now move on to explore the case of interacting fermions, $g < 1$, starting with the spinless case. We shall first discuss the limit of strong single-barrier transmission (small V), where Coulomb blockade and resonant tunneling are expected to be largely washed out. Then, we address the opposite limit with large barriers and rather weak tunneling. Finally, we briefly discuss the intermediate case.

General findings can be summarized as follows. With decreasing temperature the line width decreases and the valley conductance gets strongly suppressed. With increasing barrier strength V or stronger interaction (smaller g), these effects are further enhanced. For large level spacing on the dot ($\Delta\epsilon \gg k_B T_{\max}$), we are always in the coherent resonant tunneling (CRT) regime. For smaller level spacing ($\Delta\epsilon \gtrsim k_B T_{\max}$), we observe the *correlated* sequential tunneling (ST) regime as well as the crossover to CRT. From now on, all energies will be measured in units of $\omega_c = 1$. Data for $N^{(0)} > 1/2$ are obtained by symmetry from results for $N^{(0)} < 1/2$.

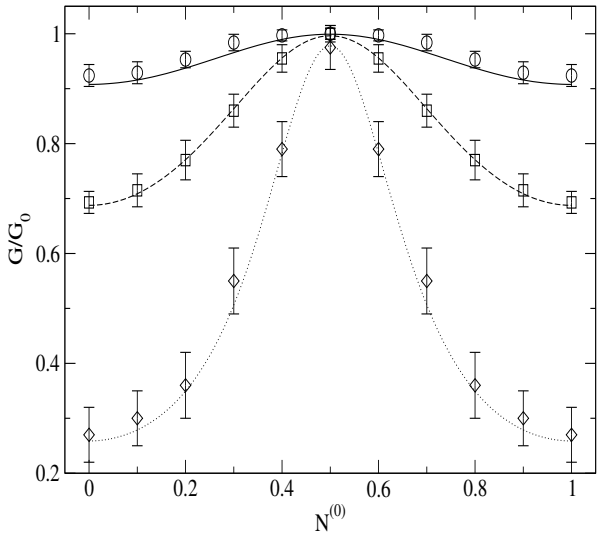

Figure 6.6: *Linear conductance in units of* $G_0 = e^2/h$ *versus* $N^{(0)}$ *for spinless fermions with* $g = 1$, $\Delta\epsilon = \pi/2$, *and* $\beta = 40$. *Single-barrier transmissions are (i)* $V = 0.05$ *(QMC data: circles, Eq. (6.42): solid curve), (ii)* $V = 0.1$ *(QMC data: squares, Eq. (6.42): dashed curve), and (iii)* $V = 0.2$ *(QMC data: diamonds, Eq. (6.42): dotted curve). Again,* $\omega_c = 1$ *and data for* $N^{(0)} > 1/2$ *are obtained by symmetry from results for* $N^{(0)} < 1/2$.

Strong single-barrier transmission

Let us start with the case of small barrier height, taking $V = 0.05$. Representative QMC data for $G(N^{(0)}, \beta)$ at $\beta = 40$ and different g are shown in Fig. 6.7. All conductance peak line shapes $G(N^{(0)})$ found in the temperature regime $\beta \leq 80$ can be fitted quite well by the $g = 1$ form (6.43) once the line shape parameter $w = w_g(\beta)$ is taken as a fit parameter, see Figs. 6.7 and 6.8. The temperature dependence of w as extracted from fits to QMC data shows power-law behavior, $w_{0.6} \sim T^{0.72}$ for $g = 0.6$, and $w_{0.3} \sim T^{0.84}$ for $g = 0.3$, see Fig. 6.8. Hence, with increasing interaction strength (smaller g), we find a renormalization of w to smaller values, corresponding to effectively stronger single barriers. This renormalization is in accordance with general expectations [37]. For $\beta > 80$, the line shape changes quantitatively and cannot any longer be fitted to (6.43). Then, the functional form is better described by

$$\frac{G(N^{(0)})}{G_0} = \frac{1}{\cosh^2[(N^{(0)} - 1/2)/w_g^*(\beta)]} \,, \tag{6.47}$$

which is similar to the Fermi liquid result (5.1). Near the peak, the line shape now is wider while the valley conductance is strongly suppressed. We checked for $g = 0.6$ and $80 \leq \beta \leq 200$ that w^* again shows power-law behavior, $w_{0.6}^* \sim T^{0.63}$, with roughly the same exponent as found for higher temperatures.

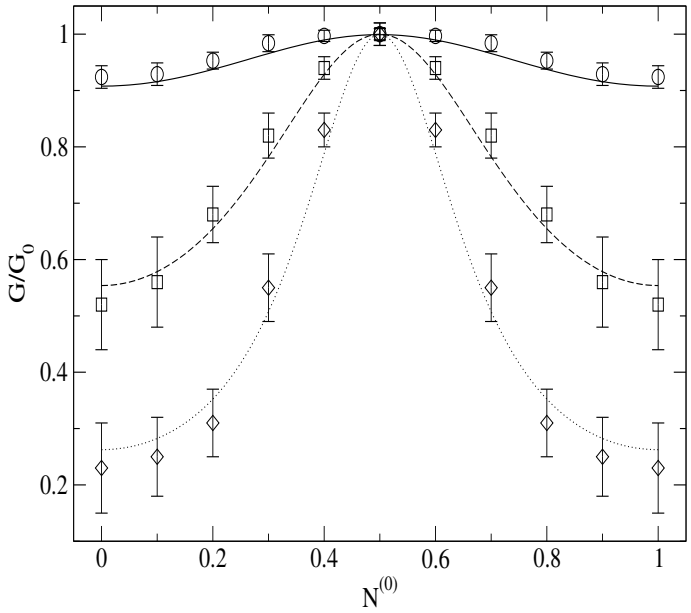

Figure 6.7: *Linear conductance versus $N^{(0)}$ for various g, $V = 0.05$, $\Delta\epsilon = \pi/2$, and $\beta = 40$. The best fit to Eq. (6.43) with w as only fit parameter gives the respective curves, see also Fig. 6.8. Data shown are for (i) $g = 1$ (QMC: circles, Eq. (6.42): solid curve), (ii) $g = 0.6$ (QMC: squares, fit: dashed curve), (iii) $g = 0.3$ (QMC: diamonds, fit: dotted curve).*

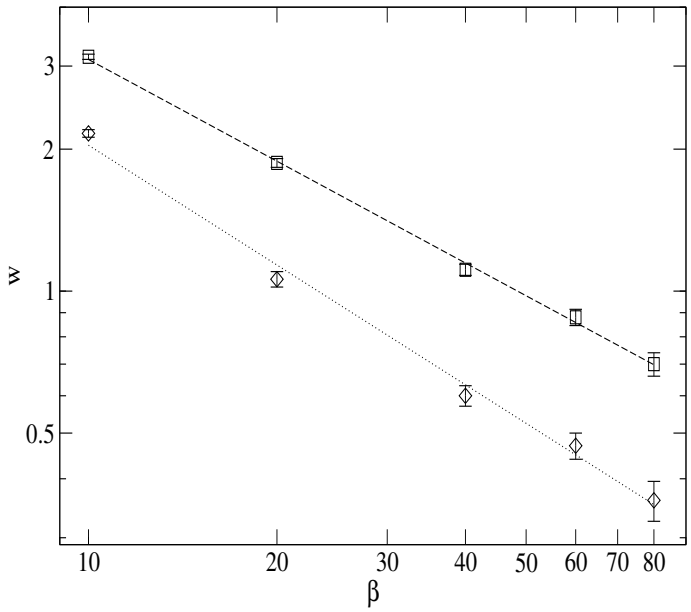

Figure 6.8: *Temperature dependence of the line shape fit parameter $w_g(\beta)$ for the parameters in Fig. 6.7. The dashed line shows a power-law fit for $g = 0.6$ (squares), $w_{0.6} \sim \beta^{-0.72}$, while the dotted line corresponds to $g = 0.3$ (diamonds), $w_{0.3} \sim \beta^{-0.84}$. Each data point here contains the information of a full line shape obtained by QMC. (Note the log-log scale of the plot.)*

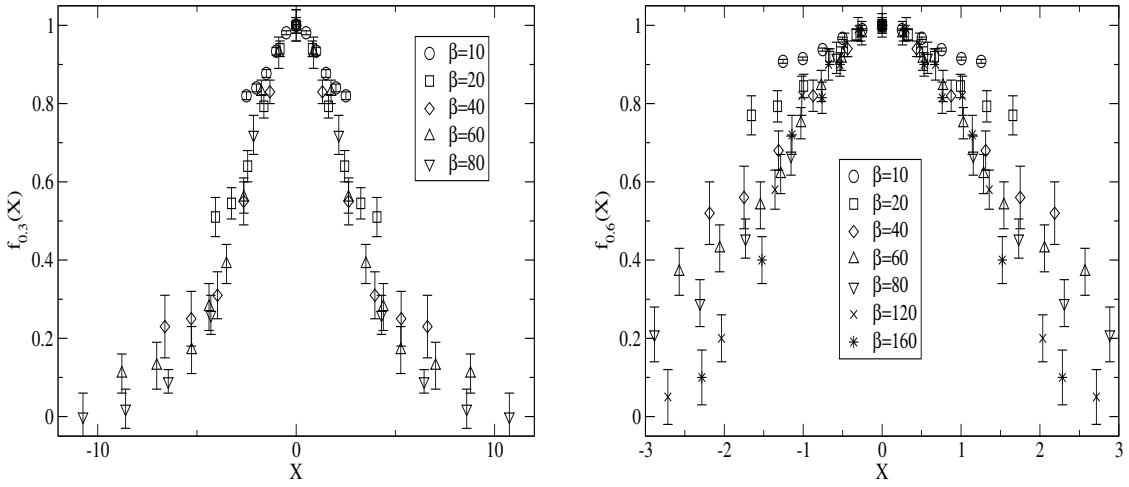

Figure 6.9: *Rescaled (according to (6.48)) QMC data for* $V = 0.05$, $\Delta\epsilon = \pi/2$, *and different temperatures (left:* $g = 0.3$, *right:* $g = 0.6$*). Within numerical accuracy, the data indeed collapse onto a single master curve. Only for the tails (conductance valley) there are deviations.*

When we rescale our QMC data for the line shape according to

$$N^{(0)} \to X(\beta) = \left(N^{(0)} - \frac{1}{2}\right) \beta^{1-g} \,, \tag{6.48}$$

see Eq. (5.2), all data points collapse onto a single universal master curve as expected for the CRT regime [37], see Fig. 6.9. As one can see, the tails, especially for high temperature and weak interaction, are too "fat" and lie above the master curve, which is given by the lower envelope function of the data. The observed power-law temperature dependence of w is, within the numerical accuracy of our data, also in accordance with the predicted behavior $w \sim T^{1-g}$.

We stress that the line shape is in general not Lorentzian but very well described by Eq. (6.43) or (6.47) with a renormalized w that has only a weak temperature dependence. The resonances become quite pronounced for strong interactions (small g). This sharpening of the peaks can be interpreted as the onset of Coulomb blockade. Despite the presence of strong quantum fluctuations of the charge on the dot, Coulomb blockade is still operative. It is obvious from Eq. (6.43) that in order to theoretically obtain such conductance peaks, it is necessary to perform a non-perturbative (in V) analysis, as is done here in a numerical way.

The line shape (6.43) closely resembles experimental results for strong-transmission (Fabry-Perot) Coulomb blockade oscillations in NTs [65, 92]. We therefore term this regime of very small barriers and/or high temperatures the *Fabry-Perot regime*. For $g < 1$, such Fabry-Perot oscillations include (strongly fluctuating) Coulomb blockade effects that are responsible for the narrowing of the resonance peak as temperature is lowered.

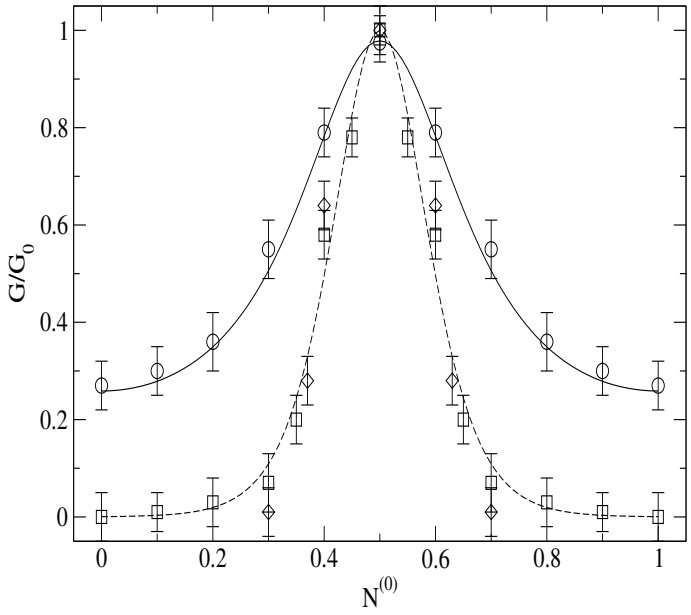

Figure 6.10: *Linear conductance versus* $N^{(0)}$ *for* $V = 0.2$*, taking* $g = 1$ *(circles),* $g = 0.6$ *(squares), and* $g = 0.3$ *(diamonds). Again,* $\Delta\epsilon = \pi/2$ *and* $\beta = 40$*. The solid line corresponds to the exact result (6.42) while the dashed line represents a fit for* $g = 0.6$ *to Eq. (6.47). The corresponding fit for* $g = 0.3$ *deviates only slightly from the one for* $g = 0.6$ *and is therefore not shown. While the data for* $g = 0.6$ *is quite well described by (6.47), for* $g = 0.3$ *the fit is not very good.*

At still lower temperatures, deviations from the Fabry-Perot line shape (6.43) can be seen. However, data can then be collapsed onto a universal curve, and the universal line shapes observed in this regime can be identified as CRT peaks [37]. Although resonant tunneling peaks are expected to survive only for $g > 1/2$, at least for strong barriers [76], we observe a perfectly pronounced resonance peak at $g = 0.3$. This finding is actually in accordance with renormalization group arguments for weak scatterers, and shows that the picture of CRT in a LL is actually very robust, covering also the low-temperature strong-transmission limit. Only for very weak barriers or high T, this picture is replaced by the Fabry-Perot regime discussed above.

Weak single-barrier transmission

The usual incoherent ST regime [76] should be realized for high barriers and essentially all temperatures for $g < 1/2$. Corresponding QMC data for $G(N^{(0)}, \beta)$ at $\beta = 40$ and $V = 0.2$ are shown in Fig. 6.10. A quantitative comparison to the sequential regime described by Eq. (5.3) is, however, not possible. Unfortunately, a further increase of V or decrease of T is getting appreciably more difficult due to a severe sign problem in the real-time QMC procedure.

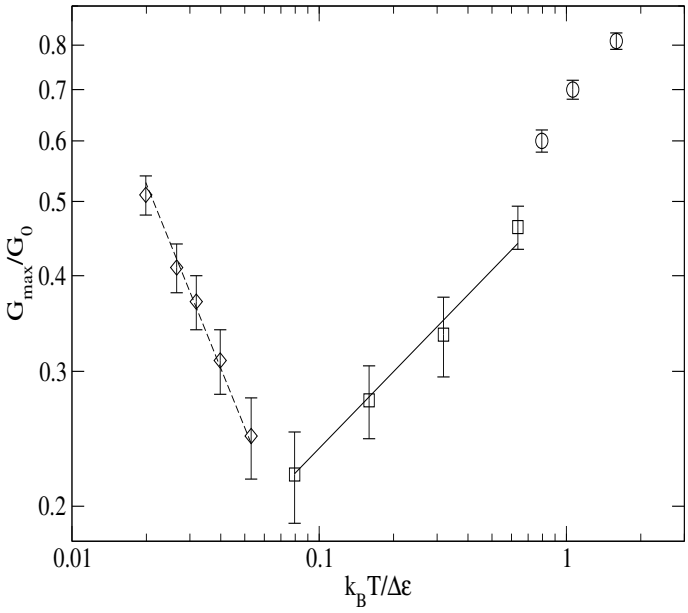

Figure 6.11: *Peak conductance versus temperature for $g = 0.6$, $V = 0.2$, and $\Delta\epsilon = \pi/20$. Notice the double-logarithmic scale of the plot. For high temperatures (corresponding QMC data: circles) one can observe deviations from the power-law behavior found in the correlated ST regime for intermediate T (solid line). The corresponding fit (incorporating QMC data denoted by squares) is to $G_{\max} \sim T^{1/3}$, see (6.49). For lower T (CRT regime), the increase of G is in accordance with (6.50), $G_{\max} \sim T^{-0.8}$ (dashed curve), taking into account the diamond shaped data points. The data shown here is in complete accordance with both theoretical predictions and experimental results, see also Fig. 5.7.*

For a larger dot (i.e. smaller level spacing $\Delta\epsilon$), we find the situation depicted in Fig. 6.11 where we show the behavior of the peak conductance $G_{\max}$ with temperature. Our findings are in accordance with both the theoretical predictions by Thorwart *et al.* [81] and the experimental results by Postma *et al.* [71], see also Fig. 5.7. Clearly visible is the regime of correlated ST with a power-law dependence of the peak conductance on temperature,

$$G_{\max} \sim T^{\eta} \quad \text{with} \quad \eta = 2\alpha_{\text{end}} - 1 = \frac{2}{g} - 3 \,, \tag{6.49}$$

and hence, $\eta = 1/3$ for $g = 0.6$ (incoherent ST predicts $\eta = -1/3$). For smaller temperature, there is a crossover to the CRT regime where the conductance again increases approaching the unitary limit for $T \to 0$. This increase is described by

$$G_{\max} \sim T^{2g-2} \,, \tag{6.50}$$

see [74]. The latter power law can easily be understood from the cumulant expansion of the effective scattering potential in the weak backscattering limit, see Sec. 6.2.1.

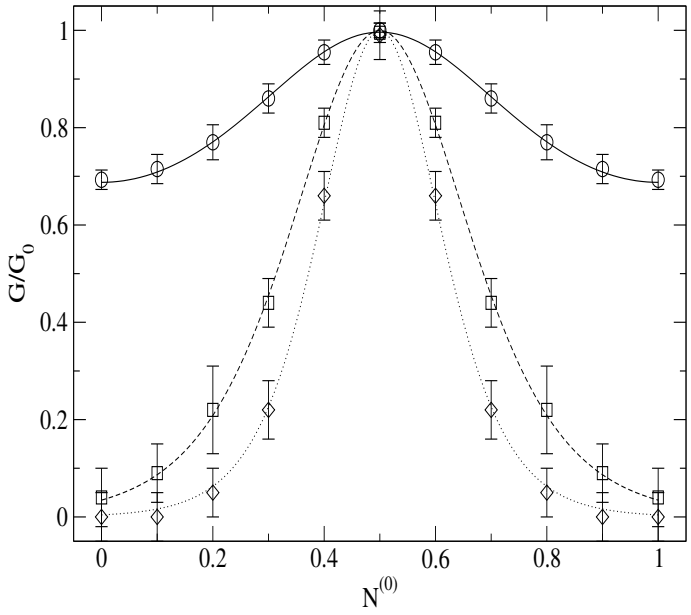

Figure 6.12: *Linear conductance versus $N^{(0)}$ for $V = 0.1$, $\Delta\epsilon = \pi/2$, and $\beta = 40$. Shown are QMC data for $g = 1$ (circles, solid line: Eq. (6.42)), $g = 0.6$ (squares), and $g = 0.3$ (diamonds). The dashed and dotted lines represent the corresponding fits to (6.47).*

Then, the island consisting of two impurities effectively corresponds to only a single impurity, and the second order term of the expansion, governing the leading behavior, readily leads to (6.50).

Intermediate transmission

Finally, we briefly discuss the case of intermediate transmission, taking $V = 0.1$. Corresponding QMC results for $\beta = 40$ are shown in Fig. 6.12, again for $g = 0.3$ and $g = 0.6$. Instead of being described by (6.43) as for $V = 0.05$, the line shape can now be fitted by (6.47). However, for lower temperature, the line shape also starts to deviate also from (6.47).

6.5.4 Results for the spinful case

Finally, we briefly consider the case of spinful interacting fermions, see Fig. 6.13. From the general resonance condition (6.11) we now expect peaks at $N^{(0)} =$ odd-integer values, in the absence of a magnetic field. This is indeed observed in the numerical data, and from the exact solution for $g_c = 1$ we expect these peaks to correspond to resonant tunneling peaks. Qualitatively, the resonance line shapes show the same behavior as in the spinless case, and therefore we show only data for $V = 0.2$ which now corresponds to intermediate transmission. Rescaling our QMC

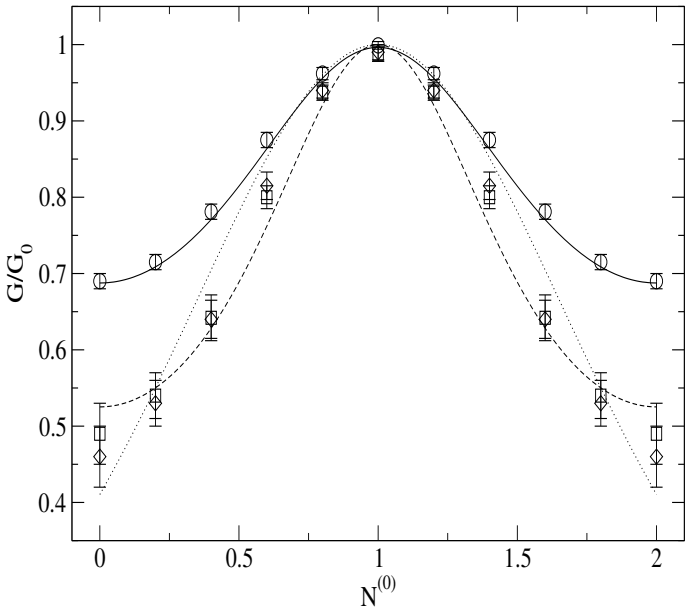

Figure 6.13: *Linear conductance versus $N^{(0)}$ (spinful case) for $V = 0.2$, $\beta = 40$, and $\Delta\epsilon = \pi/2$. Circles correspond to QMC data for $g_c = 1$ while squares and diamonds correspond to $g_c = 0.6$ and $g_c = 0.3$, respectively. The solid line represents the exact solution according to (6.42) while the dashed and dotted lines show a fit to (6.43) and (6.47), respectively. The fits are only shown for $g_c = 0.6$ since the corresponding curves for $g_c = 0.3$ deviate only slightly.*

data according to (6.48) with the changes necessary for the spinful case,

$$N^{(0)} \to X(\beta) = \left(N^{(0)} - 1\right) \beta^{\frac{1-g_c}{1+g_c}} ,$$

we again observe that the data collapse onto a single universal master curve (not shown), giving evidence for the CRT regime. Again, the line width scales as a power law in temperature with the exponent being in accordance with theoretical predictions [37], $w \sim T^{(1-g_c)/(1+g_c)}$. However, we did not find any sign of a Kondo effect in this setup.

6.5.5 Discussion

The strong-transmission regime is of direct experimental relevance [63, 65, 90, 92]. In particular, in Ref. [65], the Coulomb blockade oscillations of the conductance through a strongly contacted NT dot were observed (with normal metal leads). As a characteristic feature, pronounced dips in $G(N^{(0)})$ were found, which were interpreted as Fabry-Perot interference pattern within a Landauer-Büttiker picture of non-interacting electrons. To consistently explain the data, however, a rather

complicated fine-tuning of scattering processes involving the K point degeneracy in NTs seems necessary [65]. In our QMC calculations for strong transmission, we have never observed sharp conductance dips, neither for spinless nor for spinful fermions. Such dips are probably related to special impurity scattering processes [65] not contained in our model. However, our results closely resemble experimental data for strong-transmission resonances in NTs obtained by Park *et al.* [92].

In [37] the CRT regime was discussed, and a universal scaling behavior for the resonance curves with a power-law temperature dependence of the line width was predicted. This regime should be realized at low temperatures for $g > 1/4$ in the case of spinless fermions and not too strong barriers, or for $g > 1/2$ in both the strong-barrier limit for spinless fermions and the spinful case. As we showed, our QMC results are in good accordance with these predictions.

Let us now discuss our results in the light of the controversy described in the previous chapter. The incoherent ST regime [76] should be realized in the strong-barrier limit for not too low temperature. For $g < 1/2$ (spinless case), it should hold even down to $T = 0$, i.e., CRT should break down in this case. The predicted line shapes are rather sharp in this regime and the peak conductance should behave like $G_{\max} \sim T^{\alpha_{\mathrm{end}}-1}$. However, our QMC results do not give evidence for this scenario.

The correlated ST regime predicted in [81] is in accordance with the experimental results of [71]. Here, in contrast to the incoherent ST regime, a certain class of (but not all) diverging diagrams, i.e. the ones that cannot be divided into sub-diagrams (as assumed in the incoherent regime) due to correlations among the tunneling events on and off the dot, are included. There are no predictions for the line shape, but the peak conductance should show completely different behavior compared to the incoherent ST case, namely $G_{\max} \sim T^{2\alpha_{\mathrm{end}}-1}$. This temperature dependence is exactly what we found in our QMC data in the corresponding temperature regime where this mechanism should be operative.

Therefore, our findings are in agreement with the experimental results and also lend support to the correlated ST picture, but not to the incoherent ST regime. This indicates that corrections beyond the conventional incoherent ST mechanism are crucial in order to understand the experimental results of Ref. [71] and resolves the corresponding controversy. Compared to the theoretical model of [81], which relies on certain approximations, our analysis is more reliable since it is numerically exact.

6.6 Conclusions

We investigated resonant tunneling through a double-barrier structure in a SWNT. We presented a general theoretical model for a LL with two impurities containing the limit of spinless fermions as well as the spinful case and the SWNT. Within an effective model where the bulk degrees of freedom away from the location of

the two tunneling barriers have been integrated out, we determined the resonance condition analytically in both the weak- and strong-barrier limit by means of a cumulant expansion and a symmetry consideration, respectively. Further, we found a criterion for the stability of such resonances, depending on the interaction strength in the system.

In order to obtain the full line shape of the resonance for arbitrary single-barrier transmission, we developed a real-time (Keldysh) QMC approach on the basis of the Coulomb gas expansion for the propagator governing the dynamics of the system. Usually, a real-time QMC procedure suffers from a severe sign problem making it very difficult to obtain accurate data. However, in our approach we averaged over the classical fluctuations analytically, and only the quantum fluctuations are sampled by the QMC algorithm. This circumstance keeps the sign problem under control over a wide parameter range of interest. In particular, we paid attention to how the barrier strength influences the physical mechanisms of transport through the double barrier. To keep the number of free parameters manageable, we focused on the linear conductance for symmetric barriers, which is the most interesting and controversial regime.

The validity of our method was demonstrated for the non-interacting case by comparing numerical results to the exact solution (for arbitrary barrier height) which can be obtained via refermionization. We identified the regime of CRT where the line shape shows universal scaling behavior. When we rescaled our QMC data for different temperature, the single resonance curves indeed collapsed onto a universal master curve. We also found a power-law temperature dependence for the line width, with the exponents being in good agreement with theoretical predictions for this regime. Further, we identified the regime of correlated ST thereby resolving the recent controversy about this mechanism since we did not find any evidence for the incoherent ST regime. We could even observe the crossover from correlated ST to CRT. With spin, we identified resonant tunneling peaks, but no Kondo effect could be found in this setup.

Summary

Finally, we want to give a brief summary of the main results of our work which can be divided into two major parts. The first one addressed the behavior of van Hove singularities in the tunneling density of states of disordered multi-wall nanotubes. Having in mind the set-up of a typical scanning tunneling spectroscopy experiment for probing the tunneling density of states, we can assume that electron-electron interactions are screened off by a metallic substrate or a close-by gate and can therefore safely be neglected. In our discussion of the relevant disorder mechanisms we argued that scattering by a random scalar potential should be most important from an experimental point of view. In our model, the scattering potential is assumed to be random in space but constant in time, to have zero mean and a Gaussian white noise distribution for the fluctuations which corresponds to the assumption of point-like and isotropic scatterers. The resulting low-energy theory describing non-interacting disordered Dirac fermions on a cylinder is then solved within diagrammatic perturbation theory using standard Greens function formalism.

Since the breakdown of the Born approximation in the vicinity of a van Hove singularity makes the inclusion of all higher-order diagrams for the self energy mandatory, this problem is highly non-trivial. Focussing on potential scattering disorder, we have shown that a non-crossing approximation in combination with a self-consistent non-perturbative resummation of all diagrams for the self energy allows for an approximate but yet accurate solution of the problem which is valid over a wide parameter range. As a result, we obtained a closed analytical expression for the energy-dependent tunneling density of states which, for given radius of the nanotube, involves only one parameter, the disorder strength. The numerical solution of this expression then reveals remarkable differences between the bulk and boundary limits. While in the boundary limit van Hove singularities appear as square-root non-analyticities at the opening of new subbands with an only weak dependence on disorder, the bulk limit shows strongly broadened peaks that are shifted to smaller energies compared to the clean case. Further, above a certain disorder-dependent energy threshold, the bulk tunneling density of states behaves as a power law in energy, with an exponent depending on the disorder strength. From our results it is also apparent that it is in general not possible to define an energy-independent mean free path for all energies. We found our results to be in good qualitative agreement with experimental data, however, using available experimental technology it should be possible to unambiguously observe and test our predictions.

In the second part of our work, we investigated electronic transport through a quantum dot formed by two intramolecular buckles in a single-wall nanotube. This problem is equivalent to the one of resonant tunneling through a double-barrier structure in a Luttinger liquid which, in contrast to the single-impurity problem, is not integrable.

Within an effective model where the bulk degrees of freedom away from the location of the two tunneling barriers have been integrated out, we analytically determined the resonance condition, including a stability criterion depending on the interaction strength, both for the weak- and strong-barrier limit. Then, in order to obtain the full line shape of the resonance, a functional integral approach based on the Coulomb gas expansion for the propagator was developed. This procedure allows for a numerically exact (real-time) quantum Monte Carlo computation of the conductance through such a device. The line shape in the non-interacting limit was obtained analytically via refermionization and served as a test for the numerical results. In particular, we paid attention to how the barrier strength influences the physical transport mechanism through the device. For simplicity, we focused on the linear conductance considering only symmetric barriers at temperatures well below the level spacing on the dot which is also the most interesting and controversial regime.

We identified the regime of coherent resonant tunneling where the line shape shows universal scaling behavior, i.e., rescaled resonance curves for different temperature collapse onto a single master curve. In this regime, the line width shows power-law behavior on temperature with the exponent depending on the interaction strength in the system. We could also identify the regime of correlated sequential tunneling but did not find any evidence for the incoherent sequential tunneling regime. With our results, we resolve a recent controversy about this tunneling regime. Further, we also observed the crossover from correlated sequential tunneling to coherent resonant tunneling. With spin, we identified resonant tunneling peaks, but no Kondo effect could be found in this setup.

Appendix A

Iterative resummation approach

Now, we want to show explicitly that up to fourth order, our iterative approach of resumming the perturbation series contains the same diagrams with the correct combinatorial prefactors as the original perturbation series. In principle, one can check this, of course, for all orders, but the calculation is very tedious, already in the fifth order. However, from our analysis we are confident that all higher-order terms are also reproduced correctly. To avoid lengthy expressions, we will use the following abbreviation,

$$\mathrm{Tr}G_0 \equiv \mathrm{Tr}_{\vec{k},\sigma} G_0(E,\vec{k}) \; .$$

To find the diagrams contributing to the self energy, we have to remember the definition as explained in Sec. 2.4. If we are interested in the diagrams up to fourth order in Δ_V, we simply have to consider all propagators with up to eight scattering lines (only the ones with an even number of scattering lines will contribute). Since ensemble-averaging results in tying together scattering lines in pairs (we will only consider the non-crossing diagrams) we just have to draw pictures with all possible combinations. Per definition, only the irreducible diagrams contribute to the self energy, and the result of this procedure is shown in Fig. A.1. It is easy to write down the corresponding expressions in terms of the free propagator G_0,

$$\begin{aligned}
\Sigma_4 &= \Delta_V \mathrm{Tr}G_0 + \Delta_V^2 \mathrm{Tr}G_0^2 \mathrm{Tr}G_0 + \Delta_V^3 (\mathrm{Tr}G_0^2)^2 \mathrm{Tr}G_0 + \Delta_V^3 \mathrm{Tr}G_0^3 (\mathrm{Tr}G_0)^2 \\
&+ \Delta_V^4 (\mathrm{Tr}G_0^2)^3 \mathrm{Tr}G_0 + \Delta_V^4 \mathrm{Tr}G_0^2 \mathrm{Tr}G_0^3 (\mathrm{Tr}G_0)^2 \\
&+ \Delta_V^4 \mathrm{Tr}G_0^3 \mathrm{Tr}G_0^2 (\mathrm{Tr}G_0)^2 + \Delta_V^4 \mathrm{Tr}G_0^3 \mathrm{Tr}G_0^2 (\mathrm{Tr}G_0)^2 \\
&+ \Delta_V^4 \mathrm{Tr}G_0^4 (\mathrm{Tr}G_0)^3 \; , \qquad \text{(A.1)}
\end{aligned}$$

which is done in the same order as the diagrams appear in the figure. Here, with Σ_4 we denote the sum of all self energy diagrams up to fourth order in Δ_V. As one can see, the sixth, seventh, and eighth diagram correspond to the same term in the perturbation series. Accordingly, we can replace these three diagrams by one of them with a combinatorial prefactor of three.

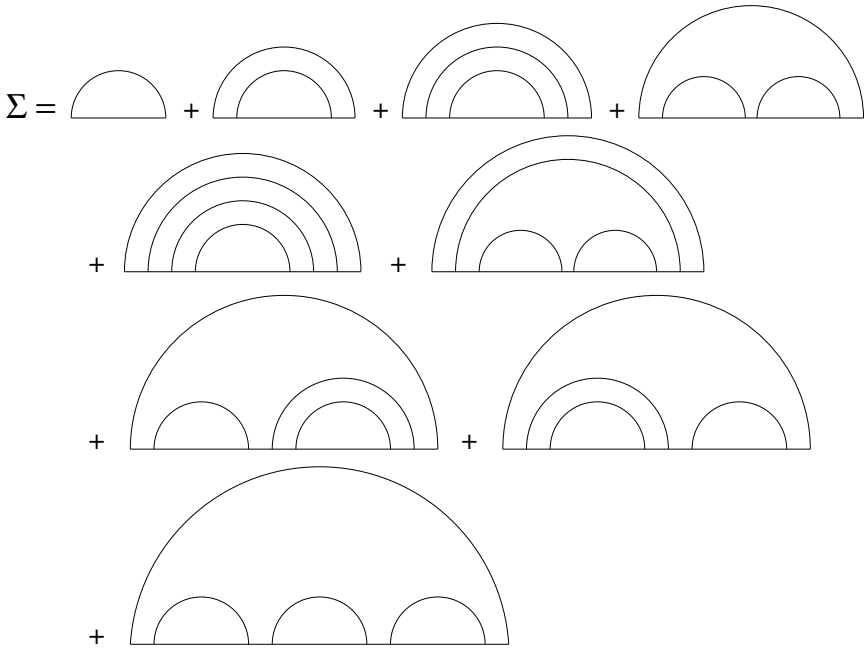

Figure A.1: *Self energy diagrams up to fourth order in* Δ_V.

Now, we turn to the iterative approach used in Sec. 3.4. From Eqs. (3.16) and (3.17) we find

$$\Sigma_N = \Delta_V \mathrm{Tr} \frac{1}{G_0^{-1} - \Delta_V \mathrm{Tr} G_{N-2}} \ ,$$

which can be expanded in Δ_V,

$$\Sigma_N = \sum_{j=1}^{N} \Delta_V^j \mathrm{Tr} G_0^j \left(\mathrm{Tr} G_{N-2}\right)^{j-1} \ . \tag{A.2}$$

To be consistent, Σ_N should not contain diagrams that are higher than Nth order in Δ_V. Therefore, we also have to expand G_{N-2} up to $(N-2)$th order,

$$G_{N-2} = \frac{1}{G_0^{-1} - \Delta_V \mathrm{Tr} G_{N-3}} = \sum_{k=0}^{N-2} \Delta_V^k G_0^{k+1} \left(\mathrm{Tr} G_{N-3}\right)^k + \dots \ .$$

This formula has to be iterated $N-3$ times, until it only contains the free propagator G_0,

$$\begin{aligned} G_{N-2} \ = \ & \sum_{k_1=0}^{N-2} \Delta_V^{k_1} G_0^{k_1+1} \left[\sum_{k_2=0}^{N-3} \Delta_V^{k_2} \mathrm{Tr} G_0^{k_2+1} \Big(\dots \right. \\ & \left. \dots \left\{ \sum_{k_{N-2}=0}^{1} \Delta_V^{k_{N-2}} \mathrm{Tr} G_0^{k_{N-2}+1} (\mathrm{Tr} G_0)^{k_{N-2}} \right\}^{k_{N-3}} \dots \Big)^{k_2} \right]^{k_1} + \dots \ . \end{aligned} \tag{A.3}$$

Note that not all possible terms in (A.3) have to be considered since there is the additional constraint

$$\sum_{i=1}^{N-2} k_i \leq N-2 \; ,$$

that ensures the consistency with respect to the order in Δ_V.

Now, we apply the general formulas (A.2) and (A.3) to the special case of $N = 4$. From Eq. (A.2) we obtain

$$\Sigma_4 = \Delta_V \mathrm{Tr} G_0 + \Delta_V^2 \mathrm{Tr} G_0^2 \mathrm{Tr} G_2 + \Delta_V^3 \mathrm{Tr} G_0^3 (\mathrm{Tr} G_2)^2 + \Delta_V^4 \mathrm{Tr} G_0^4 (\mathrm{Tr} G_2)^3 \; , \qquad \text{(A.4)}$$

where we have to replace G_2 by its expansion due to Eq. (A.3),

$$G_2 = \sum_{k=0}^{2} \Delta_V^k G_0^{k+1} \left(\sum_{l=0}^{1} \Delta_V^l \mathrm{Tr} G_0^{l+1} (\mathrm{Tr} G_0)^l \right)^k + \ldots \; .$$

Therefore, we explicitly have

$$\mathrm{Tr} G_2 = \mathrm{Tr} G_0 + \Delta_V \mathrm{Tr} G_0^2 \mathrm{Tr} G_0 + \Delta_V^2 (\mathrm{Tr} G_0^2)^2 \mathrm{Tr} G_0 + \Delta_V^2 \mathrm{Tr} G_0^3 (\mathrm{Tr} G_0)^2 + \ldots \; ,$$

which has to be inserted into (A.4). To be consistent in the order of Δ_V, we only need to consider

$$(\mathrm{Tr} G_4)^2 = (\mathrm{Tr} G_0)^2 + 2\Delta_V \mathrm{Tr} G_0^2 (\mathrm{Tr} G_0)^2 + \ldots \; ,$$

and

$$(\mathrm{Tr} G_4)^3 = (\mathrm{Tr} G_0)^3 + \ldots \; .$$

Finally, we have

$$\begin{aligned} \Sigma_4 \;\; &= \;\; \Delta_V \mathrm{Tr} G_0 \\ &+ \;\; \Delta_V^2 \mathrm{Tr} G_0^2 \mathrm{Tr} G_0 + \Delta_V^3 (\mathrm{Tr} G_0^2)^2 \mathrm{Tr} G_0 + \Delta_V^4 (\mathrm{Tr} G_0^2)^3 \mathrm{Tr} G_0 + \Delta_V^4 \mathrm{Tr} G_0^2 \mathrm{Tr} G_0^3 (\mathrm{Tr} G_0)^2 \\ &+ \;\; \Delta_V^3 \mathrm{Tr} G_0^3 (\mathrm{Tr} G_0)^2 + 2\Delta_V^4 \mathrm{Tr} G_0^3 \mathrm{Tr} G_0^2 (\mathrm{Tr} G_0)^2 \\ &+ \;\; \Delta_V^4 \mathrm{Tr} G_0^4 (\mathrm{Tr} G_0)^3 \; , \end{aligned} \qquad \text{(A.5)}$$

which is exactly the same as Eq. (A.1).

Appendix B

Non-crossing approximation

In this appendix we will explain in detail how to obtain the results (3.22) and (3.23) which are essential for the justification of the NCA. For the case of Schrödinger fermions we define $E_n = \omega_n^2/2m$, and hence, the dispersion relation reads $E(\vec{k}) = k^2/2m + E_n$. Using this and inserting the Greens function (3.21) in Eq. (3.20) we have

$$\Sigma_c^{(2)}(E,\vec{k}_0) = \Delta_V^2 \sum_{n,n'} \int \frac{dk}{2\pi}\frac{dk'}{2\pi} \left\{ \frac{1}{E - E_n - \Sigma(E) - k^2/2m} \right.$$
$$\left. \times \quad \frac{1}{E - E_{n+n'} - \Sigma(E) - (k+k')^2/2m} \; \frac{1}{E - E_{n_0+n'} - \Sigma(E) - (k_0+k')^2/2m} \right\} .$$

Now, we see that the dominant contribution comes from momenta with $|\vec{k}| \approx |\vec{k}_0| \approx |\vec{k} + \vec{k}'| \approx |\vec{k}_0 + \vec{k}'| = E/v_F$ and therefore, only $k' \approx 0$ and $n' = 0$ survives. Accordingly, we neglect terms $\sim k'^2$ and keep only $n' = 0$,

$$\begin{aligned} \Sigma_c^{(2)}(E,\vec{k}_0) \;\; &\approx \;\; \left(\frac{\Delta_V}{2\pi}\right)^2 \sum_n \int dk \frac{1}{E - E_n - \Sigma(E) - k^2/2m} \\ &\times \;\; \underbrace{\int dk' \frac{1}{E - E(\vec{k}) - \Sigma(E) - kk'/m} \; \frac{1}{E - E(\vec{k}_0) - \Sigma(E) - k_0 k'/m}}_{=I} . \end{aligned} \tag{B.1}$$

The integral I is now written as

$$I = \int dk' \frac{m/k}{k' - \frac{m}{k}\left(E - E(\vec{k}) - \Sigma(E)\right)} \; \frac{m/k_0}{k' - \frac{m}{k_0}\left(E - E(\vec{k}_0) - \Sigma(E)\right)} ,$$

and can be done by contour integration. Depending on the sign of k and k_0, both poles are in the same or in different half-planes. When both poles are in the same half-plane (k and k_0 have the same sign), then the integral vanishes. This can be accomplished by a factor $\Theta(-k_0 k)$ in the result. In doing so we can assume, without loss of generality, that k and k_0 have different signs. We then close the contour in the upper half-plane and, as one can easily check, when we have $k_0 < 0$

instead of $k_0 > 0$ the result only changes its sign. This can be taken into account by a factor $\mathrm{sgn}(k_0)$ in the final result. Thus, we can assume that $k_0 > 0$ and $k < 0$. Since $\mathrm{Im}\Sigma(E) = -\pi\Delta_V\nu(E) < 0$, see Eq. (3.19), we pick up the pole at $k' = m(E - E(\vec{k}_0) - \Sigma(E))/k_0$ and therefore, the final result is

$$I = 2\pi i\, m\, \Theta(-k_0 k)\mathrm{sgn}(k_0)\frac{1}{k\left(E - E(\vec{k}_0) - \Sigma(E)\right) - k_0\left(E - E(\vec{k}) - \Sigma(E)\right)}\ , \tag{B.2}$$

which, after inserting it in (B.1), precisely gives Eq. (3.22).

Since we want to estimate the contribution $\delta\nu$ of $\Sigma_c^{(2)}$ to the TDOS we have to add external propagators $\bar{G}(\vec{k}_0)$. Due to the external pole we then have $E - E(\vec{k}_0) - \Sigma(E) \approx 0$ and hence, inserting (B.2) in (B.1) we have

$$\begin{aligned}\Sigma_c^{(2)}(E,\vec{k}_0) &\approx -i\frac{\Delta_V^2}{2\pi}\frac{m}{k_0}\mathrm{sgn}(k_0)\sum_n\int dk\frac{\Theta(-k_0k)}{E - E(\vec{k}) - \Sigma(E)} \\ &\approx i\frac{\Delta_V^2}{2\pi}\underbrace{\frac{m}{|k_0|}}_{\approx 1/v_F}\sum_n\partial_E\int dk\bar{G}(E,\vec{k})\Theta(-k_0k)\ .\end{aligned}$$

Since $\delta\nu$ depends only on $|k_0|$ we can assume, without loss of generality, that $k_0 > 0$. Then,

$$\int_{-\infty}^{\infty} dk\Theta(-kk_0) = \int_{-\infty}^{0} dk = \frac{1}{2}\int_{-\infty}^{\infty} dk\ ,$$

where the last equality holds since $\bar{G}(E,\vec{k}) = \bar{G}(E,|k|,\omega_n)$. Finally, we end up with

$$\Sigma_c^{(2)}(E,\vec{k}_0) \approx i\frac{\Delta_V}{2v_F}\partial_E\underbrace{\Delta_V\mathrm{Tr}_{\vec{k}}\bar{G}(E,\vec{k})}_{=\Sigma(E)} = \frac{i\Delta_V}{2v_F}\partial_E\Sigma(E)\ ,$$

which is exactly Eq. (3.23).

Appendix C

Effective action

We now explicitly integrate out the bulk modes $\theta_a(x)$ in the action (6.1) away from the location $x = \pm d/2$ of the two tunneling barriers which can be done exactly by introducing Lagrange multipliers $\lambda_{ap}(\tau)$ to enforce (6.3), i.e., we have to add a term

$$S_{\rm Lagr} = i \sum_{a,p} \int_0^\beta d\tau \lambda_{ap}(\tau) \left\{ q_{ap}(\tau) - \sqrt{\frac{4\pi}{f}} \theta_a(pd/2,\tau) \right\} \tag{C.1}$$

to the action (6.1). The next step is to solve the resulting Euler-Lagrange equations,

$$(\partial_\tau^2 + v_a^2 \partial_x^2)\theta_a(x,\tau) = -i v_F \sqrt{\frac{4\pi}{f}} \sum_p \lambda_{ap}(\tau) \delta(x - pd/2) \ ,$$

which is easily done in Fourier space leading to

$$\tilde{\theta}_a(k,\omega_n) = i v_F \sqrt{\frac{4\pi}{f}} \sum_p \tilde{\lambda}_{ap}(\omega_n) \frac{e^{-ipkd/2}}{\omega_n^2 + v_a^2 k^2} \ . \tag{C.2}$$

In order to eliminate the Lagrange multipliers we have to minimize the total action $S + S_{\rm Lagr}$. Therefore, we introduce the boson propagators[1]

$$F_a(x,\omega_n) = \frac{v_F}{2} \int_{-\infty}^{\infty} dk \frac{e^{ikx}}{\omega_n^2 + v_a^2 k^2} = \frac{\pi g_a}{2|\omega_n|} e^{-|x\omega_n|/v_a} \ .$$

Taking the action $S + S_{\rm Lagr}$ as given by (6.1) and (C.1), using Eqs. (6.3) and (C.2) then gives

$$\begin{aligned} S &= -\frac{2}{\beta f} \sum_{a,n,p,p'} \tilde{\lambda}_{ap}(\omega_n) \tilde{\lambda}^*_{ap'}(\omega_n) F_a([p-p']d/2,\omega_n) \\ &+ \frac{2\pi i}{\beta f} \sum_{a,n,p} \tilde{\lambda}_{ap}(-\omega_n) \left\{ \tilde{Q}_a(\omega_n) + \frac{p}{2} \tilde{N}_a(\omega_n) \right\} + S_{\rm imp} \ . \end{aligned} \tag{C.3}$$

[1]The integrand has two poles, $k = \pm i|\omega_n|/v_a$, and the integration can be done by closing the contour, e.g., in the upper half-plane.

Integration over Lagrange multipliers amounts to solving

$$\frac{2\pi i}{\beta f}\left\{\tilde{Q}_a(\omega_n)+\frac{p}{2}\tilde{N}_a(\omega_n)\right\}-\frac{4}{\beta f}\sum_{p'}F_a([p-p']d/2,\omega_n)\tilde{\lambda}_{ap'}(\omega_n)=0\ .$$

Equivalently, this can be written in matrix form and the solution is readily obtained,

$$\begin{aligned}\begin{pmatrix}\tilde{\lambda}_{a+}\\ \tilde{\lambda}_{a-}\end{pmatrix}(\omega_n) &= \frac{i\pi}{2F_a(\omega_n)}\frac{1}{1-e^{-2|\omega_n|/\omega_a}}\\ &\times \begin{pmatrix}1 & e^{-|\omega_n|/\omega_a}\\ -e^{-|\omega_n|/\omega_a} & 1\end{pmatrix}\begin{pmatrix}\tilde{Q}_a(\omega_n)+\tilde{N}_a(\omega_n)/2\\ \tilde{Q}_a(\omega_n)-\tilde{N}_a(\omega_n)/2\end{pmatrix},\end{aligned}$$

where we have introduced $\omega_a = v_a/d$. Inserting this result in (C.3) gives, after several but simple algebraic manipulations, the effective action (6.6),

$$S_{\text{eff}}[Q_a,N_a]=\sum_{a,n\neq 0}\frac{\pi|\omega_n|}{2f\beta g_a}\left\{\frac{4|\tilde{Q}_a(\omega_n)|^2}{1+e^{-|\omega_n|/\omega_a}}+\frac{|\tilde{N}_a(\omega_n)|^2}{1-e^{-|\omega_n|/\omega_a}}\right\}+\int_0^\beta d\tau V_{\text{eff}}[Q_a(\tau),N_a(\tau)]\ .$$

Appendix D

Cumulant expansion

Now, we explicitly compute the first and second order of the cumulant expansion of (6.8) for symmetric barriers as well as the scaling dimension of the operators generated in second order of the expansion.

First order

We start with considering the first order, $V^{(1)} = \langle V_{\rm imp}\rangle_N$, and write the sine and cosine terms of $V_{\rm imp}$ as exponential functions,

$$\begin{aligned} V^{(1)} &= V\sum_p \left\langle \prod_a \left\{ \frac{1}{2}\sum_{\{\sigma_a\}=\pm} \exp\left[i\sigma_a \frac{2\pi}{f}\left(Q_a + \frac{p}{2}N_a\right)\right]\right\} \right. \\ &+ \left. \delta_{f4}\prod_a \left\{ \frac{1}{2i}\sum_{\{\sigma_a\}=\pm} \sigma_a \exp\left[i\sigma_a \frac{2\pi}{f}\left(Q_a + \frac{p}{2}N_a\right)\right]\right\} \right\rangle_N . \end{aligned}$$

Using $\delta_{f4}\prod_a \frac{1}{i} = 1$ and $N_a = N_a^{(0)} + \delta N_a$ we have

$$\begin{aligned} V^{(1)} &= \frac{V}{2^{f-1}} \exp\left[-\frac{\pi^2}{2f^2}\sum_a \langle \delta N_a^2\rangle_N \right] \sum_{\{\sigma_a\}=\pm} \exp\left[i\frac{2\pi}{f}\sum_a \sigma_a Q_a\right] \\ &\times \cos\left[\frac{\pi}{f}\sum_a \sigma_a N_a^{(0)}\right]\left(1 + \delta_{f4}\prod_a \sigma_a\right). \end{aligned} \tag{D.1}$$

When we use

$$\begin{aligned} \sum_{\{\sigma_a\}=\pm} \exp\left[\sum_a \sigma_a Q_a\right] &= \sum_{\{\sigma_a\}=\pm} \left\{ \cos\left[\sum_a \sigma_a Q_a\right] + i\sin\left[\sum_a \sigma_a Q_a\right]\right\} \\ &= \sum_{\{\sigma_a\}=\pm} \cos\left[\sum_a \sigma_a Q_a\right], \end{aligned}$$

which holds since $\sin(-x) = -\sin(x)$, we readily obtain Eq. (6.9),

$$\begin{aligned} V^{(1)} &= \frac{V}{2^{f-1}} \exp\left[-\frac{\pi^2}{2f^2}\sum_a \langle \delta N_a^2\rangle_N \right] \sum_{\{\sigma_a\}=\pm} \cos\left[\frac{2\pi}{f}\sum_a \sigma_a Q_a\right] \\ &\times \cos\left[\frac{\pi}{f}\sum_a \sigma_a N_a^{(0)}\right]\left(1 + \delta_{f4}\prod_a \sigma_a\right). \end{aligned}$$

Second order

In order to compute the second order,

$$V^{(2)} = \frac{1}{2}\left(\langle V_{\rm imp}^2\rangle_N - \langle V_{\rm imp}\rangle_N^2\right),$$

we first look at $\langle V_{\rm imp}^2\rangle_N$. Again, we use exponential functions instead of the trigonometric ones and obtain

$$\begin{aligned}\langle V_{\rm imp}^2\rangle_N = \frac{V^2}{2^{2f}} \sum_{p,p',\{\sigma_a,\sigma_a'\}} \prod_a \exp\left[i\frac{2\pi}{f}(\sigma_a+\sigma_a')Q_a\right] \exp\left[i\frac{\pi}{f}(p\sigma_a+p'\sigma_a')N_a^{(0)}\right] \\ \times \quad \exp\left[-\frac{\pi^2}{2f^2}(p\sigma_a+p'\sigma_a')^2\langle\delta N_a^2\rangle_N\right]\left(1+\delta_{f4}\prod_a\sigma_a\right)\left(1+\delta_{f4}\prod_a\sigma_a'\right).\end{aligned}$$

The other term, $\langle V_{\rm imp}\rangle_N^2$, is simply the square of the first order term (D.1),

$$\begin{aligned}\langle V_{\rm imp}\rangle_N^2 &= \frac{V^2}{2^{2f}} \sum_{p,p',\{\sigma_a,\sigma_a'\}} \prod_a \exp\left[i\frac{2\pi}{f}(\sigma_a+\sigma_a')Q_a\right] \exp\left[i\frac{\pi}{f}(p\sigma_a+p'\sigma_a')N_a^{(0)}\right] \\ &\times \quad \exp\left[-\frac{\pi^2}{f^2}\langle\delta N_a^2\rangle_N\right]\left(1+\delta_{f4}\prod_a\sigma_a\right)\left(1+\delta_{f4}\prod_a\sigma_a'\right).\end{aligned}$$

Together, we then have

$$\begin{aligned}V^{(2)} &= \frac{V^2}{2^{2f+1}} \sum_{p,p',\{\sigma_a,\sigma_a'\}} \prod_a \exp\left[i\frac{2\pi}{f}(\sigma_a+\sigma_a')Q_a\right] \exp\left[i\frac{\pi}{f}(p\sigma_a+p'\sigma_a')N_a^{(0)}\right] \\ &\times \quad \left(\exp\left[-\frac{\pi^2}{2f^2}(p\sigma_a+p'\sigma_a')^2\langle\delta N_a^2\rangle_N\right] - \exp\left[-\frac{\pi^2}{f^2}\langle\delta N_a^2\rangle_N\right]\right) \\ &\times \quad \left(1+\delta_{f4}\prod_a\sigma_a\right)\left(1+\delta_{f4}\prod_a\sigma_a'\right),\end{aligned}$$

which is precisely Eq. (6.12).

Scaling dimension

In order to determine the relevancy of the operators generated in the second order of the cumulant expansion, we have to compute the scaling dimension of the operator

$$\hat{O} = \prod_a \exp\left[i\frac{2\pi}{f}(\sigma_a+\sigma_a')Q_a\right]. \tag{D.2}$$

Therefore, we first look at $\langle Q_a(\tau)Q_a(0)\rangle$, where the expectation value has to be taken with respect to the (Gaussian) action

$$S'[Q_a] = \sum_{a,n\neq 0} \frac{\pi|\omega_n|}{2f\beta g_a} \frac{4|\tilde{Q}_a(\omega_n)|^2}{1+e^{-|\omega_n|/\omega_a}}.$$

One can immediately read off

$$\langle \tilde{Q}_a(\omega_n)\tilde{Q}_a^*(\omega_{n'})\rangle = \frac{\beta f g_a}{4\pi|\omega_n|}\left(1+e^{-|\omega_n|/\omega_a}\right)\delta_{nn'} \ ,$$

which has to be Fourier-transformed to give

$$\langle Q_a(\tau)Q_a(0)\rangle = \frac{1}{\beta}\sum_n \frac{f g_a}{4\pi|\omega_n|}\left(1+e^{-|\omega_n|/\omega_a}\right)e^{i\omega_n\tau} \ .$$

The dominant contribution comes from small frequencies and hence, taking the continuum limit, $\sum_n \to \frac{\beta}{2\pi}\int d\omega$, gives

$$\langle Q_a(\tau)Q_a(0)\rangle = \frac{f g_a}{2\pi^2}\ln|\tau| \ . \tag{D.3}$$

Therefore,

$$\begin{aligned}\langle \hat{O}(\tau)\hat{O}(0)\rangle &\overset{(D.2)}{\sim} \exp\left[-\frac{4\pi^2}{f^2}\sum_a(\sigma_a+\sigma_a')^2\langle Q_a(\tau)Q_a(0)\rangle\right] \\ &\overset{(D.3)}{\sim} \exp\left[-\frac{2}{f}\sum_a(\sigma_a+\sigma_a')^2 g_a\ln|\tau|\right],\end{aligned}$$

and we can simply read off the scaling dimension (6.14),

$$\Delta = \frac{1}{f}\sum_a(\sigma_a+\sigma_a')^2 g_a = \frac{2}{f}\sum_a(1+\sigma_a\sigma_a')g_a \ ,$$

where the last equality holds since $\sigma_a, \sigma_a' = \pm 1$.

Appendix E

Coulomb gas path integral

In this appendix, we provide various intermediate steps of the computation done in Sec. 6.3. In particular, these are the Coulomb gas expansion, the Gaussian average over Q_a, N_a degrees of freedom, and the computation of the diagonal matrix elements for the influence functional.

Coulomb gas expansion

Starting from

$$\exp[iS_{\rm imp}] = \prod_{j,p} \exp\left[-i\Delta_t V_p \left\{\prod_a \cos\left[\sqrt{\frac{4\pi}{f}}\theta_{aj}(pd/2)\right] - \prod_a \cos\left[\sqrt{\frac{4\pi}{f}}\theta'_{aj}(pd/2)\right]\right\}\right],$$

we first consider only one term and write the cosine in terms of exponential functions,

$$\begin{aligned}\exp[i\gamma_{jp}] &\equiv \exp\left[-i\Delta_t V_p \prod_a \cos\left[\sqrt{\frac{4\pi}{f}}\theta_{aj}(pd/2)\right]\right] \\ &= \sum_{\nu=0}^{\infty}\frac{1}{\nu!}\left(-i\Delta_t V_p \prod_a \frac{1}{2}\sum_{\sigma_{ajp}=\pm} e^{i\sigma_{ajp}\sqrt{4\pi/f}\theta_{aj}(pd/2)}\right)^{\nu},\end{aligned}$$

where we have introduced so-called "Coulomb charges" σ_{ajp}. Expanding up to second order in $\Delta_t V_p$ gives

$$\begin{aligned}\exp[i\gamma_{jp}] &= 1 - \frac{i\Delta_t V_p}{2^f}\prod_a \sum_{\sigma_{ajp}=\pm} e^{i\sigma_{ajp}\sqrt{4\pi/f}\theta_{aj}(pd/2)} \\ &- \frac{1}{2}\left(\frac{\Delta_t V_p}{2^f}\right)^2 \prod_a \left(2 + \sum_{\sigma_{ajp}=\pm 2} e^{i\sigma_{ajp}\sqrt{4\pi/f}\theta_{aj}(pd/2)}\right) + \dots \\ &= \sum_{\sigma_{ajp}=0,\pm 1,\pm 2} G_p^{(f)}(\sigma_{ajp}) \exp\left[i\sum_a \sigma_{ajp}\sqrt{\frac{4\pi}{f}}\theta_{aj}(pd/2)\right], \qquad \text{(E.1)}\end{aligned}$$

since $(\sum_{s=\pm} e^{isx})^2 = e^{i2x} + e^{-i2x} + 2 = 2 + \sum_{s=\pm 2} e^{isx}$. In the last step we have introduced Greens functions $G_p^{(f)}$ which can be directly read off.

For $f = 1$ we have

$$\begin{aligned}\exp[i\gamma_{jp}] &= 1 - \left(\frac{\Delta_t V_p}{2}\right)^2 - \frac{i\Delta_t V_p}{2} \sum_{\sigma_{jp}=\pm} e^{i\sigma_{jp}\sqrt{4\pi}\theta_j(pd/2)} \\ &- \frac{1}{2}\left(\frac{\Delta_t V_p}{2}\right)^2 \sum_{\sigma_{jp}=\pm 2} e^{i\sigma_{jp}\sqrt{4\pi}\theta_j(pd/2)} ,\end{aligned}$$

while for $f = 2$,

$$\begin{aligned}\exp[i\gamma_{jp}] &= 1 - \frac{i\Delta_t V_p}{4} \sum_{\sigma_{1jp},\sigma_{2jp}=\pm} e^{i\sqrt{2\pi}[\sigma_{1jp}\theta_{1j}(pd/2)+\sigma_{2jp}\theta_{2j}(pd/2)]} \\ &- \frac{1}{2}\left(\frac{\Delta_t V_p}{4}\right)^2 \left(2 + \sum_{\sigma_{1jp}=\pm 2} e^{i\sigma_{1jp}\sqrt{2\pi}\theta_{1j}(pd/2)}\right)\left(2 + \sum_{\sigma_{2jp}=\pm 2} e^{i\sigma_{2jp}\sqrt{2\pi}\theta_{2j}(pd/2)}\right).\end{aligned}$$

In order to obtain Eq. (6.22) we simply have to consider $e^{i\gamma_{jp}} e^{-i\gamma'_{jp}}$ and use (E.1),

$$\begin{aligned}e^{iS_{\rm imp}} &= \prod_{j,p} e^{i\gamma_{jp}} e^{-i\gamma'_{jp}} \\ &= \sum_{\{\sigma,\sigma'\}=0,\pm 1,\pm 2} \left(\prod_{j,p} G_p^{(f)}(\sigma_{ajp}) G_p^{*(f)}(\sigma'_{ajp})\right) \\ &\times \exp\left[-i\sqrt{\frac{4\pi}{f}} \sum_{a,j,p} \left\{\sigma_{ajp}\theta_{aj}(pd/2) - \sigma'_{ajp}\theta'_{aj}(pd/2)\right\}\right] ,\end{aligned}$$

which reads in Q, N-representation, see Eq. (6.4),

$$\begin{aligned}e^{iS_{\rm imp}} &= \sum_{\{\sigma,\sigma'\}=0,\pm 1,\pm 2} \left(\prod_{j,p} G_p^{(f)}(\sigma_{ajp}) G_p^{*(f)}(\sigma'_{ajp})\right) \\ &\times \exp\left[-i\frac{2\pi}{f} \sum_{a,j,p} \left\{\sigma_{ajp}\left(Q_{aj} + \frac{p}{2}N_{aj}\right) - \sigma'_{ajp}\left(Q'_{aj} + \frac{p}{2}N'_{aj}\right)\right\}\right].\end{aligned}$$

Gaussian average

The average in Eq. (6.27) is over the Gaussian Q_a, N_a degrees of freedom and, since it is an equilibrium average, is most conveniently done in Euclidean time using S_E in Eq. (6.21), supplemented by analytic continuation to real time.

In continuous notation, this average is in real time (z runs along the Keldysh contour)

$$\mathcal{F} = \left\langle \exp\left[-\frac{2\pi i}{f\Delta_t} \sum_{a,p} \int_{\mathcal{C}} dz \sigma_{ap}(z) \left\{Q_a(z) + \frac{p}{2}N_a(z)\right\}\right]\right\rangle ,$$

and analytic continuation gives

$$\mathcal{F}_E = \left\langle \exp\left[-\frac{2\pi}{f\Delta_t} \sum_{a,p} \int d\tau \sigma_{ap}(\tau) \left\{Q_a(\tau) + \frac{p}{2}N_a(\tau)\right\}\right]\right\rangle_{S_E} .$$

The Gaussian integral is done easily, and the stationary fields $\{\tilde{Q},\tilde{N}\}$ are given by

$$\begin{aligned}\tilde{Q}_a(\omega_n) &= \frac{g_a}{2|\omega_n|\Delta_t}\left(1+e^{-|\omega_n|/\omega_a}\right)\sum_p \tilde{\sigma}_{ap}(\omega_n)\ ,\\ \tilde{N}_a(\omega_n) &= \frac{g_a}{|\omega_n|\Delta_t}\left(1-e^{-|\omega_n|/\omega_a}\right)\sum_p p\tilde{\sigma}_{ap}(\omega_n)\ .\end{aligned}$$

Hence, up to an irrelevant normalization,

$$\mathcal{F}_E = \exp\left[\sum_{a,\omega_n}\frac{\pi g_a}{2\beta f\Delta_t^2}\left\{\frac{1+e^{-|\omega_n|/\omega_a}}{|\omega_n|}|\sum_p\tilde{\sigma}_{ap}(\omega_n)|^2+\frac{1-e^{-|\omega_n|/\omega_a}}{|\omega_n|}|\sum_p p\tilde{\sigma}_{ap}(\omega_n)|^2\right\}\right],$$

with $\tilde{\sigma}(\omega_n)=\sum_{j=1}^P e^{-i\omega_n\tau_j}\sigma(\tau_j)$. Writing $\mathcal{F}_E=\exp[\Phi_E]$ and returning to the time representation, we have

$$\Phi_E = \frac{1}{\Delta_t^2}\sum_a\int_0^\beta d\tau\int_0^\tau d\tau'\sum_{p,p'}\sigma_{ap}(\tau)\sigma_{ap'}(\tau')\left\{k_a^+(\tau-\tau')+pp'k_a^-(\tau-\tau')\right\},$$

with kernels (see Ref. [86] page 58)

$$k_a^\pm(\tau)=\frac{\pi g_a}{f\beta}\sum_{\omega_n}\frac{1\pm e^{-|\omega_n|/\omega_a}}{|\omega_n|}e^{i\omega_n\tau}\ .$$

Using the free boson thermal Greens function,

$$D_\omega(\tau)=\frac{1}{\beta}\sum_{\omega_n}\frac{2\omega}{\omega_n^2+\omega^2}e^{i\omega_n\tau}=\frac{\cosh[\omega(\beta/2-\tau)]}{\sinh[\omega\beta/2]}\ ,$$

and noticing that

$$\pi\frac{1\pm e^{-|\omega_n|/\omega_a}}{|\omega_n|}=\int_{-\infty}^{\infty}d\omega\frac{1\pm e^{-i\omega/\omega_a}}{\omega_n^2+\omega^2}=2\int_0^\infty d\omega\frac{1\pm\cos[\omega/\omega_a]}{\omega_n^2+\omega^2}\ ,$$

one can write

$$k_a^\pm(\tau)=\frac{1}{\pi}\int_0^\infty d\omega\frac{J_{\pm,a}(\omega)}{\omega^2}D_\omega(\tau)\ ,$$

with spectral densities

$$J_{\pm,a}(\omega)=\frac{\pi g_a\omega}{f}\left(1\pm\cos[\omega/\omega_a]\right)e^{-\omega/\omega_c}\ .$$

Analytic continuation is now completely analogous to the standard quantum dissipation case, the only exception is in the absence of "counterterms" related to the "potential renormalization" parameters. Following Ref. [86] (page 103), this leads to $\mathcal{F}=\exp[-\Phi]$ with

$$\Phi=\frac{1}{\Delta_t^2}\sum_a\int_{\mathcal{C}}dz\int_{z'<z}dz'\sum_{p,p'}\sigma_{ap}(z)\sigma_{ap'}(z')\left\{L_a^+(z-z')+pp'L_a^-(z-z')\right\}.$$

The real-time kernels are ($\lambda = \pm$)

$$L_a^\lambda(t) = \frac{1}{\pi}\int_0^\infty d\omega \frac{J_{\lambda,a}(\omega)}{\omega^2}\frac{\cosh[\omega(\beta/2 - it)] - \delta_{\lambda,+}\cosh[\omega\beta/2]}{\sinh[\omega\beta/2]} \; . \tag{E.2}$$

The subtraction of the $t = 0$ part for $\lambda = +$ reflects the IR divergence leading to electroneutrality (6.24). Note that the sign change in the exponent upon analytical continuation is completely in accordance with Ref. [86]. The influence functional Φ written in terms of η, ξ is then

$$\begin{aligned}\Phi &= \frac{1}{\Delta_t^2}\sum_a \int_0^{t_{\max}} dt \int_0^t dt' \sum_{p,p'} \Big\{ \xi_{ap}(t)\xi_{ap'}(t')\mathrm{Re}\left[L_a^+(t-t') + pp' L_a^-(t-t')\right] \\ &+ 2i\xi_{ap}(t)\eta_{ap'}(t')\mathrm{Im}\left[L_a^+(t-t') + pp' L_a^-(t-t')\right]\Big\} \; .\end{aligned}$$

The final step is then to go back to the discretized picture. This leads to

$$\Phi = \sum_{a,p,p'}\sum_{j=1}^{P}\sum_{k=1}^{j}\left\{\xi_{ajp}\left(S_{ajk}^+ + pp' S_{ajk}^-\right)\xi_{akp'} + 2i\xi_{ajp}\left(R_{ajk}^+ + pp' R_{ajk}^-\right)\eta_{akp'}\right\},$$

with matrices for $k < j$ given by

$$\begin{aligned} S_{ajk}^\lambda &= \mathrm{Re}\left[L_a^\lambda([j-k]\Delta_t)\right], \\ R_{ajk}^\lambda &= \mathrm{Im}\left[L_a^\lambda([j-k]\Delta_t)\right]. \end{aligned}$$

For the diagonal element, one needs to be more careful (see next section).

Diagonal matrix elements

From the derivation given in the appendix of Ref. [98], the complex-valued matrix element L_{ajj}^λ is given as

$$L_{ajj}^\lambda = \frac{1}{\Delta_t^2}\int_0^{\Delta_t} dt \int_0^t dt' L_a^\lambda(t') = S_{ajj}^\lambda + iR_{ajj}^\lambda \; . \tag{E.3}$$

We first consider

$$\frac{\cosh[x+iy] - \delta_{\lambda,+}\cosh x}{\sinh x} = \frac{e^x}{2\sinh x}e^{iy} + \frac{e^{-x}}{2\sinh x}e^{-iy} - \delta_{\lambda,+}\coth x \; ,$$

and therefore,

$$\mathrm{Im}\left[\frac{\cosh[x+iy] - \delta_{\lambda,+}\cosh x}{\sinh x}\right] = \sin y \underbrace{\left(\frac{e^x}{2\sinh x} - \frac{e^{-x}}{2\sinh x}\right)}_{=1} = \sin y \; , \tag{E.4}$$

and similar

$$\begin{aligned}\mathrm{Re}\left[\frac{\cosh[x+iy] - \delta_{\lambda,+}\cosh x}{\sinh x}\right] &= \cos y\left(\frac{e^x}{2\sinh x} + \frac{e^{-x}}{2\sinh x}\right) - \delta_{\lambda,+}\coth x \\ &= (\cos y - \delta_{\lambda,+})\coth x \; . \end{aligned} \tag{E.5}$$

Inserting (E.2) in (E.3) together with (E.4) gives

$$\begin{aligned} R^{\lambda}_{ajj} &= \frac{-1}{\pi\Delta_t^2}\int_0^{\infty} d\omega \frac{J_{\lambda,a}(\omega)}{\omega^2}\int_0^{\Delta_t} dt \int_0^{t} dt' \sin\omega t' \\ &= -\frac{1}{\pi}\int_0^{\infty} d\omega \frac{J_{\lambda,a}(\omega)}{\omega^2}\frac{1-\sin[\omega\Delta_t]/\omega\Delta_t}{\omega\Delta_t}\ , \end{aligned}$$

while doing the same steps with (E.5) we have

$$\begin{aligned} S^{\lambda}_{ajj} &= \frac{1}{\pi\Delta_t^2}\int_0^{\infty} d\omega \frac{J_{\lambda,a}(\omega)}{\omega^2}\int_0^{\Delta_t} dt \int_0^{t} dt' (\cos\omega t' - \delta_{\lambda,+})\coth[\omega\beta/2] \\ &= \frac{1}{\pi}\int_0^{\infty} d\omega \frac{J_{\lambda,a}(\omega)}{\omega^2}\coth[\omega\hbar\beta/2]\left\{\frac{1-\cos[\omega\Delta_t]}{(\omega\Delta_t)^2} - \frac{1}{2}\delta_{\lambda,+}\right\}\ . \end{aligned}$$

Appendix F

Refermionization for $g = 1$

Here, we give the details of the computation leading to Eq. (6.42). The jump conditions, which are obtained in the standard way by considering the integral of the equations of motion over a small interval around the impurity, read

$$\psi_r^\dagger(pd/2+\epsilon)-\psi_r^\dagger(pd/2-\epsilon) = \frac{i\lambda r}{2}\left\{\psi_{-r}^\dagger(pd/2+\epsilon)+\psi_{-r}^\dagger(pd/2-\epsilon)\right\}e^{-ir(p\pi N^{(0)}+eV_bt)} . \tag{F.1}$$

Using the ansatz (6.36) with (F.1) and Fourier-transforming the resulting equation with respect to t gives for $p=-1$

$$b_{rk}^\dagger - a_{rk}^\dagger = \frac{i\lambda r}{2}e^{ir(kd+\pi N^{(0)})-ieV_bd/2v_F}\left(b_{-r,k-reV_b/v_F}^\dagger + a_{-r,k-reV_b/v_F}^\dagger\right) , \tag{F.2}$$

and for $p=+1$

$$c_{rk}^\dagger - b_{rk}^\dagger = \frac{i\lambda r}{2}e^{-ir(kd+\pi N^{(0)})+ieV_bd/2v_F}\left(c_{-r,k-reV_b/v_F}^\dagger + b_{-r,k-reV_b/v_F}^\dagger\right) . \tag{F.3}$$

From (F.2) one finds

$$b_{+,k}^\dagger = \frac{i\lambda}{4}e^{i(kd+\pi N^{(0)}-eV_bd/2v_F)}\left\{\left(1+\frac{4}{\lambda^2}\right)b_{-,k-eV_b/v_F}^\dagger + \left(1-\frac{4}{\lambda^2}\right)a_{-,k-eV_b/v_F}^\dagger\right\} ,$$

and

$$b_{-,k-eV_b/v_F}^\dagger = -\frac{i\lambda}{4}e^{-i(kd+\pi N^{(0)}-eV_bd/2v_F)}\left(b_{+,k}^\dagger + a_{+,k}^\dagger\right) + a_{-,k-eV_b/v_F}^\dagger .$$

Combining these two equations, one can express the b's in terms of a's,

$$\begin{aligned} b_{+,k}^\dagger &= \frac{4+\lambda^2}{4-\lambda^2}a_{+,k}^\dagger + i\frac{4\lambda}{4-\lambda^2}e^{i(kd+\pi N^{(0)}-eV_bd/2v_F)}a_{-,k-eV_b/v_F}^\dagger , \\ b_{-,k-eV_b/v_F}^\dagger &= \frac{4+\lambda^2}{4-\lambda^2}a_{-,k-eV_b/v_F}^\dagger - i\frac{4\lambda}{4-\lambda^2}e^{-i(kd+\pi N^{(0)}-eV_bd/2v_F)}a_{+,k}^\dagger , \end{aligned}$$

which is equivalent to Eq. (6.37) with the transfer matrix (6.38). The transfer matrix $\mathcal{T}_{b\to c}$ is found in exactly the same way. Multiplying the two matrices then results in

$$\mathcal{T}_{a\to c} = \frac{1}{(4-\lambda^2)^2}\begin{pmatrix} A & B \\ B^* & A^* \end{pmatrix},$$

with

$$|A|^2 = (4-\lambda^2)^4 + |B|^2 \,, \tag{F.4}$$

$$|B|^2 = (8\lambda)^2(4+\lambda^2)^2 \cos^2\left[kd + \pi N^{(0)} - \frac{eV_b d}{v_F}\right] \,, \tag{F.5}$$

and hence, one easily finds

$$c^\dagger_{+,k} = \frac{1}{(4-\lambda^2)^2}\frac{|A|^2-|B|^2}{A^*}a^\dagger_{+,k} + \frac{B}{A^*}c^\dagger_{-,k-eV_b/v_F} \,.$$

Using (6.40) one has

$$\langle c^\dagger_{+,k}c_{+,k}\rangle = \frac{1}{(4-\lambda^2)^4}\frac{(|A|^2-|B|^2)^2}{|A|^2}f(v_Fk) + \frac{|B|^2}{|A|^2}f(v_Fk-eV_b) \,,$$

and can then compute the current (6.39),

$$I = \frac{e^2}{h}V_b - ev_F\int\frac{dk}{2\pi}\left\{\frac{1}{(4-\lambda^2)^4}\frac{(|A|^2-|B|^2)^2}{|A|^2}f(v_Fk) + \frac{|B|^2}{|A|^2}f(v_Fk-eV_b) - f(v_Fk)\right\} \,.$$

Finally, the linear conductance is found by deriving with respect to the bias voltage,

$$G = \left.\frac{dI}{dV_b}\right|_{V_b=0} \,.$$

From (F.4) and (F.5) one directly sees that

$$\frac{1}{(4-\lambda^2)^4}\frac{(|A|^2-|B|^2)^2}{|A|^2} = \frac{w^2}{\cos^2\left[kd+\pi N^{(0)}-\frac{eV_bd}{v_F}\right]+w^2} \,,$$

and

$$\frac{|B|^2}{|A|^2} = \frac{\cos^2\left[kd+\pi N^{(0)}-\frac{eV_bd}{v_F}\right]}{\cos^2\left[kd+\pi N^{(0)}-\frac{eV_bd}{v_F}\right]+w^2} \,,$$

with w defined in (6.41), and thus, it is obvious that only the term proportional to $\partial_{V_b}f(v_Fk-eV_b)$ contributes to the conductance. After a change of variables one readily arrives at the final result (6.42).

Bibliography

[1] S. Iijima, Nature **354**, 56 (1991).

[2] C. Dekker, Physics Today **52** (6), 22 (1999).

[3] S. Iijima and T. Ichibashi, Nature **363**, 603 (1993); D.S. Bethune *et al.*, *ibid.*, 605 (1993).

[4] S.J. Tans *et al.*, Nature **386**, 474 (1997).

[5] A. Thess *et al.*, Science **273**, 483 (1996).

[6] T.W. Ebbesen and P.M. Ajayan, Nature **358**, 220 (1992); T.W. Ebbesen *et al.*, Chem. Phys. Lett. **209**, 83 (1993).

[7] *Carbon Nanotubes: Synthesis, Structure, Properties, and Applications*, edited by M.S. Dresselhaus *et al.*, Topics in Applied Physics, Vol. 80, (Springer,2001).

[8] M.S. Dresselhaus *et al.*, Carbon **33**, 883 (1995).

[9] P.R. Wallace, Phys. Rev. **71**, 622 (1947).

[10] M.S. Dresselhaus *et al.*, *Science of Fullerenes and Carbon Nanotubes* (Academic Press, 1996).

[11] M. Ouyang *et al.*, Science **292**, 702 (2001).

[12] T.W. Odom *et al.*, Nature **391**, 62 (1998).

[13] J.W.G. Wildöer *et al.*, Nature **391**, 59 (1998).

[14] R.E. Peierls, Ann. Phys. (Leipzig) **4**, 121 (1930).

[15] C.L. Kane and E.J. Mele, Phys. Rev. Lett. **78**, 1932 (1997).

[16] A. Bachtold *et al.*, Nature **397**, 673 (1999).

[17] Y. Aharonov and D. Bohm, Phys. Rev. **115**, 485 (1959).

[18] B.L. Al'tshuler *et al.*, JETP Lett. **33**, 94 (1981).

[19] Yu. Sharvin, Physica (Amsterdam) **126 B**, 288 (1984).

[20] A.A. Maarouf *et al.*, Phys. Rev. B **61**, 11156 (2000).

[21] R. Egger, Phys. Rev. Lett. **83**, 5547 (1999).

[22] A. Bachtold *et al.*, Phys. Rev. Lett. **84**, 6082 (2000).

[23] M. Krüger *et al.*, Appl. Phys. Lett. **78**, 1291 (2001).

[24] S. Frank *et al.*, Science **280**, 1744 (1998).

[25] G. Binnig *et al.*, Appl. Phys. Lett. **40**, 178 (1982); Phys. Rev. Lett **49**, 57 (1982); Phys. Rev. Lett. **50**, 120 (1983).

[26] J. Tersoff and D.R. Hamann, Phys. Rev. Lett. **50**, 1998 (1983); Phys. Rev. B **31**, 805 (1985).

[27] L.C. Venema *et al.*, Phys. Rev. B **62**, 5238 (2000).

[28] P. Kim *et al.*, Phys. Rev. Lett. **82**, 1225 (1999).

[29] L.C. Venema *et al.*, Science **283**, 52 (1999).

[30] *Scanning Tunneling Microscopy*, edited by J.A. Stroscio, J.W. Kaiser (Academic Press, New York, 1993).

[31] A.G. Rinzler *et al.*, Science **269**, 1550 (1995); W.A. de Heer *et al.*, Science **270**, 1179 (1995).

[32] N.S. Lee *et al.*, Diamond Relat. Materials **10**, 265 (2001).

[33] H. Sugie *et al.*, Appl. Phys. Lett. **78**, 2578 (2001).

[34] R.H. Baughman *et al.*, Science **297**, 787 (2002).

[35] S.J. Tans *et al.*, Nature **393**, 49 (1998).

[36] P.W. Anderson, Phys. Rev. **109**, 1492 (1958).

[37] C.L. Kane and M.P.A. Fisher, Phys. Rev. B **46**, 15233 (1992).

[38] P.A. Lee and T.V. Ramakrishnan, Rev. Mod. Phys. **57**, 287 (1985).

[39] S. Chakravarty and A. Schmid, Phys. Rep. **140**, 193 (1986).

[40] D.P. DiVincenzo and E.J. Mele, Phys. Rev. B **29**, 1685 (1984).

[41] J. Gonzáles *et al.*, Phys. Rev. Lett. **69**, 172 (1992); Phys. Rev. B **63**, 134421 (2001).

[42] A.W.W. Ludwig *et al.*, Phys. Rev. B **50**, 7526 (1994).

[43] A.A. Nersesyan *et al.*, Phys. Rev. Lett. **72**, 2628 (1994); Nucl. Phys. B **438**, 561 (1995).

[44] A.A. Abrikosov, L.P. Gorkov, and I. Dzyaloshinskii, *Quantum Field Theoretical Methods in Statistical Physics* (Pergamon, New York, 1965).

[45] S. Hügle and R. Egger, Phys. Rev. B **66**, 193311 (2002).

[46] L. van Hove, Phys. Rev. **89**, 1189 (1953).

[47] M. Morse, Am. Math. Monthly **49**, 358 (1942); Trans. Am. Math. Soc. **27**, 345 (1925).

[48] C. Schönenberger *et al.*, Appl. Phys. A **69**, 283 (1999).

[49] C. Chamon *et al.*, Phys. Rev. Lett. **77**, 4194 (1996); Nucl. Phys. B **466**, 383 (1996).

[50] A. Altland *et al.*, preprint cond-mat/0006362.

[51] J.W. Mintmire and C.T. White, Phys. Rev. Lett. **81**, 2506 (1998).

[52] P.A. Lee, Phys. Rev. Lett. **71**, 1887 (1993).

[53] R.A. Jishi *et al.*, J. Phys. Soc. Jpn. **63**, 2252 (1994).

[54] A. Bachtold *et al.*, Phys. Rev. Lett. **87**, 166801 (2001).

[55] R. Egger and A.O. Gogolin, Phys. Rev. Lett. **87**, 66401 (2001).

[56] D.J. Carrol *et al.*, Phys. Rev. Lett. **78**, 2811 (1997).

[57] L.D. Landau, Sov. Phys. JETP **3**, 920 (1957).

[58] S. Tomonaga, Progr. Theor. Phys. **5**, 544 (1950).

[59] J.M. Luttinger, J. Math. Phys. **4**, 1154 (1963).

[60] D.C. Mattis and E.H. Lieb, J. Math. Phys. **6**, 304 (1965).

[61] F.D. Haldane, J. Phys. C **14**, 2585 (1981).

[62] Z. Yao *et al.*, Nature **402**, 273 (1999).

[63] M. Bockrath *et al.*, Nature **397**, 598 (1999).

[64] A.O. Gogolin, A.A. Nersesyan, and A.M. Tsvelik, *Bosonization and Strongly Correlated Systems* (Cambridge University Press, Cambridge, England, 1998).

[65] W. Liang *et al.*, Nature **411**, 665 (2001).

[66] R. Egger and A. Gogolin, Eur. Phys. J. B **3**, 281 (1998).

[67] R. Egger and A.O. Gogolin, Phys. Rev. Lett. **79**, 5082 (1997); C.L. Kane *et al.*, *ibid.*, 5086 (1997).

[68] J. Voit, Rep. Prog. Phys. **57**, 977 (1995).

[69] *Single Charge Tunneling*, edited by H. Grabert and M.H. Devoret, NATO ASI Ser. B, Vol. 294 (Plenum, New York, 1992).

[70] J. Nygard *et al.*, Nature **408**, 342 (2000).

[71] H.W.Ch. Postma *et al.*, Science **293**, 76 (2001).

[72] J. Kondo, Prog. Theor. Phys. **32**, 37 (1964)

[73] L. Kouwenhoven and L.I. Glazman, Phys. World **14**, 33 (2001).

[74] A. Furusaki and N. Nagaosa, Phys. Rev. B **47**, 3827 (1993).

[75] M. Sassetti *et al.*, Phys. Rev. B **52**, 11213 (1995).

[76] A. Furusaki, Phys. Rev. B **57**, 7141 (1998).

[77] T. Kleimann *et al.*, Phys. Rev. B **66**, 165311 (2002).

[78] T. Kleimann *et al.*, Phys. Rev. B **62**, 8144 (2000).

[79] A. Braggio *et al.*, Phys. Rev. Lett. **87**, 146802 (2001).

[80] Y. Yang and T. Lin, Phys. Rev. B **64**, 233314 (2001).

[81] M. Thorwart *et al.*, Phys. Rev. Lett. **89**, 196402 (2002); M. Thorwart and M. Grifoni, Chem. Phys. **281**, 477, (2002).

[82] Yu. Nazarov and L. Glazman, cond-mat/0209090.

[83] D.G. Polyakov and I.V. Gornyi, cond-mat/0212355.

[84] P. Fendley *et al.*, Phys. Rev. B **52**, 8934 (1995).

[85] C.W.J. Beenakker, Phys. Rev. B **44**, 1646 (1991).

[86] U. Weiss, *Quantum Dissipative Systems*, Vol.2 (World Scientific, Singapore, 1999).

[87] K.A. Matveev *et al.*, Phys. Rev. Lett. **71**, 3351 (1993).

[88] O.M. Auslaender *et al.*, Science **293**, 76 (2001).

[89] H.W.Ch. Postma *et al.*, Phys. Rev. B **62**, R10653 (2000).

[90] J. Kong *et al.*, Phys. Rev. Lett. **87**, 106801 (2001).

[91] M. Bockrath *et al.*, Science **291**, 283 (2001).

[92] J.W. Park *et al.*, Appl. Phys. Lett. **81**, 2644 (2002).

[93] K. Moon *et al.*, Phys. Rev. Lett. **71**, 4381 (1993).

[94] N. Hatano and M. Suzuki, in *Quantum Monte Carlo Methods in Condensed Matter Physics*, edited by M. Suzuki (World Scientific, Singapore, 1993).

[95] K. Leung *et al.*, Phys. Rev. Lett. **75**, 3344 (1995).

[96] C.H. Mak and R. Egger, Phys. Rev. E **49**, 1997 (1994).

[97] R. Egger and H. Grabert, Phys. Rev. B **58**, 10761 (1998).

[98] R. Egger and C.H. Mak, J. Phys. Chem. **98**, 9903 (1994).

[99] W. Krauth, *Introduction to Monte Carlo Algorithms* in *Advances in Computer Simulation*, edited by J. Kertesz and I. Kondor, Lecture Notes in Physics (Springer, 1998); K.P.N. Murthy, cond-mat/0104215.

[100] N. Metropolis, J. Chem. Phys. **21**, 1087, (1953).

[101] K. Binder, *Theory and Technical Aspect of Monte Carlo Simulation* in *Monte Carlo Methods in Statistical Physics*, edited by K. Binder, (Springer, 1979).

Danksagung

An dieser Stelle möchte ich meinen Dank an diejenigen aussprechen, die zum Gelingen dieser Arbeit beigetragen haben.

Herrn Prof. Dr. Reinhold Egger danke ich für die engagierte Betreuung und seine unermüdliche Geduld.

Meinen Eltern danke ich für die Unterstützung während des Studiums und der Promotion.

Erklärung

Hiermit erkläre ich, die vorliegende Dissertation eigenhändig und ohne unerlaubte Hilfen angefertigt und diese in der vorgelegten oder in ähnlicher Form noch keiner anderen Institution eingereicht zu haben.

Düsseldorf, den 02.04.2003

Sascha Hügle